UNIVERSITÀ
DEGLI STUDI
FIRENZE

PhD in
Atomic and Molecular Photonics

CYCLE XXXII

COORDINATOR Prof. Francesco Saverio Cataliotti

Photopolymerization approaches towards smart responsive surfaces and materials

Academic Discipline (SSD) CHIM/07

Doctoral Candidate
Dr. Flavia Lupi

Supervisor
Prof. Diederik Sybolt Wiersma
Co-Supervisor
Dr. Camilla Parmeggiani

Coordinator
Prof. Francesco Saverio Cataliotti

Years 2016/2019

alla mia famiglia

Summary

Preface

Surface represents the interface between a system and the environment that surround it. In nature, there are a lot of examples in which a particular structuration/chemical composition of a surface is essential for the interactions with the environment. Surfaces of living organisms are often organized in micro- and/or nano-scopic structured motif, and generally, result in amazing functions optimized by natural evolution. Technological applications extensively took inspiration by nature in order to reproduce or even improve well-known and consolidated functionalities. Among them, special attention was deserved to surface with controllable wettability and biocompatible surfaces for biological applications.

Bioinspired functional surfaces with specific wettability have been extensively investigated, because their underling mechanism opens to many applications as self-cleaning and waterproof coatings that have a great potential in the fields of materials science, medicine, engineering and so on. Moreover, material biocompatibility is a fundamental requirement for every device that operates in biological or biomedical environment.

The aim of this thesis was to realize modified surfaces for specific aims, using different materials and techniques. Our approach includes a morphological modification of the surfaces (physical methods) as well as a diffuse employ of chemistry needed to create the appropriate materials, focusing on micro-structured surfaces for two scopes. First, in self-cleaning applications, , the main goal was the realization of a surface whose wettability could be dynamically controlled by a remote stimulus controlling both the morphology of the surface and the chemical composition of the material. In this context, we were interested to use light as a trigger to change the surface properties, because it allows rapid, local, and wireless control on a specific area and it is a clean, cheap and environmental-friendly energy source.

The second topic was to realize micro-structured surfaces that would drive the proliferation and differentiation of cells for tissue engineering applications. In the last years, this was an hot topic for regenerative medicine, and functional substrates will improve the performances of the existing protocols for *in vitro* studies on selected cellular lines. Together with regenerative medicine for implantable devices, *in vitro* studies are useful to understand the mechanisms of specific diseases. Open challenges are the growth of functional tissues and differentiation and maturation of stem cells *in vitro* analysis. In this scenario, biomimetic substrates can provide an effective maturation of the stem cells, that highly resemble adult cells.

To realize these objectives, we exploited different surface modifications from photopolymerization reaction to create a polymer substrate and functionalization of a glassy or polymeric surface, up to physical micro-structuration realized by lithographic techniques.

The materials chosen for the fabrication of micro-structured surfaces for self-cleaning applications are Liquid Crystalline Elastomers (LCEs), a type of shape-changing polymers that have attracted scientists' attention for their ability to translate a small molecular movement, triggered by an external stimulus, into large mechanical motion. Regarding the materials that improve cellular growth, we chose hydrogel-based surfaces for their biocompatibility and biodegradability and, in particular, poly(ethylene glycol) (PEG) was found as the best candidate within polymeric hydrogels for its high biocompatibility and tuneable cross-link density.

In both cases, we realized the micro-structured surfaces using soft-lithography, a convenient, effective and low-cost strategy based on replica molding.

The content of this thesis is summarized below:

Chapter 1 reports an introduction to different surface modifications in various technological fields, with particular attention on industrial applications in which the change of the wettability property is the widespread objective. The general concepts of the wettability are described, and different surface modifications technique are summarized, distinguishing them in chemical and physical methods. Particular attention is addressed to two different fields: the micro-structuration of surfaces for self-cleaning and the tissue engineering applications. Finally, the materials employed in this thesis work are presented and explained highlighting the molecular mechanism beneath their reconfigurability.

Chapter 2 highlights the objectives and the results obtained in the fabrication of self-cleaning surfaces using acrylate-based LCEs. Photoresponsive surfaces were realized by introducing an azo dye in the polymeric network. Depending on the azo dye moieties, the absorbed energy can result in an isomerization or in a thermal relaxation. Both processes can induce a phase transition of the liquid crystalline network, translating the molecular process in a macroscopic deformation of the material. Two kinds of mixtures were considered, that mainly differ for the mechanism of their photoresponsive behaviour (isomerization and heat dissipation). The two different mechanisms are characterized by different response times and temperature gradients that revealed their pros and cons in the change of wettability of the surface. Moreover, the post-functionalization of these micro-structured surfaces with silanization reaction has been studied to enhance the superhydrophobic nature of the micropatterned interfaces.

Chapter 3 shows the synthesis of a small library of thiols and alkynes to be employed in a different synthetic strategy for the fabrication of more responsive polymers with a larger deformation capability. The click polymerization reaction between thiols and alkynes was used to produce different LCEs samples characterized by a mixed main-chain/side-chain architecture, in which the mesogens are both incorporated in the main-chain and attached to it with a spacer. Thanks to this

mixed network, polymers obtained with this strategy undergo larger deformations than acrylate-based LCEs. A characterization of thermoresponsivity of these polymers was performed and finally, thermal and mechanical properties of these materials were evaluated by Differential Scanning Calorimetry (DSC) and Dynamic Mechanical Analysis (DMA) measurements.

Chapter 4 shows hydrogel-based micro-patterned surfaces for tissue engineering applications. We evaluated how human induced pluripotent stem cells-derived cardiomyocytes (hiPSC-CMs) grow and differentiate on micro-patterned hydrogel substrates. Using soft-lithography, different patterned surfaces were obtained, and a characterization of the biological activities, using action potential (AP) and calcium transients (CaT) of these cellular lines, was performed by a collaboration with the laboratory of Dr. Raffaele Coppini and Dr. Cecilia Ferrantini of the University of Florence.

Part of this PhD thesis has been the object of publications and communications at conferences.

Papers:

1. J.M. Pioner et al, “Optical Investigation of Action Potential and Calcium Handling Maturation of hiPSC-Cardiomyocytes on Biomimetic Substrates”, *Int. J. Mol. Sci.* **2019**, *20*, 3799.

Congresses:

1. **F. Lupi**, D. Martella, S. Nocentini, C. Parmeggiani, D. S. Wiersma. Poster Communication: “Thiol-yne click chemistry as a new synthetic tool for liquid crystalline elastomers preparation”, XLII “A. Corbella” International Summer School on Organic Synthesis, Gargnano (BS), Italy, June 18 – 23 2017.
2. **F. Lupi**. Poster Communication: “From synthesis to applications: how to get smart materials”, Poster Session European Laboratory for Non-Linear Spectroscopy, Florence (FI), Italy, October 9 2017.
3. **F. Lupi**, D. Martella, C. Parmeggiani, S. Nocentini, D. S. Wiersma. Poster Communicaion: “A chemical insight in liquid crystalline elastomers”, 27th International Liquid Crystal Conference, Kyoto, Japan, July 20-27 2018.
4. **F. Lupi**, D. Martella, C. Pamreggiani, D.S. Wiersma. Oral Communication: “Exploring thiol and alkyne chemistry for smart polymers preparation”, XLIII "A. Corbella" International Summer School on Organic Synthesis, Gargnano (BS), Italy, June 10-14 2018.
5. **F. Lupi**, D. Martella, C. Parmeggiani, D.S. Wiersma. Oral Communication: “Liquid crystalline elastomers based on thiol-yne click chemistry”, International Liquid Crystal Elastomers Conference, Eindhoven, Netherlands, September 15-18 2019.

Chapter 1 - Introduction

1.1 Surface engineering for different technological fields

Surface modification is a key aspect in many different research areas. Surface regulates the interaction of each system with the surrounding environment that can be represented by an empty space as well as by the presence of other materials. In many cases, the interface between the material surface and the environment regulates the "device" functionalities and properties.

One of the most relevant example of functional surface is represented by our skin. It is only a few millimetres thick, but it is our heaviest and largest organ, being one seventh of our body weight. It represents the human interface with the external environment: it works as a barrier that protects the body against pathogens, foreign bodies, water loss, solar radiation and has a key role in temperature regulation, sensing and vitamin D production [1]. Skin was chosen as introductive example because it behaves as an active layer, able to reconfigure itself depending on the biological stimuli that it receives.

Taking inspiration by the several roles that surfaces play in nature, in technological applications, there is the need to tailor the surface properties in a highly specific and possibly programmable way. The latter requirement aims to change the surface properties "on-demand" in order to obtain a dynamic response to selected external stimuli.

Surface properties may be inadequate in terms of wettability, adhesion properties, resistance to environmental agents. On the other side, in biological applications, properties as biocompatibility and good adhesion of proteins and cells in cell scaffolds should be considered. To reply to these requirements, surfaces can be modified to match the characteristics needed by different applications. One of the most common procedure to modify the surface properties is to introduce specific coatings made by functional materials [2]–[5]. Moreover, the morphological properties and the chemical structure/composition can be modified in order to obtain an optimal and desired surface.

In the industrial field, a wide range of surface modifications have been employed and in **Figure 1**, some representative examples are shown. In solar cells, the interplay of the chemical composition and the morphology (characterized by an hierarchical roughness) of their antireflective self-cleaning coatings aims to reduce dust accumulation, that is one of the principal causes of reduced efficiency [6]. Self-cleaning surfaces are of great interest for the efficiency of solar energy production (solar cells and panels) as well as in the automotive field. Indeed, car glasses are treated with fluoroalkylsilanes to provide self-cleaning properties. In such a way, during car acceleration the water droplets are able to remove dust and powder as they are blown over the glass substrate. These represent just two examples of hydrophobic surfaces in our daily life but besides hydrophobicity, wettability of a surface from oils (oleophobicity) represents another

widespread issue. A very popular example is represented by the non-stick pan, on which a micro-layer of polytetrafluoroethylene (PTFE), as the well-known brand of which is “Teflon”, prevents the food sticking to the pan.

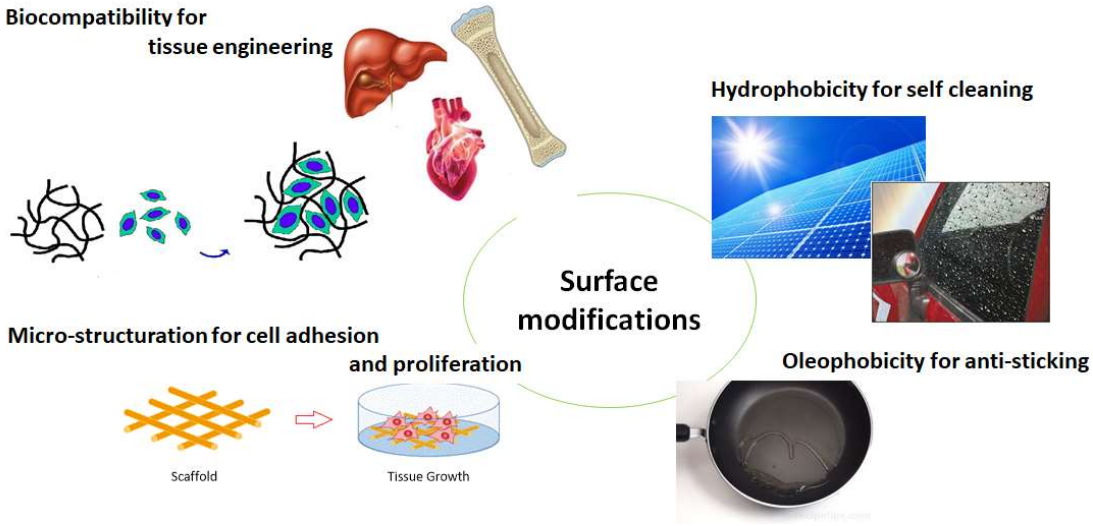

Figure 1 – Examples of surface modifications and correspondent applications. In solar panel and car glasses a special coating reduces the wettability and enhances a self-cleaning effect. A micro-layer of Teflon on the internal surface of the pun allows an anti-sticking effect. In tissue engineering, micro-structured surfaces are used to drive cellular growth and ensure in vivo tissue culture for future implantation. In this field, biocompatibility is the key property for an optimal bio-surface modification.

Looking closer at biomedical applications, surface modification is a useful tool to improve the properties of an implantable device or to study the mechanism of particular diseases. Biomaterials, fully or partially synthetic, or made by biological components, interact with the biological environment through their surface. Surface properties such as roughness, morphology, charge, chemical composition, surface energy and wettability all influence the interactions of the biomaterial with the biological compounds. Biocompatibility, defined as the property of a material to be compatible with living tissue, rules phenomena as adhesion and proliferation of cells on the materials used for surgical implant. For this reason, biocompatible materials do not produce a toxic or immunological response in the interaction with the body or biological fluids.

The progress in surface modification techniques has been pushed by extensive studies on the relations between chemical structure and surface performance. On the other side, the enlarged availability of analytical instruments for surface characterization and for surface treatment allowed to achieve specific physicochemical structures of the surface.

1.1.1 Surfaces with different wettabilities: general concepts

One of the most studied aspect in surface chemistry is wettability. Many examples of artificial hydrophobic surfaces have been described in literature, mimicking nature to develop synthetic advanced materials [7], [8]. Wettability is a superficial property that attracts the industrial attention in the realization of hydrophobic/hydrophilic surfaces, antifogging mirrors and displays, self-cleaning window and panels, anti-reflection, anti-icing materials [9]–[11].

Surfaces with different wettability have been first observed in nature in butterfly wings, fish scale and many plants (e.g. Lotus leaf and red rose petals). The capability of a water droplet to roll-off without wetting the surface is a behaviour which can be found in the Lotus leaf, which is characterized by both superhydrophobicity and low surface energy (**Figure 2a**). If high hydrophobicity is coupled to a high surface energy, as for the red rose petal, the water droplet on the surface appears spherical in shape, and it is not able to roll off even if the petal is turned upside down (**Figure 2b**).

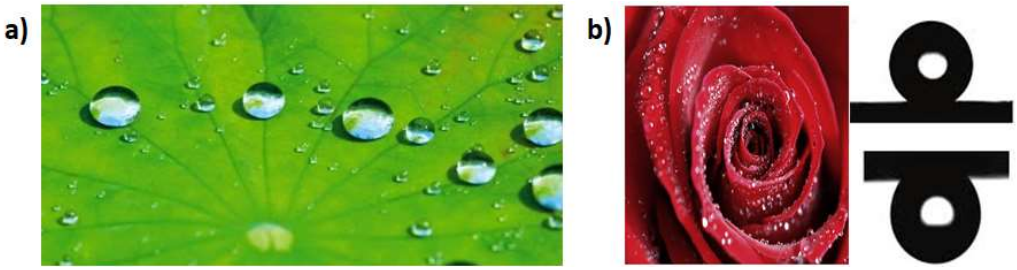

Figure 2 – Superhydrophobicity in nature. (a) In Lotus leaf, superhydrophobicity and low surface energy cooperate for a not wettable effect. (**b**) In red rose petal, superhydrophobicity and, a high adhesive force, do not allow the rolling of the water droplet even when the petal is turned upside down.

The parameters used to describe the wettability of a selected surface are the contact angle (CA) and the tilting (or sliding) angle (TA or SA). The former quantifies the degree of wetting of a solid surface: the CA of a liquid on a surface depends on the surface tension (molecular forces) of the involved liquid, the solid surface and the surrounding vapor. Thus, wetting depends on the competition of two phenomena: the bulging of the droplet on the surface to form a spherical shape and the adsorption on the surface to form a wetting layer [12], [13].

The interfacial tensions between liquid-air, liquid-solid and solid-air determine the contact angle of a liquid droplet on a given surface and are described by Young's equation, shown in **Figure 3a**. The contact angle given by Young's equation or the Young contact angle (YCA) is a static angle.

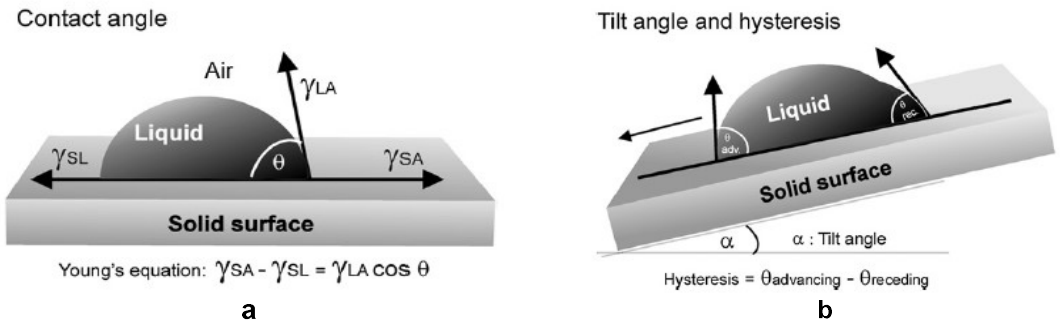

Figure 3 – Wetting of a solid surface. γ_{LA}, γ_{SL} and γ_{SA} are interfacial tensions at the boundaries between liquid (L), solid (S) and air (A), which determine the CA of a water droplet and are described by Young's equation (**a**). The hysteresis of a water droplet on a tilted surface represents the adhesion of the liquid on the surface and can be determined by measuring the tilting angle or the advanced and receding angle of a water droplet (**b**). Images adacted from [14].

If the solid-vapor interfacial energy is denoted by γ_{SA}, the solid-liquid interfacial energy by γ_{SL} and the liquid-vapor interfacial energy (i.e. the surface tension) by γ_{LA}, the equilibrium contact angle θ is determined from these quantities by the Young equation.

$$\gamma_{SA} - \gamma_{SL} = \gamma_{LA} \cos\theta$$

Solid surfaces can be classified in four categories on the basis of their CA as reported in **Figure 4**: (**a**) superhydrophobic if CA is above 150°, (**b**) hydrophobic if CA is between 90° and 150°, (**c**) hydrophilic if the CA is between 10° and 90° and (**d**) superhydrophilic if the CA is less than 10°[15].

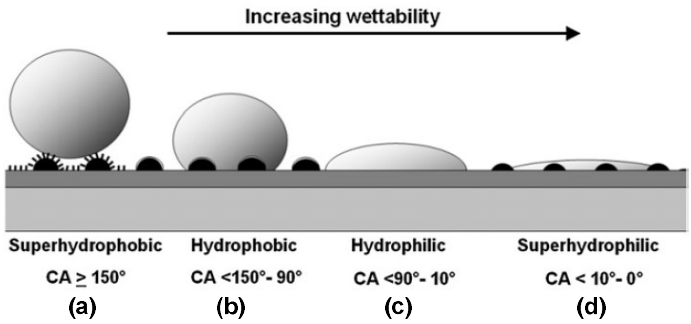

Figure 4 – Four classes of surface wettability. Images adacted from [14]**.**

When the surface is tilted of a certain angle, the droplet can start to roll off the surface, and it is necessary to introduce the tilt (or sliding) angle (TA or SA), as shown in **Figure 3b**. TA can be evaluated from the contact angle hysteresis (CAH) that is the difference between the advancing and receding contact angles. Let's think about the water droplet on a tilted surface. If there is no contact angle hysteresis, the drop would immediately, when hitting the surface, start to slide because of gravity. For hysteresis > 0°, the advancing and receding angles can be measured. The advancing contact angle is the maximum contact angle that the surface can have, and the receding contact angle is the minimum one. Superhydrophobic and self-cleaning surfaces (Lotus leaf) are

characterized by low TAs (<10°) , whereas the combination of high CA and high TA results in adhesion and “storage” of droplets (rose petals).

Control of the water droplet adhesion is very important towards applications as water harvesting, biochemical analysis and lab-on-chip devices [16]–[18]. Low-surface-energy structures with different levels of roughness exhibit different levels of adhesion: an extremely rough surface with low surface energy makes the surface superhydrophobic, while smooth or ideally flat surfaces with low surface energy can result in an adhesively hydrophobic or even hydrophilic substrate [19], [20].

1.2 Surface modification techniques

Several techniques have been employed for surface modifications and many methods have been proposed to classify them. One of the common way consists in considering the type of interaction between the treatment and the substrate. Generally, physical methods consist in a coating deposition with no chemical bonds between the coating and the substrate, while chemical methods include all the modifications in which the chemical substance is covalently attached to an activated substrate.

Following this classification, we divided the techniques for surface treatment into three categories: physical deposition of surface-active compounds, direct coupling reactions of polymers onto surfaces (grafting-to) and grafting of monomers from reactive surfaces (grafting-from) [21]–[23].

The physical deposition of surface compounds leads to noncovalently bound coatings, and this is a reversible process. Such coatings may be unstable under high shear forces or other adverse chemical and physical conditions. Surface modification via coupling reactions (grafting-to) has several limitations (e.g. incomplete surface coverage, diffusion limitations of the polymers to the surface, island formation due to steric crowding of the reactive sites by the already grafted polymers), hence the grafting-from technique is often preferred, since the grafts are formed through the reaction of monomers from active surfaces, forming robust coatings that provide great control over the density and functionality of the grafts.

In this thesis, we used different methods to modify the surfaces depending on the final application. The used techniques often requires different steps and can not be univocally defined as chemical or physical method. For example, soft-lithography, which is generally a physical method, has been employed to obtain micro-structured surfaces, by polymerization of a monomer mixture infiltrated in the mold. Within this work, in the case of hydrogel-patterned surfaces for biological applications, the polymerized mixture was covalently bonded to the substrate while in

the case of micro-structured surfaces for self-cleaning devices there was no chemical interaction between the polymeric matrix and the substrate. However, we decided to define soft-lithography as a physical method, and the photopolymerization as a chemical method.

1.2.1 Physical methods

1.2.1.1 Soft-lithography

Soft lithography [24] is a convenient, effective and low-cost strategy based on replica molding for the realization of 2D micro- and nanostructures. In soft-lithography, an elastomeric stamp (usually polydimethyl siloxane) with a patterned-relief surface is used to create patterns and structures with feature sizes ranging from nanometer [25] to micrometer [26]. This technique aims to overcome the drawbacks of photolithography [27], [28], in which the entire pattern of the photomask is projected onto a thin film of photoresist. Although photomasks are commercially available, the time and costs involved in the fabrication and photo-alignment of such masks represent a significant barrier to the use of photolithography in rapid and inexpensive prototyping. **Figure 5** outlines the five steps of the procedure generally used for soft-lithography:

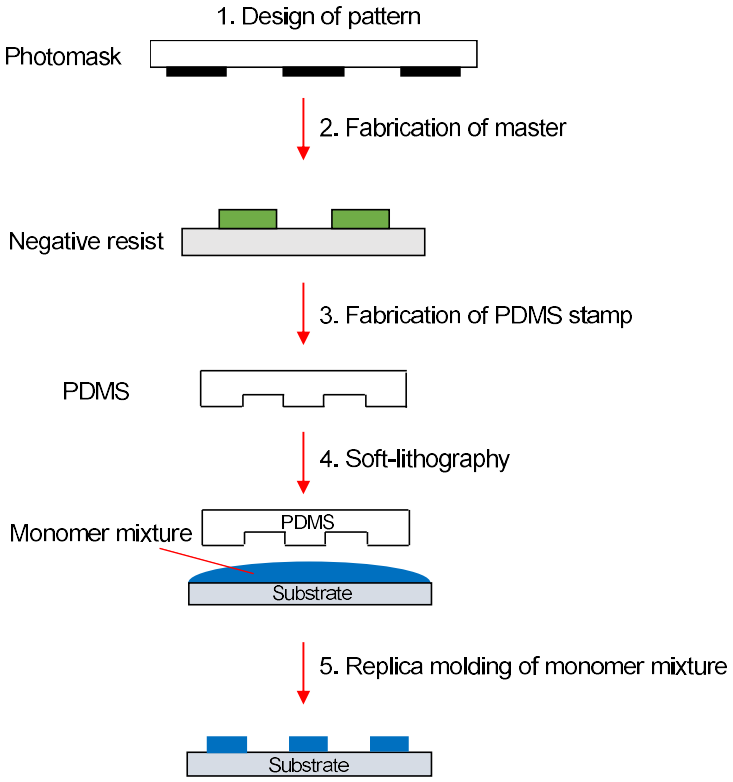

Figure 5 – Schematic procedure for soft-lithography.

1. Pattern design involves the use of computer-aided design (CAD) software. A wide range of software are commercially available and allow to design the pattern on a chrome mask (i.e. a quartz or fused silica plate patterned with opaque chrome on its surface) (**Figure 5**, step 1).

2. High-resolution printing (such as E-beam lithography, UV lithography) provides a simple and convenient method for fabricating photomasks on transparent films, the master [29]. Chrome photomasks are available from commercial suppliers in the price range from hundreds to thousands of dollars depending on the feature size and density of patterns on a photomask (**Figure 5**, step 2).

3-5. The key feature of soft lithography is the negative replica of the master with an elastomeric stamp. The replica molding (REM) [30] method, using poly(dimethyl siloxane) (PDMS) [31], allows to rapidly create several copies of the molds [32] on a large area (parallel fabrication process). Moreover a wide range of polymers can be used for the mold and the micro-patterning can be applied and be transferred to non-planar surfaces thanks to the elastic nature of the mold [33]. The liquid prepolymer of PDMS is casted on the photomask and, after curing, the cross-linked and elastomeric PDMS is carefully peeled off from the master. The nano/micro structures present on the PDMS replica are, in turn, re-replicated using a rigid or elastic organic polymer, the material for the final structure. Also the second replica has no restriction on the employed material. Widespread materials include a photochemically-curable polyethylene glycol diacrylate (PEG-DA) [34] or polyurethane (PU) [35], [36] that are well known to precisely replicate the original master in polymeric nanostructures with high accuracy (**Figure 5**, steps 3, 4 and 5).

1.2.2 Chemical methods

1.2.2.1 Photopolymerization reaction as tool for surface modification

Photopolymerization is a chemical process that rules the formation of polymeric chains from single monomers or cross-linked network by light (commonly triggered by a photo-initiator molecule). In general, the polymerization generates the increase of molecular weight and includes the crosslinking of pre-existing macromolecules. Photopolymerization played an important role in the early development of polymer chemistry. One of the first procedures for polymerizing vinyl monomers was to expose the monomer to sunlight [37]. In 1845 Blyth and Hoffmann obtained a clear glass-like product from styrene and Berthelot and Gaudecheon were the first scientists to polymerize ethylene creating a solid structure by ultraviolet light.

Photochemically production of primary radicals can be obtained at low temperatures (10-40°C), except for thermal free-radical initiators which generally operate above 40°C. This technique is the basis of the important and widely used commercial processes with broad applicability, such as photoimaging and ultraviolet curing of coatings and inks. In the process, light is absorbed by the system and used to trigger the radical formation whose instability results in the formation of new chemical bonds.

Photoinitiators are usually added to the monomeric mixture to favour the creation of reactive species. Fundamental requirement for photopolymerization is the spectral matching of the emission wavelength of the light source with the absorption band of the photoinitiator .

They absorb light in the UV-visible spectral range (250-450 nm) and transform light energy into chemical energy in the form of reactive intermediates, such as free radicals and reactive cations. Subsequently they initiate the polymerization of functional monomers to form linear polymers, whereas multifunctional monomers generate three-dimensional crosslinked networks.

Photopolymerization can be ruled by two different processes, free radical and ionic reaction. The former is most extensively used because of its applicability to a wide range of formulations based on acrylates [38], unsaturated polyesters [39], and polyurethanes [40].

For free radical polymerization (**Scheme 1**), the photoinitiator (**IN**) absorbs the incident light and it is promoted to an electronically excited state (**IN***) (**Scheme 1**, step 1), characterized by a short lifetime (generally less than 10^{-6} sec), in which it can decay back to **IN** (**Scheme 1**, step 2) with emission of light or heat, or become a reactive intermediate $\mathbf{I}^{\bullet}$ or $\mathbf{I}^{+}$ (**Scheme1**, step 3). The reactive intermediate may be in turn react with another radical **R** (**Scheme 1**, step 4) or initiate polymerization of monomer **M** (**Scheme 1**, step 5).

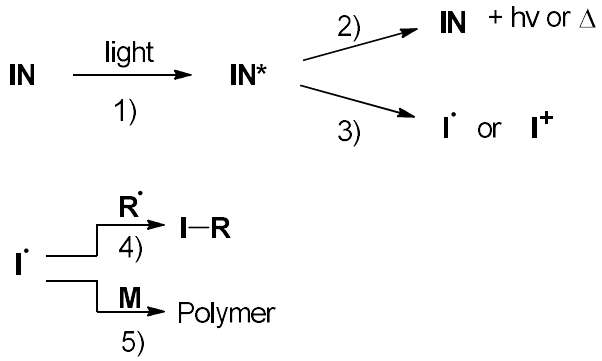

Scheme 1 – Scheme reaction of photopolymerization

In most cases, polymerization in air can be hindered. The problem of radical quenching by oxygen can been avoided by performing the photopolymerization in vacuum or in an inert atmosphere, such as molecular nitrogen [41].

In this thesis work, we used photopolymerization to create hydrogel-patterned substrate for the cellular growth studies, and for the realization of polymeric liquid crystalline elastomers based films with micro-structured surfaces.

1.2.2.2 Silanization

Silanes are silicon derivatives and refer to many compounds with four substituents on silicon. They have a hydrolytically sensitive center, that can react with inorganic substrates, such as glass, to

form stable covalent bonds, and an organic substitution that alters the physical interactions with treated substrates.

Silanization is a low-cost and effective covalent coating method to modify material surface that is rich in hydroxyl groups (**Figure 6**) [42]. In contrast with silanes commonly used as coupling agents in adhesive applications, silane groups for surface modification (for example to improve or decrease the wettability), under normal conditions, do not impart chemical reactivity to the substrate. There are many types of commercially available silane-coupling agents, that easy react with hydroxylated surfaces and introduce active groups. Even if silanization is a simple process, reaction conditions, such as concentration of the silane and reaction time, must be carefully controlled to prevent the formation of thick polymerized silane network on the surface. Otherwise, the bond between silane and the surface can also be subjected to hydrolysis in some conditions.

Within this work, this reaction was used in different areas for a wide range of purposes: to ensure the hydrogel attachment on glass surface [43], to improve the hydrophobicity increasing the contact angle (CA) and decreasing the adhesion force (AF) of a water droplet on the surface [44], to reach the liquid crystal alignment in a homotropic way [45].

The silane bond to a substrate requires a pre-silanization treatment of the substrate to expose free-hydroxyl groups on the surface (**Figure 6a**).

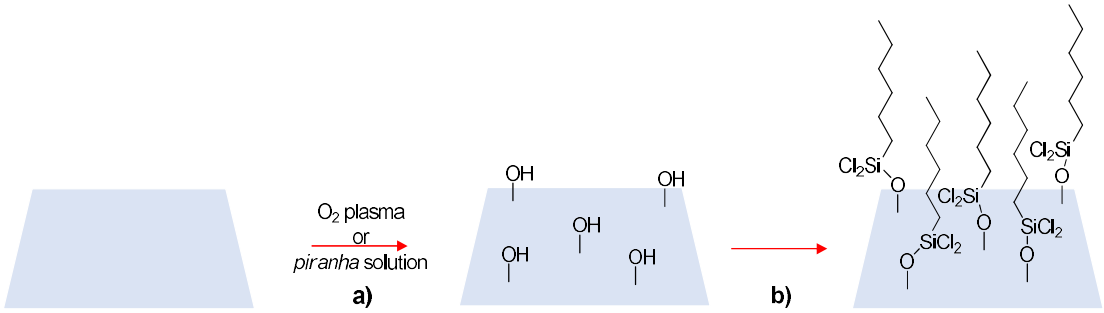

Figure 6 – Schematic illustration of functionalization of glass surface by silanization reaction.

This step can be performed in different ways depending on the substrate material. If the sample is a glass slide, the treatment can be made in wet conditions by a basic or acid *piranha* solution [46]. Otherwise, if the sample is a polymeric film or substrate, mild and dry conditions are required: oxygen plasma method can be applied to oxidize the sample surface and produce free-hydroxyl groups at the interface of the substrate [47].

In the silanization step (**Figure 6b**), the choice of the silane , as well as its concentration, the solvent and time exposition are dependent from the desired final result. Most of the widely used organosilanes have one organic substituent and three hydrolizable substituents (**Figure 7**).

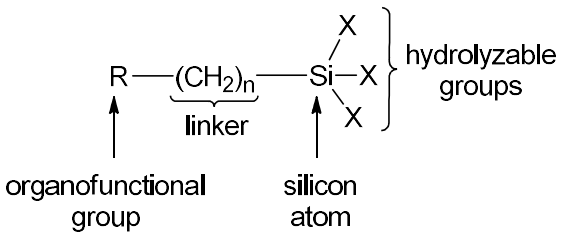

Figure 7 – General molecular structure of a silane molecule.

In several surface treatment applications, the alkoxy groups of the trialkoxysilanes are hydrolysed to form a silanol-containing species. Reaction of these silanes involves four steps (**Scheme 2**).

In the first step, hydrolysis of three labile groups occurs; then, silane molecules undergo a condensation reaction to form oligomers, which then interact by hydrogen bond with the activated OH groups of the substrate. In the final step, during drying or curing, a covalent bond is formed with the substrate with loss of water. The latter reactions can occur in the same time after the first hydrolysis step. The R group remains available for covalent reaction (when it is functionalized) or physical interaction with other phases [48].

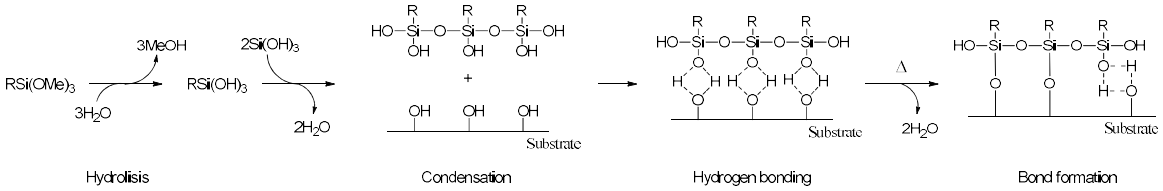

Scheme 2 – Reaction mechanism for functionalization of hydroxylate-activated substrate.

Water for the hydrolysis step may be added, it may be present on the substrate surface, or it may come from the atmosphere. The polymerization degree of the silanes is dependent on the amount of water available and the organic substituent. If the silane is added to water and has low solubility, a high degree of polymerization is favoured.

The thickness of a polysiloxane layer is determined by the concentration of the siloxane solution. Moreover, the formation of covalent bonds on the surface (last step) proceeds with a certain amount of reversibility. As water is removed, generally by heating up to 120° C for 30 or 90 minutes or under vacuum for 2 to 6 hours, bonds may form, break and reform to release internal stress.

The factors that influence the silane surface modification are the concentration of surface hydroxyl groups, the type of surface hydroxyl groups, the hydrolytic stability of the bond formed and the physical dimensions of the substrate or substrate features.

As previously mentioned, silanization has been employed in this work for various purposes: to control the liquid crystal alignment as well as for guarantee the adhesion of two substrates, and decrease the wettability changing the adhesion forces.

Silanization for LC alignment

A relevant issue in many technological applications is the alignment of liquid crystals (LCs). In all liquid crystal applications, a specific LC orientation must be defined at one or two interfaces of the LC cell. Examples include planar anchoring, where the LC long axis lies in the surface plane (**Figure 8a**) or homeotropic anchoring, where the long axis of the LC molecules is oriented perpendicularly to the surface (**Figure 8b**).

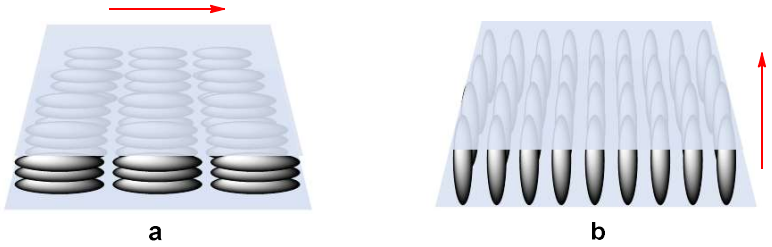

Figure 8 – Uniaxial homogeneous (a) and homeotropic (b) alignments of liquid crystal molecules.

To achieve these LC alignments, a wide range of surface modifications are available. The most common strategy exploits the use of a chemical substance, such as polyimide (PI) [49] or polyvinyl alcohol (PVA) [50], to create sacrificial layers. The homogenous planar anchoring (**Figure 8a**) is then guaranteed by a rubbing of the sacrificial layer by a velvet cloth while the homeotropic one (**Figure 8b**) requires only a proper choice of the polyimide. Sometimes, the use of sacrificial layers is not suitable, as for spontaneous LC infiltration in the micro-structured substrates [51], and a chemical functionalization is required.

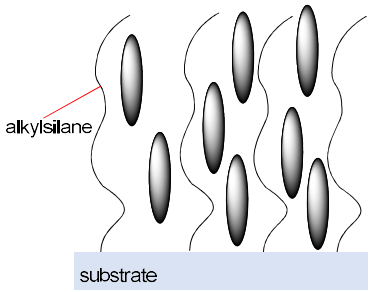

Figure 9 – Schematic alignment mechanism of LC molecules between silane alkyl chains.

In **Figure 9** the mechanism involved in homotropic LC alignment with a silanized surface is shown. The mesogens interact with the alkyl chains of the silane molecules attached to the substrate. This step is influenced by the concentration of the silane on the surface and the alkyl chain length [45].

Silanization for tissue engineering

In the field of tissue engineering, studied in this work for the growth of stem-cells, the silanization reaction of a glass substrate is a good tool to ensure the attachment of a micro-patterned-hydrogel support during the proliferation process.

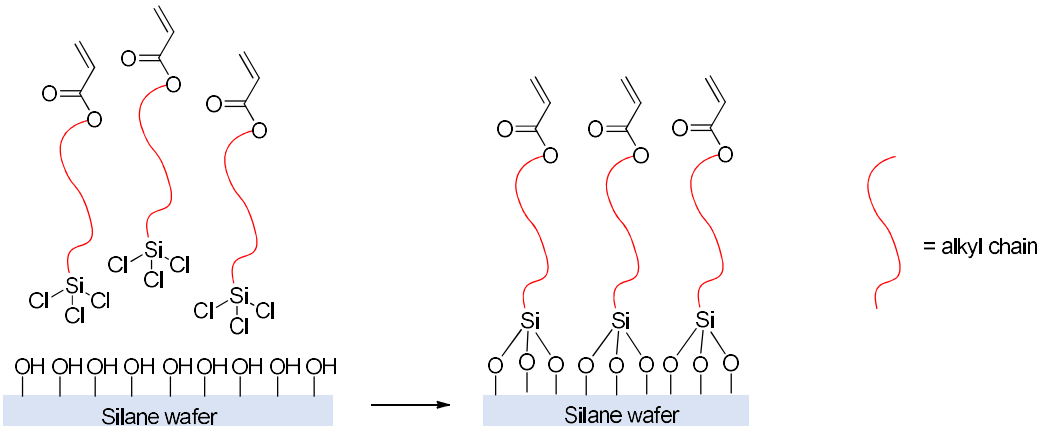

Figure 10 – Schematic reaction for functionalization of hydroxyl-activated substrates with silane molecules bearing polymerizable functionalities, in this case acrylate groups.

In this case, the silane agent is characterized by an acrylate group on one end of the molecule. For example, when the hydrogel substrate is polyethylene glycol diacrylate (PEG-DA), the silane molecule with the end- acrylate group allows the anchoring of the hydrogel layer to the substrate during the polymerization step [43]. In this context the concentration of the silane is a very important parameter to ensure the good attachment of the hydrogel layer on the glass surface (**Figure 10**).

Silanization and wettability

Functionalization of surfaces with silane molecules allows to increase and tailor the wettability properties. A successful hydrophobic coating must eliminate or mitigate hydrogen bonding and shield polar surfaces from interaction with water by creating a non-polar interphase. Aliphatic hydrocarbon substituents or fluorinated hydrocarbon substituents [52] are the hydrophobic entities which enable silanes to induce surface hydrophobicity.

1.3 Modified surfaces for material science and biological applications

1.3.1 Micro-structured surfaces for modulation of wettability and adhesion force

Superhydrophobic lotus leaves and rose petals are two relevant examples of biological surfaces with low and high liquid-solid adhesion, respectively.

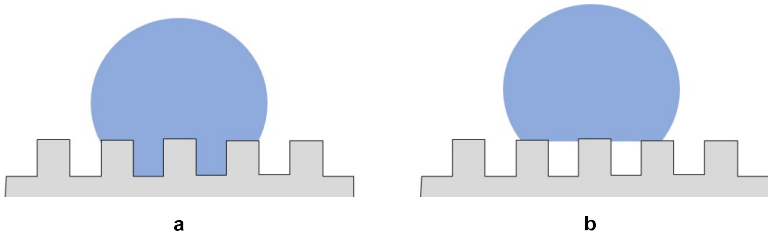

Figure 11 – A liquid droplet a) in the Wenzel state and b) in the Cassie state with a micro-structured solid surface.

The underlying secrets behind high/low liquid-solid adhesion can be found in the two basic models of wetting, namely Wenzel (rose petal) and Cassie (lotus leaf) states. In the Wenzel state, a liquid can completely fill the grooves of rough structures (**Figure 11a**). A continuous three-phase contact line leads to an increase in the area of solid-liquid contact. Consequently, a liquid droplet can stick to such surfaces even when turned upside down. In the Cassie state, the presence of air gaps gives rise to a discontinuous line of solid-liquid contact (**Figure 11b**). In this case, a liquid droplet can only partially fill the roughness of the structures, and the solid/liquid adhesive force decreases with the area of solid-liquid interface. Decreasing the droplet adhesion, if the surface is tilted, the droplet rolls off.

The physics behind the Wenzel and Cassie states determines the high/low liquid-solid adhesion of the droplet to the patterned surface and it can be modulated by controlling structural parameters of the surface.

In a recent work [53], a series of PDMS-based squared pillars and dimples, with different size, were fabricated and characterized (**Figure 12**).

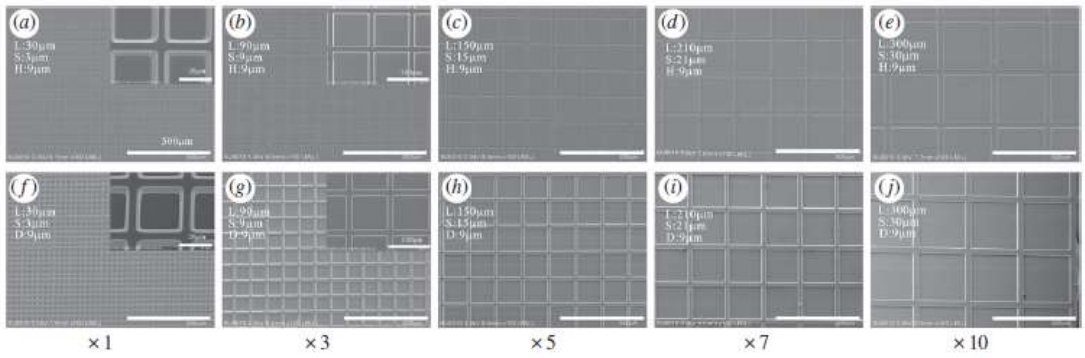

Figure 12 – SEM micrographs showing (a-e) pillars and (f-j) dimples with varying scales. Images adacted from [53]**.**

Different wettability and adhesion behaviour were measured, showing the scale-dependent behaviour both for pillars and dimples. Indeed, increasing the dimension of the pillars and dimples, both geometries show a decrease of the contact angle, and an increase of the adhesive forces. For dimple surfaces, larger contact angles and lower adhesion forces were observed than in pillar based patterns. Moreover decreasing the scale of the geometry, the surface becomes more

hydrophobic and with lower adhesion forces, meaning that this micro-patterning follows a Cassie-state behaviour (**Figure 13**).

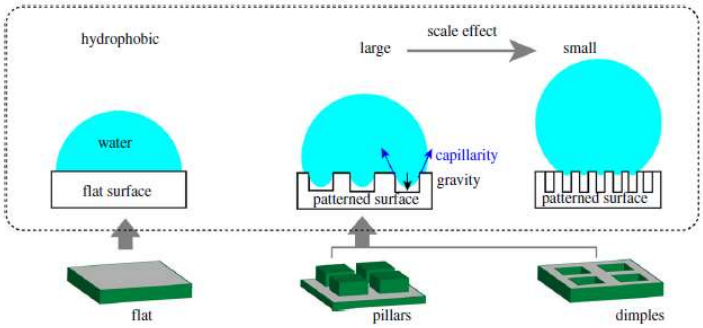

Figure 13 – The influence of pillars and dimples on wettability. Images adacted from [53]**.**

This work was very useful to highlight as different micro-structurations of the surface, depending on the scale and the morphology, produce different behaviour in terms of wettability and adhesion force, and, even more relevant, it pointed out how to modulate these properties by varying the topography.

1.3.2 Surfaces at the interface with biological materials: the importance for tissue engineering

Tissue engineering requires comprehensive efforts to combine engineering with life sciences for the purpose of restoring, replacing, or improving the function of damaged tissues and organs [54], [55]. It is a technological approach in the field of regenerative medicine [56]–[58], while stem-cell science, gene therapy, soluble molecules, and reprogramming of cell and tissue are all topics that join tissue engineering and regenerative medicine.

In tissue engineering, the design approaches can be divided in three types of studies that involve and attempt to reproduce systems composed by cells, scaffolds and a combination of cells and scaffolds [59]. Scaffolds can be fabricated in natural (e.g. collagen, decellularized matrices) or synthetic materials. Their function is to replicate the biological three-dimensional (3D) environment, i.e., the extracellular matrix (ECM), in order to favour the cell proliferation and organization into tissues or organs, at the same time preserving their specialized tissue configuration and reproducing their desired local environment [60]. In addition, synthetic scaffolds must be fabricated with specific properties, such as pore size, geometry permeability, and spatial distribution [61]. The bulk and surface characteristics of scaffold materials may also affect cellular behaviour [61]. Moreover, the natural degradation of the scaffold must be compatible with the normal activity of the cells to avoid early aging.

Since the beginning of the twenty-first century, 2D and 3D printers have been used extensively in medicine and tissue engineering to fabricate biocompatible cell scaffold and culture substrates [62]–[64]. In cardiovascular research, for example, polyester urethane urea was 3D printed as a

cardiac patch for the differentiation and growth of human mesenchymal stem cells and human umbilical vein endothelial cells. The patches were then implanted into rats with induced myocardial infarction, showing increased vessel formation and enhanced heart functionality [65]. In micro- and nanotechnologies, the use of scaffold-based tissue engineering opened many perspectives for regenerative medicine. Scaffolds require specific properties for cells to maintain and regulate their functionality. Micro- and nanotechnologies facilitate the manufacturing of sophisticated scaffolds with different properties, such as pore size, geometry (up to nanometer resolution), and distribution. Nanostructured scaffolds are gaining attention because of their ability to regulate cell functionality [66]. Nanoengineered scaffolds with tailored biochemical, mechanical and electrical properties have been employed to control tissue growth, as they own chemical and physical properties, such as elastic moduli, that allow the cell proliferation and preservation of their functionality [67].

Micropatterning and nanopatterning can control the cellular microenvironment and govern cellular behaviour as surface topography affects cell polarity, adhesion, migration, proliferation and differentiation [66], [68]

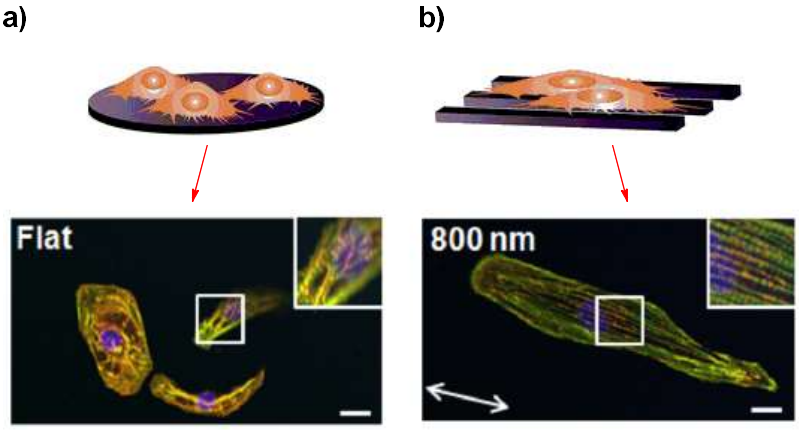

Figure 14 – Schematic illustrations and confocal images of cardiomyocytes on a) flat and b) nanopatterned substrate. Images adacted from [69]**.**

Nanopatterned substrates were extensively studied as cell scaffolds to promote the cellular growth, alignment and maturation of stem cell-derived cardiomyocytes [70], [71]. Stem cells are characterized by their undifferentiated immature nature with any specific intrinsic functionality [72]. Therefore a maturation of stem cell-derived cardiomyocytes *in vitro* toward more adultlike phenotypes is crucial for their employ in heart regenerative medicine. An immature cell with no specific functionality (as typical adultlike cells have), has a circular shape (**Figure 14a**), and it is reported that immature human stem cell-derived cardiomyocytes often have sarcomere lengths of approximately 1.5 µm; while adult cardiomyocytes have sarcomere lengths in the range of 1.8-2.0 µm [73], [74].

Micro- and nanopatterned substrates, characterized by linear nanogrooves, help the structural maturation of cardiomyocytes in a highly efficient way [34]. Human cardiac cells respond to exogeneous structure by orienting themselves into parallel arrays that more closely mimic the structure of the native cardiac cell (**Figure14b**).

1.4 Materials

The main goal of this study was to realize functionalized substrates for different purposes. We focused our attention on patterned surfaces to improve cell adhesion and differentiation, and on reconfigurable surfaces for self-cleaning applications.

Micro-structuration of the surface is the common feature required to control the substrate wettability, and drive cell maturation on biocompatible substrates for tissue engineering applications. In both cases, not only topography results fundamental for the achievement of these scopes but also a tailored chemical composition of the surfaces. Indeed, in the case of self-cleaning devices, chemical functionalization allows to decrease the surface energy and further reduce the wettability; on the other hand, in biological applications biocompatibility of synthetic materials is a primary requirement to ensure the cell adhesion and growth for *in vitro* studies.

In order to fabricate micro-patterned surfaces for cellular growth, we employed poly(ethylene glycol) as hydrogel-based substrate for its well-known biocompatibility and hydrophilicity [75]. Moreover, it is characterized by a stiffness very similar to organic tissues (Young modulus) in the order of 100 kPa [76]. On the other hand, aiming to demonstrate smart reconfigurable surfaces for microfluidic applications, shape-changing materials that deform in response to external stimuli, have been patterned in different geometries to explore the dynamic wettability of surfaces.

1.4.1 Poly(ethylene glycol) as polymeric hydrogel for tissue engineering

A hydrogel is a three-dimensional (3D) network of hydrophilic molecules that swell in water holding a large amount of liquid while maintaining the structure due to chemical or physical cross-linking of individual polymer chains. First examples of hydrogels were reported by Wichterle and Lím in 1960 [77]. By definition, water must constitute at least 10% of the total weight (or volume) of a hydrogel and because of significant enclosed water content and their elasticity, they nicely resemble tissues of living organisms.

Hydrogels undergo a reversible volume phase transition or gel-sol phase transition in response to certain physical and chemical stimuli, such as temperature, electric and magnetic fields, solvent composition, light intensity, pressure, and pH variations. Their use in different fields is motivated

by their isotropic volume change in liquids, responsivity to different external stimuli and biocompatibility.

In tissue engineering, the use of hydrogels composed by biological polymers, like collagen and other extracellular matrix-derived polypeptides, might seem to be an obvious choice. However, these natural hydrogels have undesirable mechanical properties and can induce immunogenic risks [78]. Hydrogels, made by synthetic polymers, are widely preferred and synthetic polymers composed mainly of poly(ethylene glycol) (PEG) are largely employed.

Poly(ethylene glycol) (PEG) is a synthetic, non-biodegradable polymer that can be easily synthesized by the controlled polymerization of ethylene glycol in aqueous solution thus determining the polymer chain length. PEG is biocompatible and thus well-suited for biological studies. Its repeated alkane-ether motif makes PEG not only very hydrophilic, which is important for nutrient and waste transport, but also biochemically inert. PEG is also non-immunogenic and resistant to protein adsorption [79], making it suitable for in vivo as well as *in vitro* studies. However, unlike biological hydrogels, PEG is not biodegradable. As a result, PEG is almost always incorporated in block copolymers with biodegradable polymers, such as poly(glycolic acid) (PGA) and poly(lactic acid) (PLA) [80].

The main advantages of PEG-based hydrogels lie in the versatility of PEG chemistry. All chain lengths of PEG are soluble in water and can be synthesized with low polydispersity. PEG has both a linear structure and a branched (star) structure and its hydroxy end groups can be readily replaced with a wide variety of functional groups [81]. Those end groups can be identical, or different (two different functional groups): this makes PEG extremely versatile, not only in terms of hydrogel architecture, but also for its ability to covalently link different biomolecules [81], [82].

In addition to the control of the chemical composition of PEG, the mechanical properties of a PEG-based hydrogel can also be tuned. Stiffness and porosity, important mechanical factors for the functionality and life of stem cells, are largely determined by the degree of crosslinking among polymer chains. Crosslinking can be achieved through specific chemical reactions, such as Michael-type addition and click chemistry [79]. However, the most prominent method of crosslinking is a free radical mechanism of diacrylate based monomer, as reported in **Figure 15**. In radical conditions, a non-degradable crosslinked structure can be prepared, and this methodology is compatible with many lithographic techniques that allow the hydrogel patterning at the microscale with nanometric resolution [43].

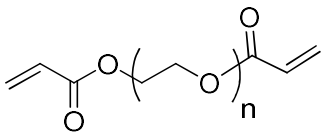

Figure 15 – Molecular structure of di-acrylate poly(ethylene glycol)

PEG hydrogel can be fabricated by photopatterning into 2D-microstructures to study the growth and functionality of cells in tissue engineering applications [83]. On the other side, planar micropatterned geometries can be prepared by soft lithography using PDMS mold in order to improve and control the cellular-growth [84].

1.4.2 Liquid Crystalline Elastomers (LCEs) as smart polymers for different applications

1.4.2.1 General concepts

Liquid crystalline elastomers are smart materials obtained by the combination of liquid crystals molecules within an elastomeric network.

Liquid crystal is a state of matter which has properties between those of liquids and those of solid crystals. It flows like a liquid, but present anisotropic mechanical, optical and dielectric properties as crystalline materials [85].

The most common mesophases of liquid crystals are shown in **Figure 16**.

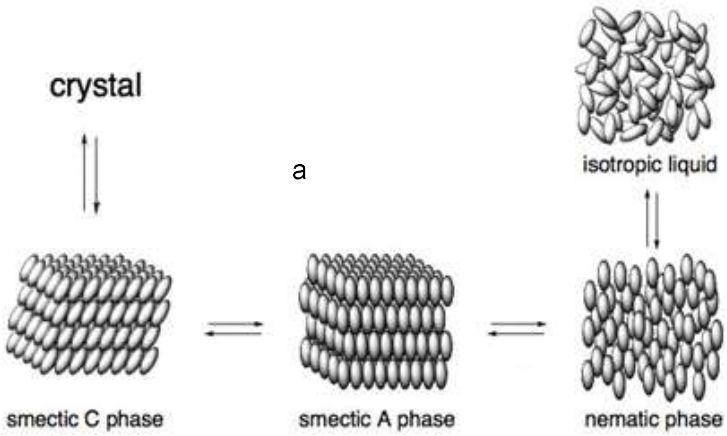

Figure 16 – Examples of mesophases for rod-like LC molecules.

Nematic phase (**N**) is the less ordered liquid crystal phase and presents only orientational order: the long molecular axes are preferentially oriented in one direction, defined as director. Nematic LCs are characterized by a relative low viscosity so they can rearrange under even small external forces. In smectic phases, molecules lay parallel one to the other and they are arranged in layers with the molecular long axis perpendicular (smectic A phase, **SmA**) or tilted (smectic C phase, **SmC**) to the layer plane. Many variations of smectic phases have been identified [86].

Elastomers are polymers that can be easily deformed up to large strains [87] thanks to the moderate cross-linking density of the main polymer chains.

LCEs that are characterized by the liquid crystalline order of molecules and the elasticity of rubbers, are able to undergo a reversible shape change when exposed to external stimuli (**Figure 17**), as a variation of temperature, an electric or magnetic field or when irradiated by light [88]–[90].

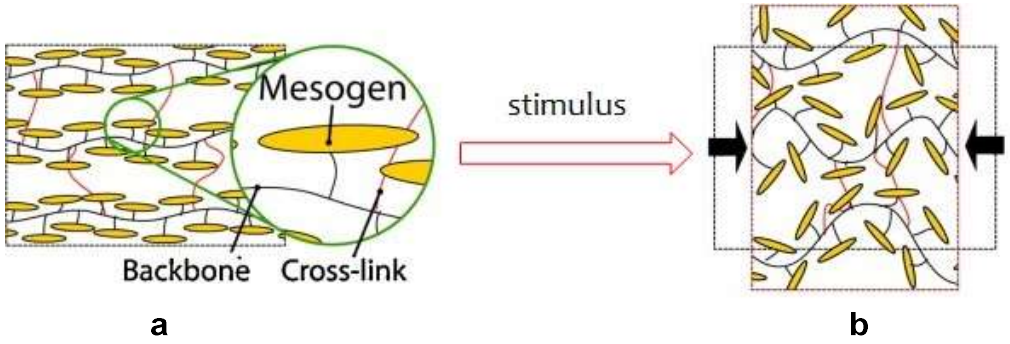

Figure 17 – Macroscopic change of a sample during the N (a) to I (b) phase transition by application of external stimuli. Images adacted from [91].

The polymeric chains, in which the mesogens can be incorporated along the polymer backbone (main chain LCE) or laterally attached to the backbone (side-chain LCE) (**Figure 17a**), present an anisotropic conformation. If the elastomer loses its anisotropy, for example when it is heated up to the isotropic phase, it shows a contraction along the direction of alignment of the mesogens and an expansion in the perpendicular direction (**Figure 17b**). When the stimulus is removed (following the above examples the sample is cooled) it recovers its initial shape.

Different type of deformations can be achieved by programming the molecular alignment of the liquid crystalline units before the polymerization process [92].

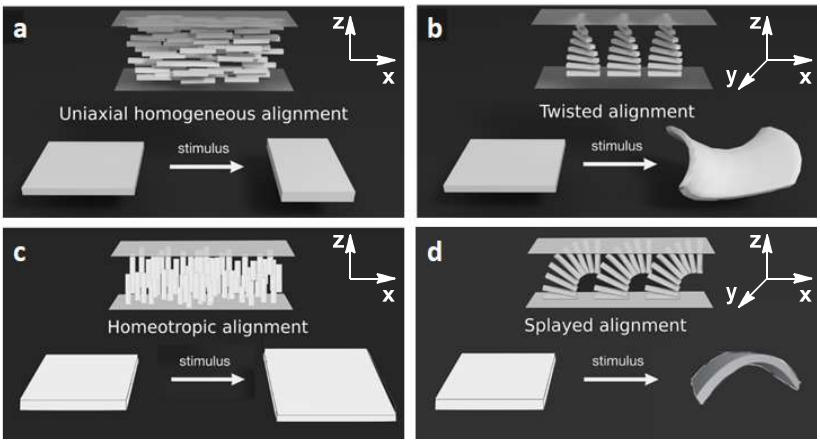

Figure 18 – Different alignments of LC molecules and correspondent deformation under external stimuli.

In homogeneous and homeotropic alignments, the molecules are oriented along one direction and the polymer movement, once the molecular disordering is attained, results in a contraction

along the alignment direction (**Figure18a** and **c**). On the contrary, in twisted alignments the molecules rotate on the *xy* plane along the *z* axis, as shown in **Figure 18b**, causing a torsion of the final polymer under activation; while, in splayed alignment (**Figure 18d**) the molecules switch from homogeneous to homeotropic alignment along the *z* axis, causing a bending of the final polymer.

1.4.2.2 Preparation methods

First examples of LCEs were described by de Gennes in 1969 [93], that studied the possible interaction of a polymer network incorporating molecules with a liquid-crystalline phase. In 1975, he extended these ideas to the specific case of a crosslinked liquid-crystalline polymer [94]. Then, a big impulse in the study of LCEs and in their synthesis was given by Finkelman, that showed how to obtain LCE starting by a linear, nonfunctional polyhydrosiloxane chain, which was coupled with the mesogenic groups and a crosslinking agent in one step by Pt-catalyzed hydrosilylation reaction [95]. Here, the platinum-catalyzed addition reaction of terminal C=C double bonds to Si-H bonds was used to bond the mesogens and crosslinking moieties to the polyhydrosiloxane chains [96] (**Figure 19**).

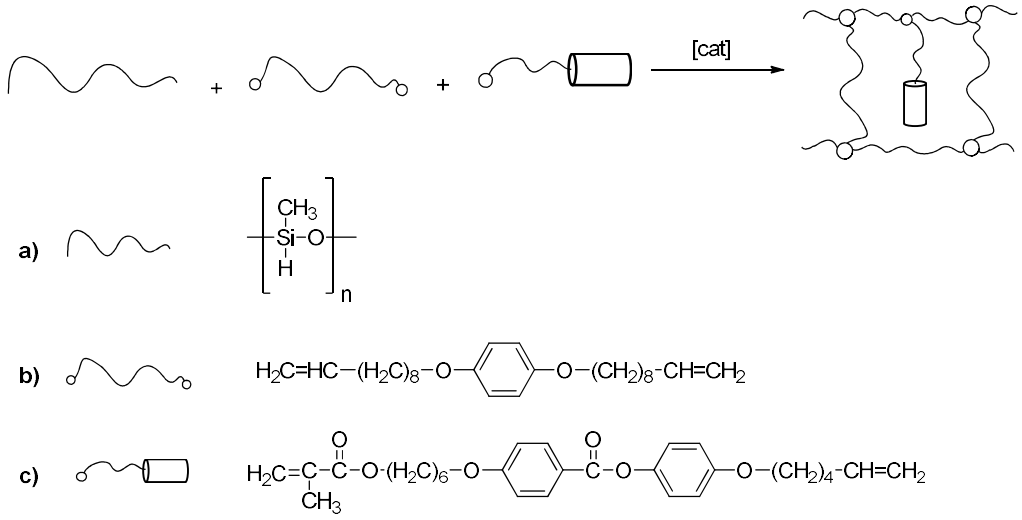

Figure 19 – Reaction scheme for preparation of LCEs using Pt-catalysed hydrosilylation reaction.

With this method, a huge variety of LCE samples were obtained. Moreover, photochromic side-groups were introduced as mesogens in side-chain architectures to obtain photoresponsive polymers [97], [98]. Also main-chain polymers have been prepared by silicone chemistry, performing the reaction with divinylic monomer and tetramehyldisiloxane in a polycondensation reaction [99]. Within the latter strategy, the alignment of the mesogens is performed by a mechanical stretching of the final polymer, thus, samples with big size can be easily prepared. At the same time, the mechanical alignment introduces some drawback as only a homogenous LC alignment can be programmed, and it cannot be employed for micro-structures. Free-radical

polymerization solved these issues and, in particular, photopolymerization of acrylate (methacrylate) functionalized mesogens is actually a common way to obtain LCEs at different length scales. In this synthetic strategy, a monomer mixture, composed by LC monomers and multifunctional cross-linker, leads to the formation of a liquid crystalline network (**Scheme 3**) by the simultaneous growth of different chains and their crosslinking.

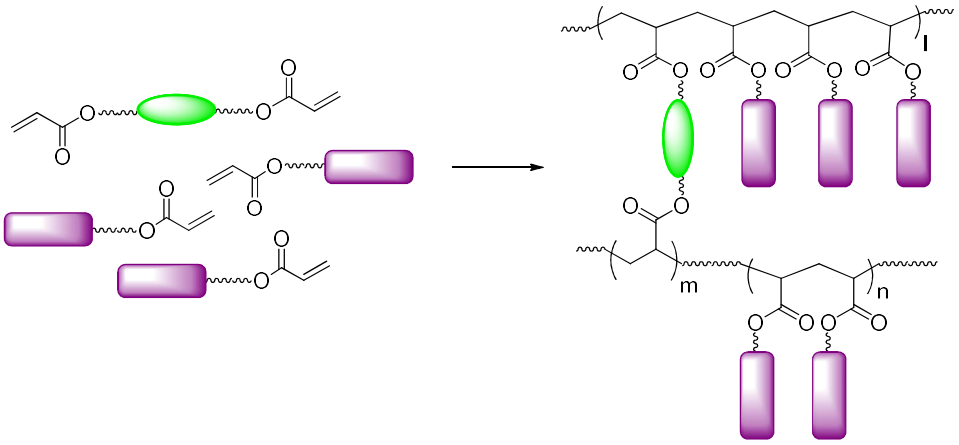

Scheme 3 - Synthesis of a LCE using free radical polymerization of acrylate based monomers.

Free radicals can be produced through application of heating, irradiation with light or a redox agent with the relative initiation of the polymerization process. Light in the ultraviolet or visible range can break selected bonds, thereby forming free radicals and allowing the polymerization process at a choice temperature [100]. This aspect is fundamental in the LCE preparation where the monomer mixture must be aligned in the nematic phase before polymerization. The temperature is maintained in a selected range in which the LC phase is present and stable and, only at this moment, the polymerization can occur leading the formation of a LCE. This synthetic strategy allowed to design the LC orientation also at the micro scale by photo-alignment techniques [101] or physical interactions with microstructured surfaces [102] in order to achieve complex deformations.

A wide range of examples reports the use of acrylate-based photopolymerization to obtain LCEs [103], [104].

This techniques has been also used to fabricate thermoresponsive micro-pillars by soft-lithography [105] obtaining the desired LC alignment by application, before polymerization/cross-linking, of an oriented magnetic field on the nematic mesophase. Single micro-pillar showed a contraction (in the order of 30-40%, **Figure 20a-c**) in response to small temperature changes around a well-defined transition temperature. The cylinders went back to their original size after cooling them below the isotropic to nematic transition temperature.

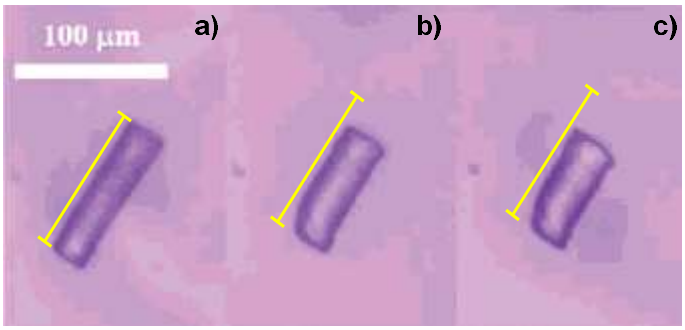

Figure 20 - An isolated pillar heated (from left to the right, the temperatures are 100, 120, and 130 °C) exhibits a contraction along its major axis of the order of 35%. The yellow bars show the initial length of the isolated cylinder. Images adacted from [105]**.**

These microstructures respond only to temperature changes, limiting their application to the use in high boiling solvent (such as glycerol), while this work highlights the potential applications of micro-structured LCE in the field of micro-fluidics and micro-robotics at room temperature.

The introduction of a chromophore inside the LCE network allowed the fabrication of photochemically driven LC elastomeric systems. Many examples of acrylate-based monomers with photochromic groups have been described, in particular by using azobenzene derivatives [106], [107], [108], and a radical UV initiator. The light-driven material deformation is a consequence of the light absorption by the dye which induces a by nematic to isotropic transition of the system. In most cases, the systems undergo material bending, caused by the partial penetration of the light inside the material (and then to unsymmetrical material deformation). To solve this problem, Li & co-workers realized a material in which an azodye is incorporated inside the LC monomer (**Figure 21a**), showing a fast photochemical contraction (less than 1 min) of the polymer up to 18% along a preferred orientation (**Figure 21b** and **c**) [90].

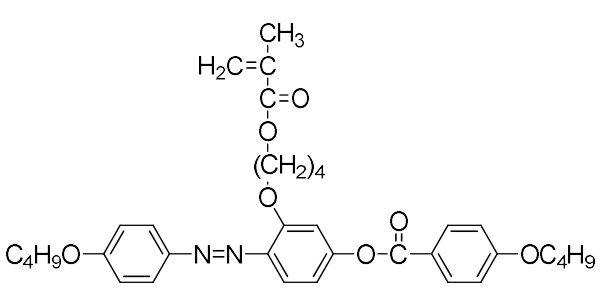

a)

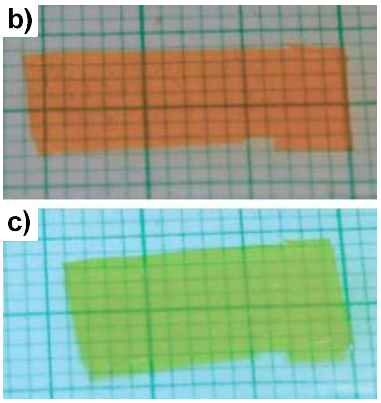

Figure 21 – An azo-containing methacrylate monomer (a) allowed to obtain polymers that contract along a preferential direction when exposed to UV light (b-c). Images adacted from [90].

In our research group, different examples both for robotics [109]–[111], photonics [112], [113] and biological applications [114] have been published using photopolymerization of acrylate functionalized mesogens.

A synthetic strategy based on the photoinduced addition of thiols to olefins was used to prepare new LCEs [115], [116] and, finally, its sister reaction, based on the click-coupling between thiols and alkynes, was recently used to prepare the first example of LCE with a large contraction (around 40%) [117].

Depending on the monomers and crosslinker used during the preparation of LCE, it is possible to obtain three different material architectures (**Figure 22**).

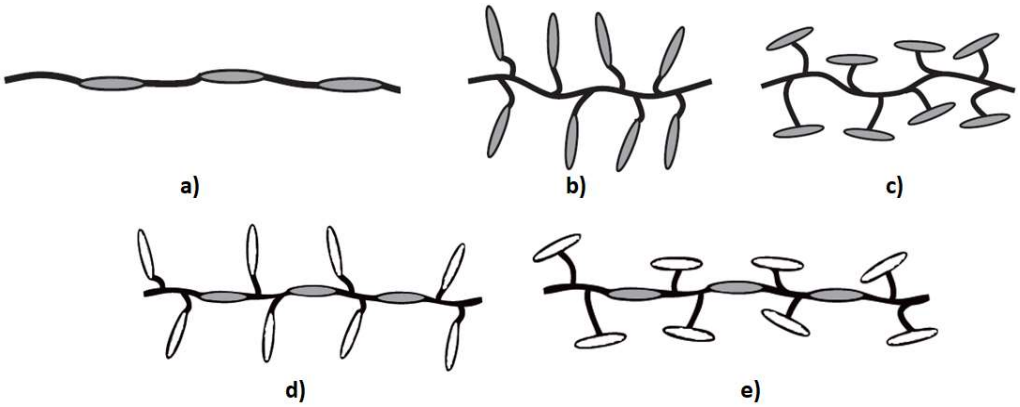

Figure 22 – Possible architecture obtained using LCEs.

In **Figure 22a**, the mesogenic molecules are incorporated in the backbone of the polymer architecture, to produce main-chain architecture. Otherwise, the mesogens can be attached to the backbone with a spacer to have side-chain polymers, that can be subdivided in “end-on” architecture, where the rod-like mesogens are attached via their long axis (**Figure 22b**) and in “side-on” type polymers, where they are attached via their short axis (**Figure 22c**). Finally, both structural principles can be combined to prepare mixed main-chain/side-chain polymers (“combined” LC polymers, **Figure 22d-e**) [118], [119].

Versatility of acrylate chemistry also opened to of LCEs manufacturing with specific fabrication techniques. Patterned LCEs, with high reproducibility and over centimeter scale distances, were fabricated by replica molding in a short time in 2D geometries [120]; while, for micro-fabrication of 3D structures, Direct Laser Writing technique was demonstrated as a useful tool to prepare LCE structures in arbitrary shapes with high resolution (about 200 nm) [121].

Chapter 2- Micro-structured surfaces with photoresponsive properties

2.1 Introduction

As mentioned in Chapter 1, surface micro-structuring is one of the most promising strategy to obtain self-cleaning materials. Surface properties are determined by multiples factors, and their hydrophobic/hydrophilic behaviour can be regulated by the topography and morphology of the micro pattern, the chemical treatment or the coating.

Nature is a fascinating source of inspiration. Plants during their evolution found a plethora of functional solutions to exploit and save water, e.g. by reduction or increase of leaf surface wetting and adhesion properties. Such behaviour is usually determined by the complex micro-structuration of plant epidermis cells, that has been engineered by nature to create superhydrophobic leaves.

For example, **Figure 23** shows the structure and wetting properties of a Lotus leaf. A hierarchical (i.e. structuration of the surface at different length scales) geometrical modulation is present on the leaf surface (SEM images in **Figure 23a**) as well as in many other superhydrophobic leaves (e.g. the rice leaf, the rose petals).

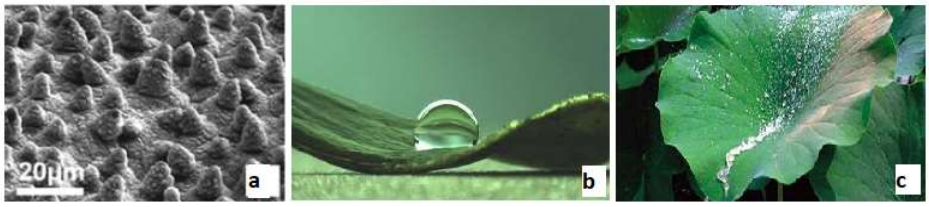

Figure 23 – Superhydrophobic and self-cleaning surfaces engineered by nature. a) SEM micrograph of the Lotus leaf surface shows randomly arranged micro-structuration at different length scales. **b)** A spherical water droplet on a superhydrophobic leaf that results in **c)** the self-cleaning behaviour thanks to the interplay of high superhydrophobicity and low surface energy.

Thanks to this micro-structuration, the leaf wettability is minimized. Air is trapped in the cavities of the convex cell and the hierarchical roughness enlarges the water-air interface while the solid-water interface is reduced. Water on such a surfaces forms spherical droplets (**Figure 23b**) that can roll off when the leave is tilted, with a consequent self-cleaning phenomenon (**Figure 23c**). This behaviour has been extensively studied focusing on the requirements for strong and directional adhesion, superhydrophobicity, and self-cleaning in static and isolated configurations [2], [7], [8].

In this work, we aim to study and fabricate reconfigurable surfaces whose hydrophobic/hydrophilic properties can be locally and selectively switched by an external stimulus. The actuation source that we chose is light because of its non-invasive and remote control, its various degrees of freedom (wavelength, polarization, intensity) and the possibility to modulate its profile intensity in space and time. The material of choice is a liquid crystalline

polymer that enables a photo-response and a consequent shape change behaviour in a controlled manner. In Chapter 1, the properties of these materials have been introduced and herein, we investigated the possibility to use them to create superhydrophobic surfaces with a light modulated wettability.

2.2 Light responsivity of liquid crystalline networks: photo-thermal effect and isomerization

The conversion of light energy into mechanical work is a promising tool for powering systems in a clean, cheap and environmental-friendly way.

Light conversion into mechanical deformation requires molecules that interact with the radiation by different mechanism such as undergoing different chemical reactions (e.g. isomerization) or dissipating energy into heat. Different photoswitches have been studied for this purpose such as azobenzenes, stilbenes, spiropyrans and fulgides, while regarding the polymeric matrix, liquid crystalline polymers are the most employed.

In azobenzene doped LC polymers, the resulting guest/host system isothermally undergoes phase transition under light irradiation that induces a photochemical reaction of the dye [122]. Azobenzenes can be reversibly isomerized between their two geometric isomers (*trans* and *cis* forms): using light of appropriate wavelength [123].

In case of not-substituted azobenzene, for example those shown in **Figure 24**, the *trans* and *cis* isomers display well-separated absorption bands in the UV-Vis spectra (**Figure 24b**), and different physical-chemical properties, such as molecular geometry, dipole moment or absorption spectrum [124], [125], [126]

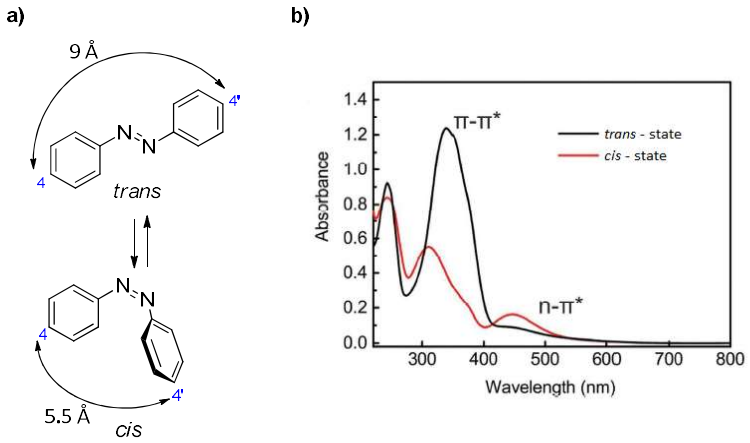

Figure 24 – Chemical structure (a) and absorption spectra (b) of *trans* and *cis* azobenzene.

A careful analysis of the azobenzene isomer absorption spectra gives a meaningful insight of the chemical physical process of isomerization. A typical UV-Vis spectrum of *trans*-azobenzenes, or

(*E*)-azobenzenes (following the *E-Z* nomenclature), shows an intense band around 320 nm, which corresponds to the π-π* symmetry-allowed transition, and a weaker band in the visible region around 450 nm, which corresponds to the symmetry-prohibited n-π* transition. Regarding *cis* isomer, or (*Z*)-azobenzene, the absorbance profile shows a strong absorption band in the UV around 300 nm and a weaker band in the visible region around 450 nm. These bands correspond to the same transitions explained for the *trans* form. Exploiting the differences in the absorption spectrum of the two isomers, the isomerization process could be activated with UV light, for *trans* → *cis* conversion, and visible light, for the reverse process. Moreover, *cis* isomer can also relax back spontaneously to the thermodynamically stable *trans* form in the dark isothermally. The two photochemical conversions occur in the scale of picoseconds, while the thermal relaxation is much slower and depends on the lifetime of the *cis* state (milliseconds to day) [127].

The *trans* isomer has a rod-like molecular shape and it is 10-12 Kcal mol^{-1} more stable than *cis* one; consequently, in the dark at the equilibrium, the *trans* is the dominant isomer (99.99%). The isomerization process involves a change in geometry from planar to bent, a decrease in the distance between the two carbon atoms in position 4 and 4' of the aromatic rings (from 9.0 Å in the *trans* to 5.5 Å in the *cis* isomer), and a consequent change in dipole moment (from less than 0.5 Debye in the *trans* form to 3.1 Debye in the *cis* form). The geometrical rearrangement allows to avoid steric repulsions in between the π clouds of two aromatic rings [128].

Azobenzenes doped LCEs have been first exploited by Finkelmann and co-workers to obtain photoresponsive actuators. They described as nematic LCEs with polysiloxane main-chain and an azobenzene crosslinker show a contraction of 20% along the LC director axis [98] when exposed to UV light. Later on, many other authors described photoresponsive LCE devices having different shapes for a variety of applications, of notice the robotic elements able to use light as fuel for locomotion and action at different length scales. Combining light responsive LCE with different lithographic techniques, such as UV and soft lithography opened also to the preparation of microscopic actuators [109]–[111].

As example, artificial cilia have been fabricated by an inject printing method and shown an asymmetric motion by tuning the irradiation conditions, as represented in **Figure 25** [108].

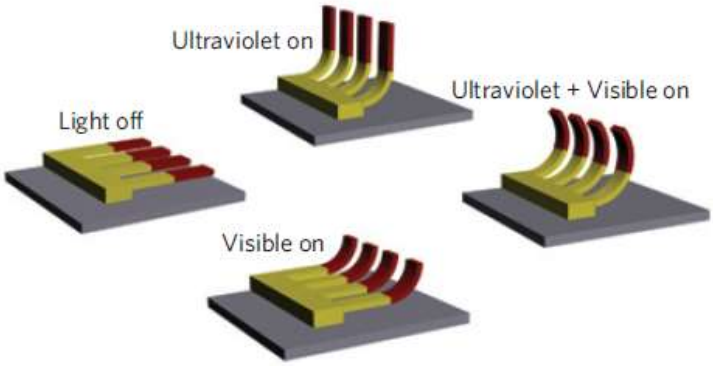

Figure 25 - Asymmetric motion of artificial cilia fabricated with crosslinked photochromatic LC polymers by controlling the irradiation conditions. Images adacted from [108].

The first LCE microrobot entirely powered by light, a microscopic walker, was fabricated by a two-photon photopolymerization process promoted by a femtosecond laser beam (Direct Laser Writing) [109]. The locomotion of such device is caused by the light absorption, in the visible range, of the azo dye contained in the LCE. To be noticed that in the last example (and not in the previous one), the movement is mostly induced by a light-induced thermal effect: the energy of the absorbed light is transformed into heat and the temperature increase leads to LC disordering and material deformation. [129]

Technological advances in microrobotics can also be exploited to obtain functional surfaces. Both photochemical and photothermal effect can be investigated to tune the wettability properties of LCE-based surfaces depending on the specific desired application. However, when water is the solvent of interest, the photothermal effect can generate the droplet evaporation and the photochemical one represents the desirable solution to modulate the surface properties.

In this Chapter, different micro-structured surfaces made by photoresponsive LCE materials have been fabricated and characterized in terms of wettability and light response. A local and programmable photoinduced change in the surface hydrophobicity would be used to create re-writable microfluidic channels for microdroplet manipulation, opening to dynamic self-cleaning and microfluidic applications.

This wettability characterization was done in collaboration with the group of Dr. Silvia Vignolini of the Chemistry Department of the University of Cambridge.

2.3 Results and discussion

2.3.1 LCE mixtures for micro-structure photoresponsive surfaces

In order to obtain photoresponsive micro structured surfaces, a preliminary study was pursued to identify the best mixture for fabrication and light induced deformation. In particular, we choose

two different acrylate-based mixtures that mainly differ for the mechanism of their photoresponsive behaviour (due to the different dye used). Both mixtures are characterized by the presence of a LC monomer functionalized with an acrylate group, responsible for the formation of the polymeric chain, a cross-linker which allows the formation of the network with the elastic response, a photoinitiator, to promote the radical polymerization by light (needed to integrate the material preparation with standard lithographic techniques). Furthermore, an azo dye was introduced to obtain a photosensitive polymer.

Previous studies of our research group [121], [130], [109], showed as the mixture **Mix1**, reported in **Scheme 4**, allows to obtain good resolution for microfabrication with different lithographic platforms.

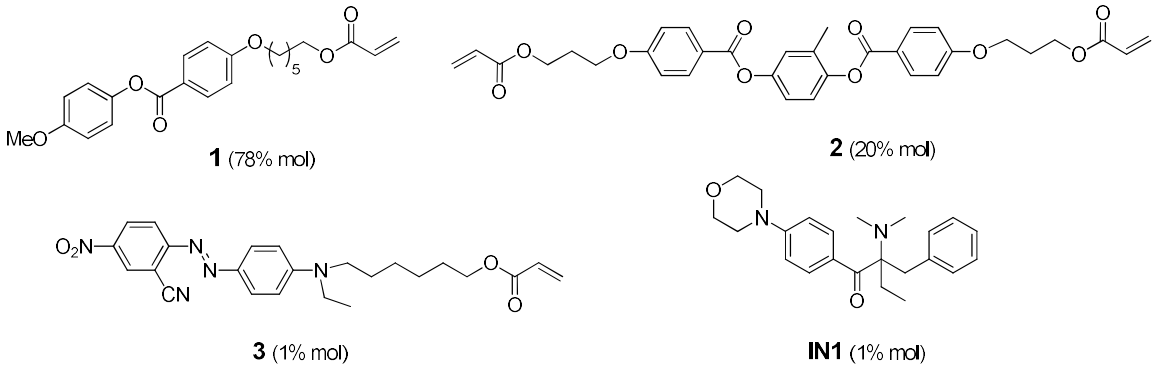

Scheme 4 – Chemical structures and correspondent % mol/mol (in bracket) of the monomers used for Mix1.

In **Mix1**, **1** and **2** are both liquid crystalline monomers and **3** is a push-pull azo dye with an absorption peak in the visible range (**Figure 26a**), allowing for material activation under green light (532 nm). Photoinitiator **IN1** promotes the photopolymerization by UV illumination (385 nm).

Observation by polarized optical microscopy (POM) of the liquid mixture showed a nematic phase around 60 °C. The nematic mesophase was diagnosed through a *Schlieren* texture, with two and four dark brushes (**Figure 26b**). Transition temperature is also confirmed by the DSC traces reported in previous work [131]. On cooling, the mixture displays the isotropic-nematic transition (T_{NI} = 57 °C) and the nematic phase remains stable at room temperature for hours. For this reason, the mixture represents a good candidate for lithographic processes in which the nematic alignment has to be kept stable at room temperature during the entire printing process.

Introduction of the push-pull azo dye **3** allows to control the shape-change of the material thanks to a light induced thermal process which induces a LC-isotropic phase transition. The polymer recovers its original shape when the light source is switched off (**Figure 26c-g**). We can assume this step as synchronous with the switching off of the illumination since the thermal relaxation processes last in tens of milliseconds. Detailed studies on the deformation mechanism has been

previously conducted by using an infrared thermo camera imaging [132], [133] demonstrating how the photoinduced energy dissipation plays a major role in the activation.

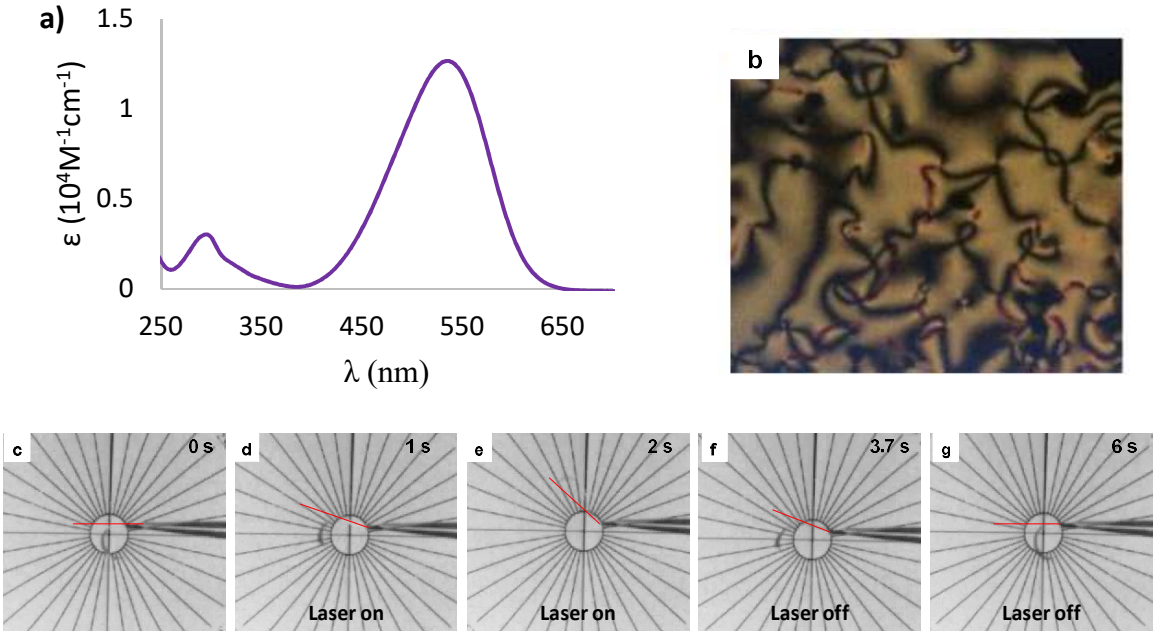

Figure 26 – a) Absorption spectrum of dye **3**, with a maximum absorption at λ = 540 nm **b)** POM image of **Mix1** at 53 °C, in which the *Schlieren* textures show the nematic phase of the mixture **c-g)** Photoresponsivity of the elastomeric film obtained with **Mix1** with a splayed alignment. The bending of the film is generated by LC disordering induced by the thermal effect induced by light. The red bar highlights the sample position. Time evolution is monitored.

The second mixture used in this study is **Mix2** showed in **Scheme 5** and containing a symmetrical di-substituted azo dye.

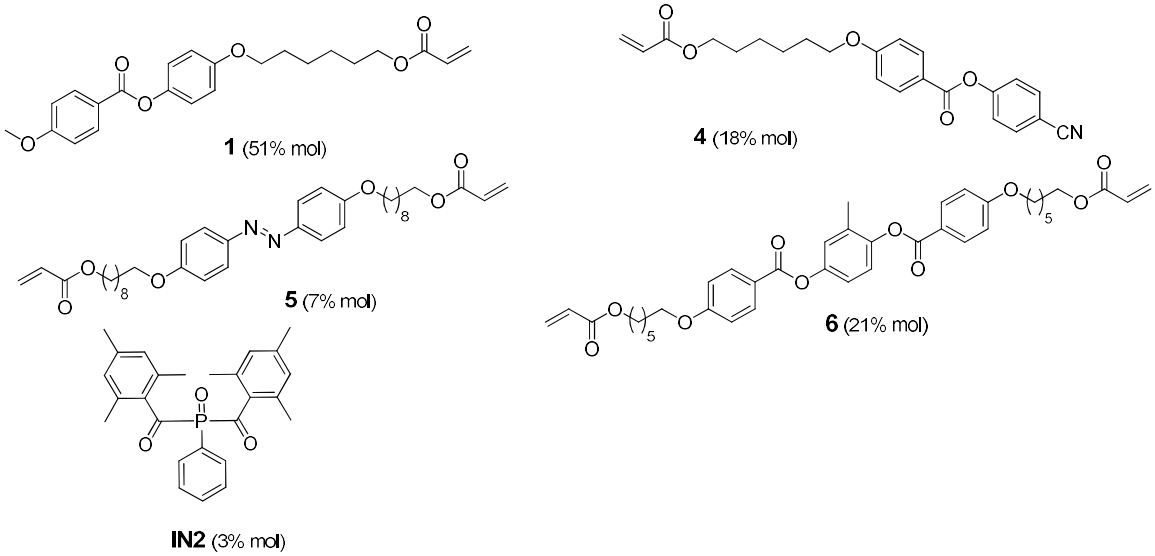

Scheme 5 – Chemical structures and correspondent % mol/mol (in bracket) of the monomers used for Mix2.

Di-acrylate **6** is a crosslinker used to balance the mechanical properties of the polymer. Its concentration is adjusted to obtain a glass transition temperature of the final polymer network

above room temperature (80° C) [10]. Monomers **1** and **4** enhance alignment properties and optimize the elastic properties of the LCE on light-induced deformation. Di-acrylate **5** acts both as dye and crosslinker and induces the deformation by its photochemical isomerization [10]. The use of such dye determines larger deformations then mono-acrylate based azobenzene, since the dye is connected to the polymer network at both ends and it is able to directly deform the surrounding network during the *trans-cis* isomerization [134]. Photoinitiator **IN2** was chosen to activate the polymerization by wavelengths >400 nm, preventing premature azobenzene isomerization during the material preparation.

The liquid crystal properties of the unpolymerized mixture were checked by POM, founding a nematic phase (**Figure 27**) between 40 °C to 70 °C.

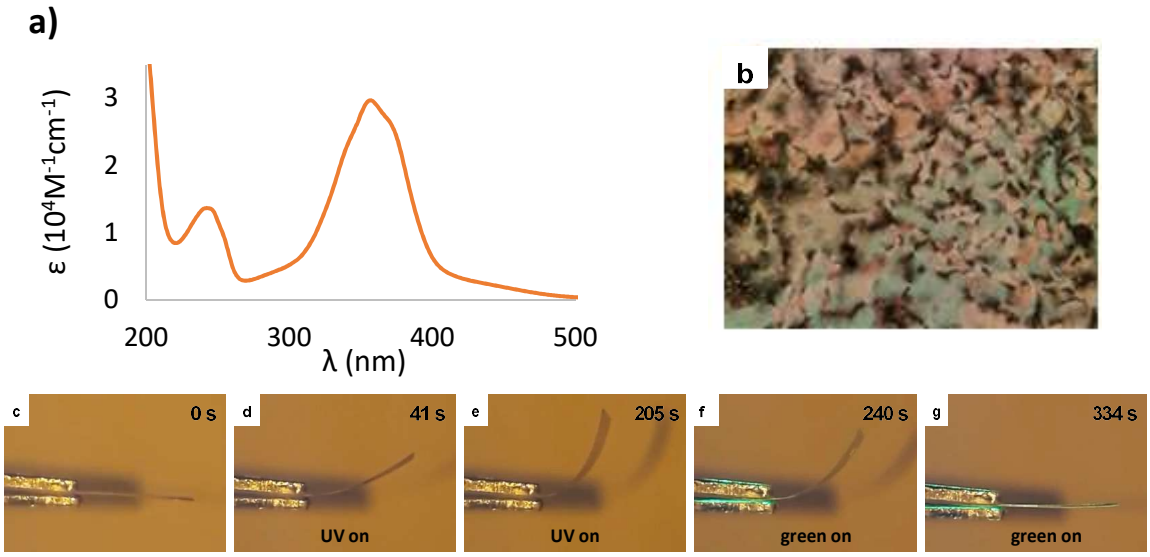

Figure 27 – a) absorption spectra of **5** dye with a maximum absorption at λ = 356 nm **b)** POM image of **Mix2** at 50 °C **c-e)** Photoresponsivity of a splayed-aligned film obtained with **Mix2**. The bending of the film is a consequence of *trans-cis* isomerization of **5** azo dye during the exposition at UV light **(f-g)** The recovery of the initial state is caused by irradiation with a wavelength in the visible region at 505 nm. Time evolution is reported.

Dye **5** leads to a different light responsive behaviour with respect to **3** (**Figure 27a**). Trough irradiation with a UV lamp (380 nm) the dye isomerization generates a macroscopic material deformation, and after switching off the sources, the deformation remains fixes thanks to the stability of the *cis* isomer. Only using green light irradiation or heating the sample, the back *cis-trans* isomerization is obtained and the material recovers the original shape (**Figure 27c-g**). Comparing **Figure 26 c-g** and **27 c-g** is immediately clear that the activation and relaxation processes for dye **3** and **5** are ruled by two different dynamics. In the first case, the light-induced thermal response happens in few seconds while isomerization needs longer irradiation time (minutes for dye **5**) with two different wavelengths.

2.3.2 Fabrication of PDMS mold

Micro-patterned surfaces were fabricated by soft-lithography, previously described in Chapter 1. Starting from different microstructured silicon masters, that differ in the size and the shape of the micro-pillars, the pattern is replicated by an elastomeric mold. This was realized by Silgard 184, a polydimethylsiloxane (PDMS) [24], [36] based material chosen for its low surface energy (about 20 $mN \cdot m^{-1}$ [135], in contrast of other elastomers having surface energy around 34 $mN \cdot m^{-1}$. The low surface energy favours the detachment from the silicon master and from the replicated micro-structure without any pre-treatment [136].

Micro- and nanoscale imprinting with soft molds does not require high pressure [137] during the replication thus opening to its application also on curved or flexible substrates [138], [139].

The PDMS molds were obtained by a standard procedure [140], [141] and in **Figure 28** some optical images of the PDMS substrates are shown.

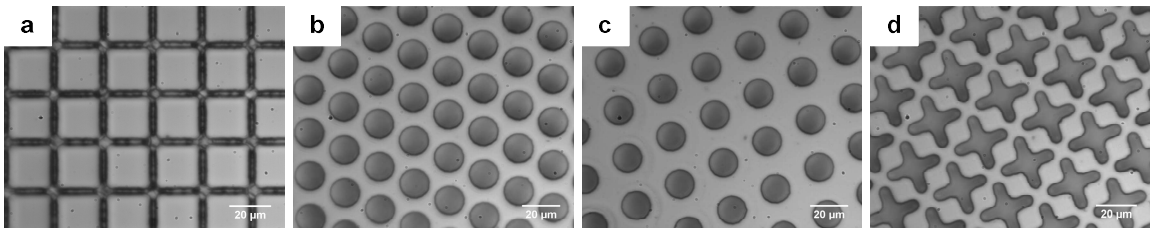

Figure 28 – Optical images of PDMS mold acquired with an objective 50x. a) sample **1**: square section 20x20 µm **b)** sample **2**: circular section with a diameter of 15 µm and center to center distance of two pillars of 20 µm **c)** sample **3**: circular section with diameter of 15 µm and center to center distance between two pillars of 24 µm and **d)** sample **4**: four-point star section with a length of the long side of the star of 29 µm.

We choose to fabricate different geometries to investigate how the surface morphology influences the wettability and adhesion behaviour of the patterned substrates [53]. The selected shapes have square (sample **1**), circular (samples **2** and **3**) and four-pointed star section (sample **4**) (**Figure 28**). Moreover, for the circular section, the center to center distance among pillars was varied to evaluate how this parameter can affect the superhydrophobicity.

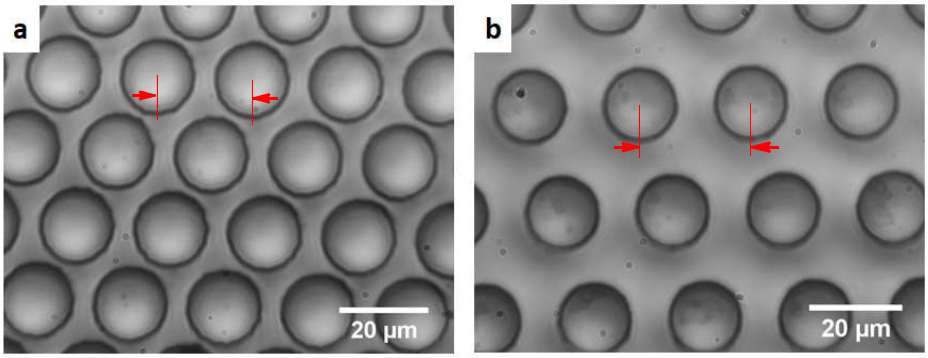

Figure 29 – Optical image of the sample2 (a) and sample3 (b) with an objective 50x.

In **Figure 29** the optical images of the silicon master for samples **2** and **3** are showed. The distance in between adjacent pillars was evaluated: for sample **2** (**Figure 29a**) the distance is about 20 µm

and the diameters of the circles are 15 µm, while for sample **3** (**Figure 29b**) the distance is about 24 µm while the diameter is the same. The PDMS mold replicates with high fidelity the design of the silicon master.

2.3.3 Fabrication of micro-structured surfaces

PDMS mold was used to replicate the LCE-based micro-structures and the different steps for the LCE pattern fabrication are reported in **Figure 30** and as described in previously works to obtain LCE-based micro-actuators [105], [142].

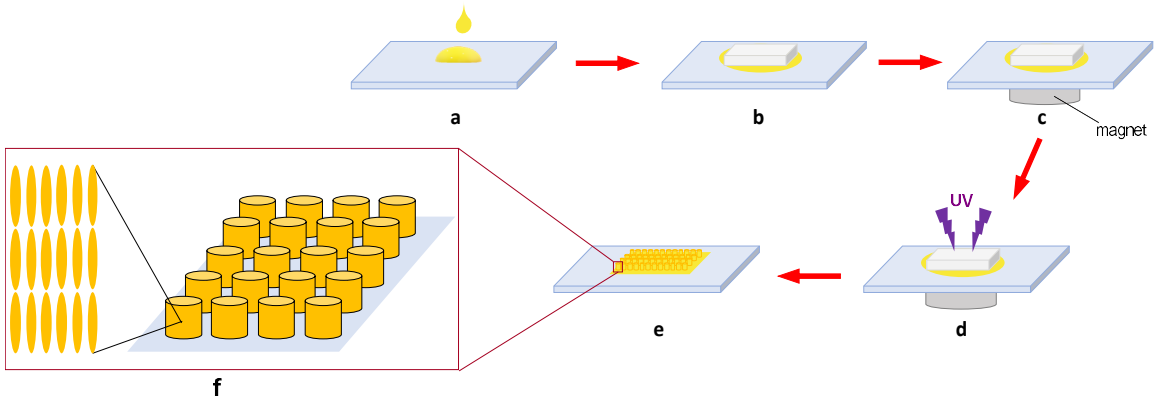

Figure 30 - Schematic illustration of the fabrication of micro-pillars using soft-lithography. a) Deposition of a small amount of the LCE precursor on a microscope slide at isotropic temperature **b)** PDMS mold is casted on the mixture and pressed on it during the infiltration of the LCE mixture into the holes **c)** the alignment of the mesogens inside the holes is performed by a magnet at nematic temperature of the mixture **d)** photopolymerization of the mixture is done using a UV source **e)** obtainment of a micro-structured area on the glass surface after peeling off the PDMS mold

A small amount of LCE mixture, positioned on a microscope slide (**Figure30a**), was infiltrated inside the holes of the PDMS master (**Figure 30b**). Infiltration time was tested: infiltration for 10 minutes at the isotropic temperature (80°C for **Mix1** and 100°C for **Mix2**) creates not well-defined structures (**Figure 31a and b**); for this reason, infiltration time was increased up to 20 minutes for both mixtures. A gentle pressure on the top of the PDMS master is necessary to remove air bubbles.

In order to obtain dynamic surfaces, each micropillar should have a uniform homeotropic alignment in order to create a net deformation under light irradiation. Therefore, the nematic director should be parallel to the symmetry axis of the pillars, as showed in **Figure 30f**. However it is not trivial to obtain an homeotropic alignment inside pillars with 60 micron height [143]. In micro-patterned PDMS mold, alignment can not be controlled by a sacrificial layer, typically used in glass LC cells. To orient the mesogens along a preferential direction we decided to employ a magnetic field [144] via a small permanent magnet (**Figure 30c**) before the polymerization/cross-

linking step. The mixture was pre-aligned at the nematic phase temperature (45°C for **Mix1** and 55°C for **Mix2**) for 20 minutes and then photopolymerized with a UV-source (385 nm for **Mix1** and 405 nm for **Mix2**) for 1 hour, leaving the sample on the magnet at the nematic phase temperature (**Figure 30d**). After cooling to room temperature, the PDMS mold was gently peeled off from the substrate (**Figure 30e**), ending up in a glassy polymer film covered by a regular array of pillars, as shown by POM and SEM pictures (**Figure 31c-h**).

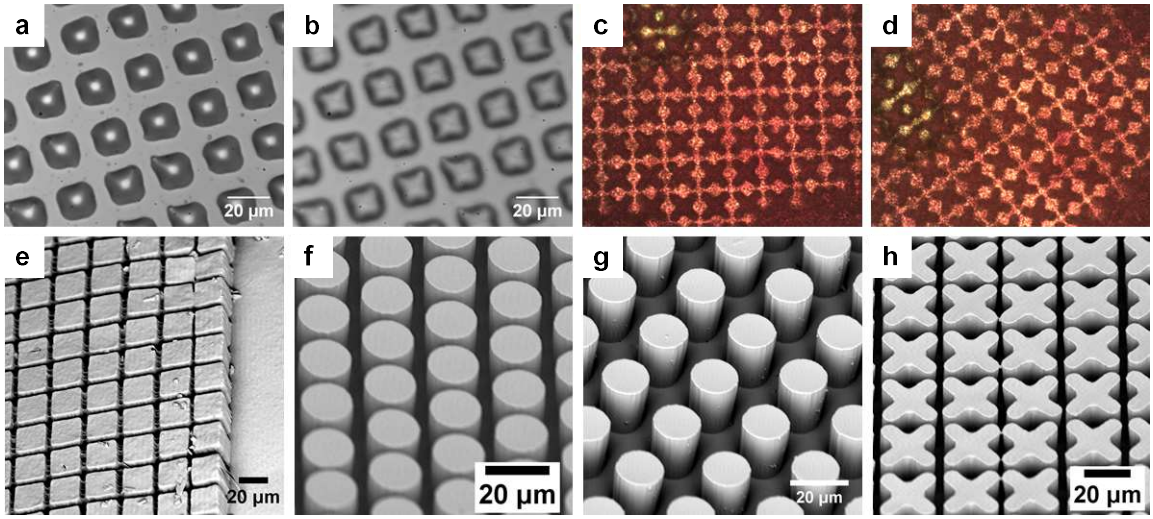

Figure 31 – Optical, POM and SEM characterization of the micro-structured surfaces. a-b) Optical images of the microstructures obtained with a too low infiltration times **c-d)** POM images of the micro-pillars **e-h**) SEM pictures of micro-structured surfaces. The height of the structures is 21 µm for squares and four pointed stars and 28 µm for circles. .

The POM pictures of a polymerized sample obtained with **Mix1** show a good alignment, since the structures are dark for different orientation of the sample with respect to the axis of the crossed polarizers(**Figure 31c** and **Figure 31d**). The POM images thus demonstrate as the LC director inside the pillars is perpendicular to the substrate. Moreover the structures are well defined, except for some defects that can be appreciated in the SEM pictures for the square structures (**Figure 31e-h**).

In **Figure 32,** the optical images of the silicon master (**Figure 32a**), PDMS mold (**Figure 32b**) and LCE micro-pillars (**Figure 32c**) of sample **4**, are shown. To evaluate the difference in size from the silicon to the replicated PDMS and final structures in LCE, the measure of the long side, *d*, of the star was taken (the red lines indicated in **Figure 32a**) and compared. Such dimension scales from 29 µm in the silicon master, to 27 µm PDMS mold and the final structure of LCE micropillar has a size of 26 µm. This reveals as during the different lithographic steps there is a shrinkage of the final structures with respect to the starting design for the four-point star geometry.

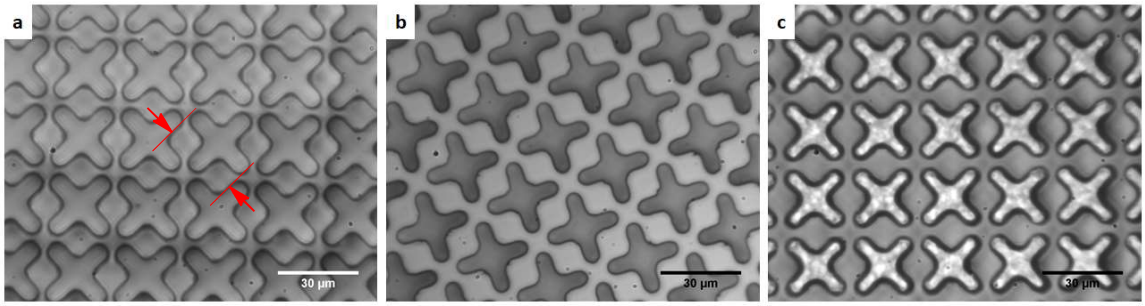

Figure 32 – Optical images of samples 4. Images of the silicon master (**a**), the PDMS mold (**b**) and the LCE structures (**c**) in which the pillar dimension is evaluated along the different lithographic steps**.** The long size d of the star, measured for silicon master (**a**), PDMS mold (**b**) and LCE structures (**c**), is equal to 29 µm, 27 µm and 26 µm respectively.

Unfortunately, the micro-pillars obtained with **Mix2** do not show the desired homeotropic alignment, as demonstrated by the POM images in **Figure 33**. Even if different strategies (as increasing the magnet field or bringing the mixture to the nematic phase by several slow heating-cooling cycles) were investigated, the alignment was not improved.

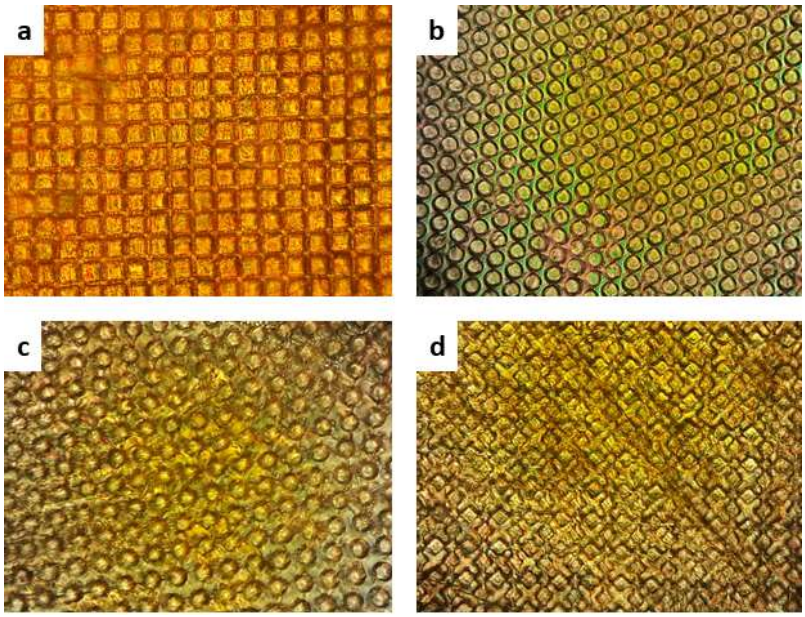

Figure 33 – POM pictures of LCE-based micropillars for obtained with Mix2 for every sample.

In the next paragraph, the polymerized samples will be indicated with the following nomenclature:

- **T0x** for samples obtained with **Mix1**
- **O0x** for samples obtained with **Mix2**

Where x indicates the type of morphology:

- **1**, for square section
- **2**, for circular section with the shorter pillar pitch
- **3**, for circular section with the larger pillar pitch
- **4**, for four-pointed star section

In **Figure 34** other optical images of microstructures obtained with both mixtures are shown.

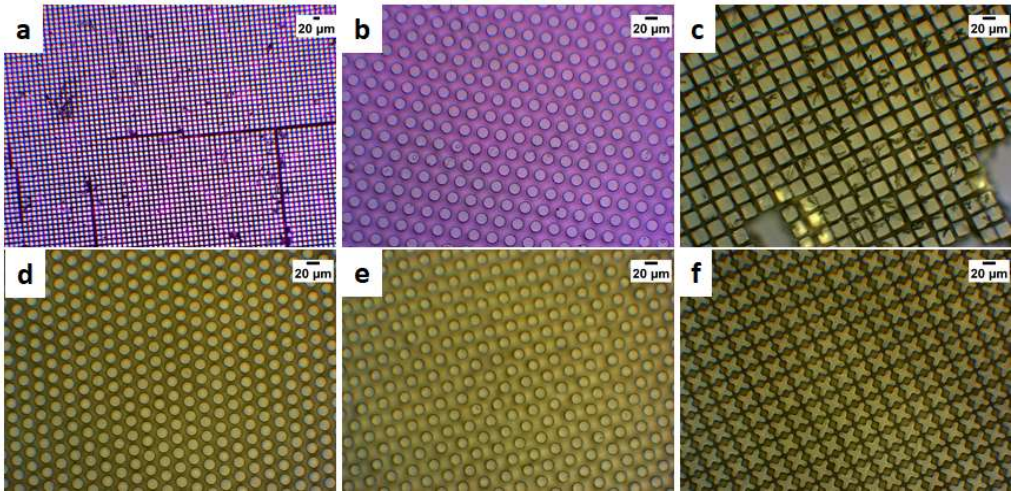

Figure 34 – Optical images of micro-pillars obtained with Mix1 (a and b) and Mix2 (c-f)

All samples present a 1x1 cm patterned area.

2.3.4 Photo-responsive characterization of micro-structured surfaces

Surface deformation under irradiation was evaluated. The samples obtained by **Mix1** were observed by an optical microscope with a 20x objective and actuated by a laser source at 532 nm with a power of 62 mW (power density = 0.77 mW μm^{-2}). In **Figure 35,** optical images of the **T03** sample are reported: before (**Figure 35a**), under (**Figure 35b,** the green light has been filtered out by a long pass optical filter in order to not saturate the camera) and after (**Figure 35c**) the exposition to green light.

Since the pillars contract along their symmetry axis (not appreciable in the optical pictures), and expand in the perpendicular plane, we monitored the diameter ϕ variation before, during and after the light irradiation. In the rest condition (no actuation) the diameter ϕ_a is 20 µm. During the exposition with a green light, the deformation is well detectable and the diameter ϕ_b expands up to 26 µm, with a relative expansion of 23% (**Figure 35b)**. As it can be observed in **Figure 35b**, the contraction/expansion is not homogeneous for all pillars, probably due to a not perfect alignment in each single pillar.

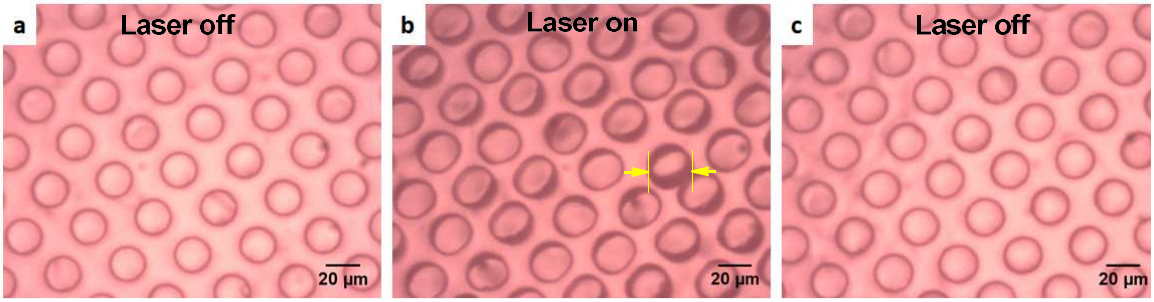

Figure 35 – Optical images of sample T03 a) before **b)** during and **c)** after exposition at green light.

After the irradiation with a green laser light, the complete recovery of the initial size of the structures is achieved as reported in **Figure 35c**.

For the micro patterned surfaces fabricated with **Mix2**, the isomerization of the **5** azo dye requires a 4 minutes exposure (time needed to obtain the maximum deformation) with UV light (385 nm), and 4 minutes exposure to green light (lamp at 505 nm) to relax back to the *trans* state isomer. **Figure 36** shows the experimental deformation. For this sample, a not appreciable deformation of the diameter of the pillars can be observed, the height variation has been evaluated from tilted pillars that probably fall down during the PDMS peeling off. The height before (h_i) and after (h_f) the exposition with UV light were measured (**Figure 36a** and **36b**).

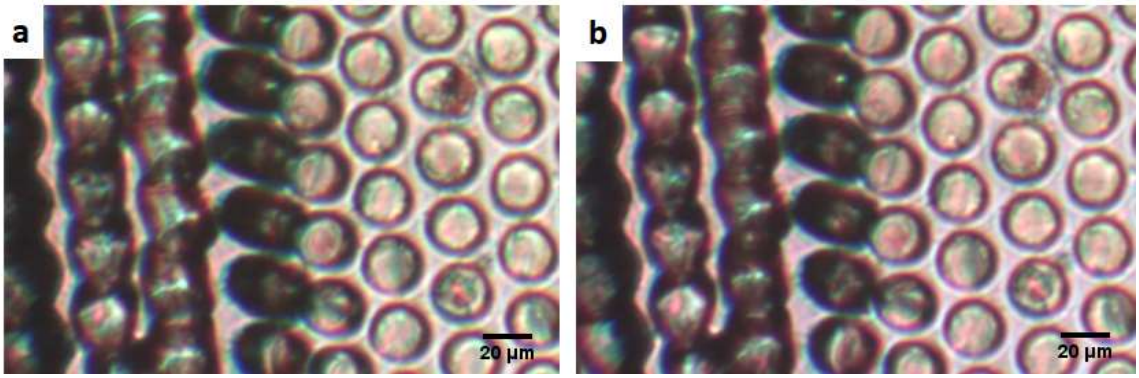

Figure 36 – POM pictures of sample O02 a) before exposition at UV light b) after exposition at UV light

In this case, the contraction of the structure, corresponds to 12%. For **Mix2**, probably due to the higher amount of the crosslinker content in the mixture, the deformation is smaller than in **Mix1**. These deformation values are comparable with the one described in literature, reporting a maximum contraction of acrylate-based LC polymers around the 20% of their original length [109].

2.3.5 Contact angle measurement and evaluation of hydrophobic properties

In order to evaluate the wetting properties of the micro-structured surfaces, we performed different measurement on the static contact angle (CA) analysing both LCE flat films and micro-patterned surfaces.

A water droplet (2 µL) was deposed on the material surface by the computer controlled syringe of a contact angle setup equipped with a CCD camera.

For flat films (**Figure 37a**) the CA is around 70° for films obtained with **Mix1** and 80° for films obtained with **Mix2**, showing a hydrophilic behaviour in both cases (**Figure 37b-d**). When the flat surfaces were tilted the water droplet did not slide. No droplet sliding was observed also in case of turning upside down the patterned surface indicating an high adhesion energy surface and strong water retention on the surfaces.

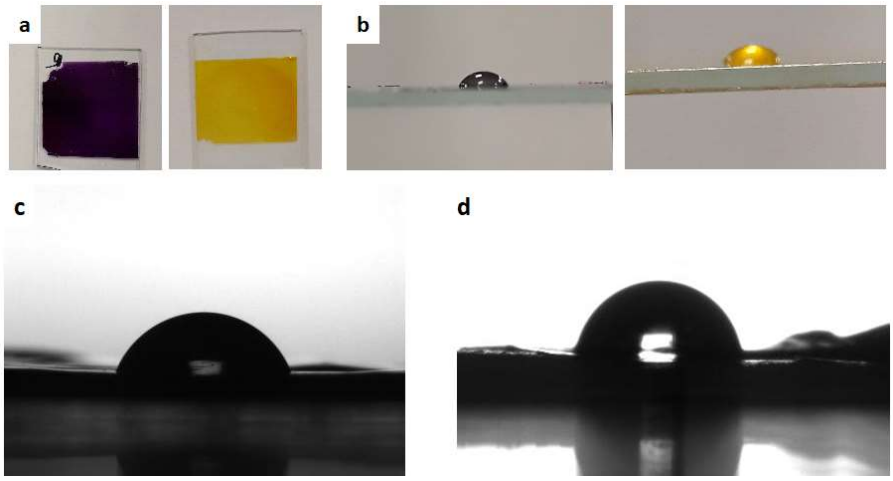

Figure 37 – Evaluation of wettability properties of flat film. a) Pictures of flat film obtained with **Mix1** on the left and **Mix2** on the right (top view) **b**) pictures of flat film (**Mix1** on the left, **Mix2** on the right) with a water droplet on the upper face (side view) **c-d**) Contact Angle measurement on flat film obtained with **Mix1** CA = 70 °C (**c**) and **Mix2** CA = 80 °C (**d**)

Micro-patterning dramatically change the surface properties. [145]. For **Mix1**, it was possible the measure the CA only for **T01** and **T03**, because of the poor homogeneity of the other micropattern geometries.

In **Figure 38** the CA measurements for these samples are reported ($\mathbf{CA_{T01}}$ = 120°, $\mathbf{CA_{T03}}$ = 135°). As expected, the micro-structuring increase the CA value of the surfaces with respect to flat films, confirming an increment of the hydrophobic behaviour for the micro-structured surfaces.

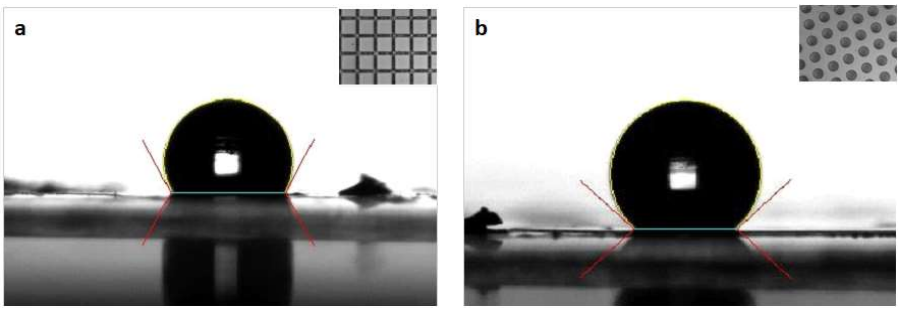

Figure 38 – Contact Angle measurements for micro-structured surface obtained with Mix1 for a) sample **T01** (CA = 120°) and **b**) sample **T03** (CA = 135°)

For the optical mixture, the CA measurement was performed for each geometry of the pillar patterns and reported in **Figure 39.**

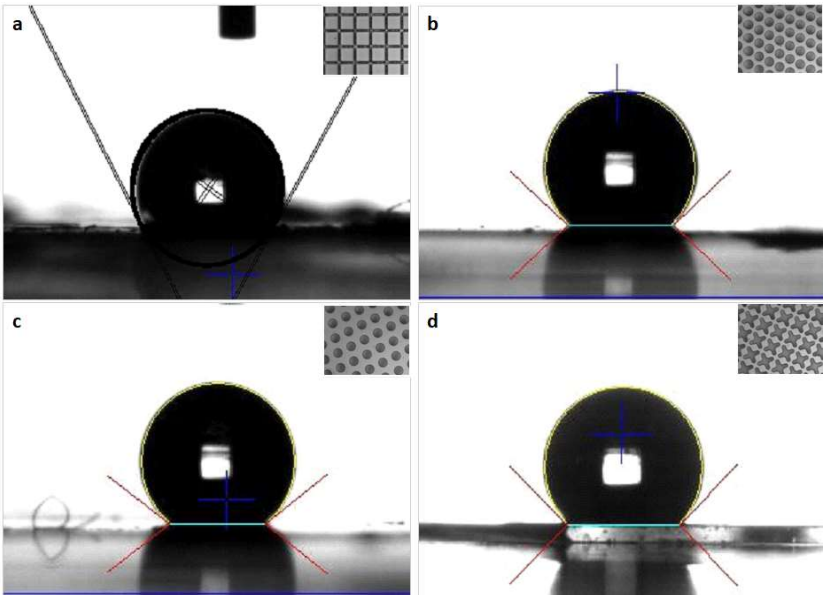

Figure 39 - Contact Angle measurements for micro-structured surface obtained with Mix2 for a) sample **O01** (CA = 120°), **b**) sample **O02** (CA = 135°), **c**) sample **O03** (CA = 136°) and **d**) sample **O04** CA = 120°.

For each sample, CA values greater than 100° are observed, with different values in dependence of the surface morphology. The CA for samples patterned with pillars with circular section ($\mathbf{CA_{O02}}$ = 135°, $\mathbf{CA_{O03}}$ = 136°, **Figure39b** and **c**) are larger than the ones relative to structures with squared ($\mathbf{CA_{O01}}$ = 120°, **Figure39a**) and four-pointed star section ($\mathbf{CA_{O04}}$ = 120°, **Figure39d**).

Contact angle of the different surfaces are collected in **Table 1**.

		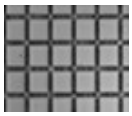	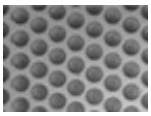	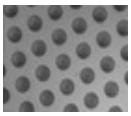	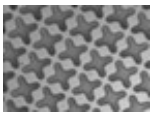
	Flat Film	01	02	03	04
Mix1 CA	70	120	/	135	/
Mix2 CA	80	120	135	136	120

Table 1 – Summarized results for Contact Angle measurements on samples obtained with Mix1 and Mix2.

From this characterization, we can observe that the wettability of the micro-structured surfaces is not dependent on the employed LCE mixture but only on the pillar geometry, with CA reaching the same value for the different mixtures and same morphology (**Table1**).

To further improve the hydrophobicity of the micro-structured surfaces, the samples were coated with a silanizing agent bringing long alkyl chains. As described in Chapter1, the silanization process is a useful tool for the surface modification in term of wettability properties.

The samples were previously exposed to a plasma source that eliminates biological contaminants and, at the same time, favours the hydroxylation (OH groups) of the surface. This step is fundamental to create the sites prone to silanization (**Figure 40b**). The silanization occurs by immersion of the samples in a solution of a silane in a solvent (**Figure 40c**) (octadecyltrichlorosilane (OTS) 5% in weight in hexadecane) and it is completed by a washing bath in hexadecane.

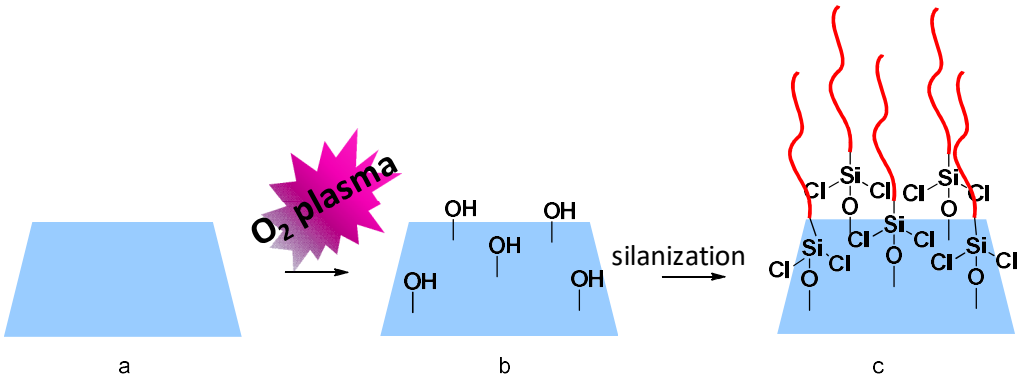

Figure 40 – Schematic process of the functionalization of the glass surface. The glass surface (**a**) is exposed at a O_2 plasma source allowing the exposition of hydroxyl groups on the surface (**b**) obtaining an increase in wettability. The treatment of the activated surface with a silanizing solution allows reaching a hydrophobic surface (**d**) with a consequent decrease of the wettability.

The silanization step allowed to increase both the contact angle and the sliding angle of the droplets (142° Vs 135° for sample **O03**), thus increasing the hydrophobicity of the surface and decreasing the surface energy respectively. Indeed, for the silanized samples, the CA is larger than for the untreated samples (**Figure 41a-b**).

Moreover, a decrease of the surface energy enables the droplet sliding along tilted plane (**Figure 41c-h**).

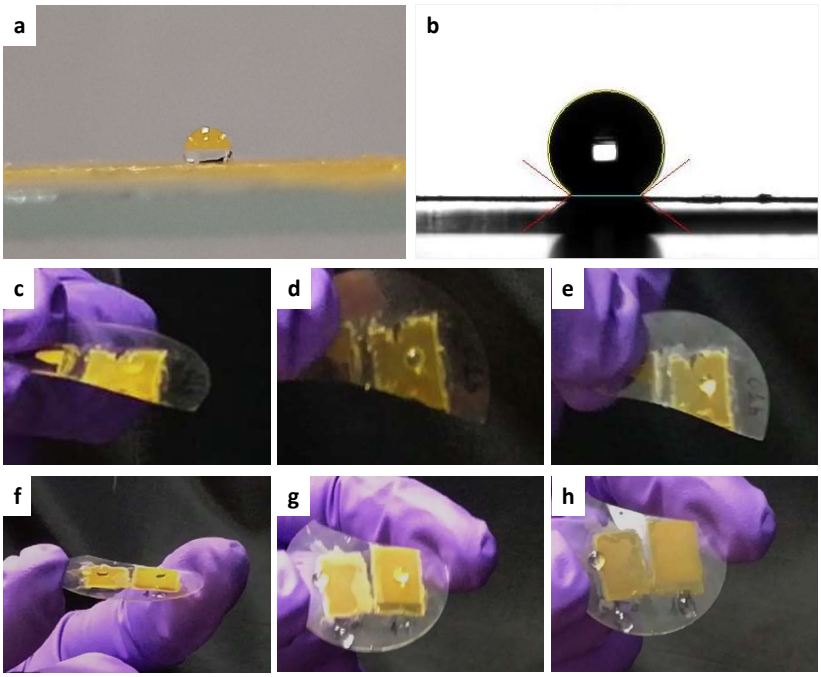

Figure 41 – Images of samples after silanization treatment. The increase of wettability is visible in macroscopic way (**a**) and confirmed by CA measurement of a micro-structured sample (CA = 142°). The silanization treatment not only influences the CA values but allows to decrease the surface energy of the substrate, on which a water droplet rolls off by the untreated tilted surface (**c**-**e**) and slides on it after the treatment (**f**-**h**).

At the end, we evaluated how the dynamic light induced deformation of the micropattern is able to change the hydrophobic properties of the substrate. Such effect was determined by performing contact angle measurements during and after the illumination. Due to the millisecond time response of **Mix1**, the experiment was performed observing the droplet directly in the CCD camera of the contact angle setup. The laser source was assembled in the CA setup, allowing the observation of the CA variation during light exposure.

For these samples, we measured an interesting change in the contact angle (from 135° to 115° for sample **T01** and from 125° to 75° for sample **T03**) as shown in **Figure 42.** Nevertheless, such variation should be associated to viscosity change of the material, caused by temperature increase of the surface induced by the green light absorption. The water droplet does not recover its shape when the laser is turned off.

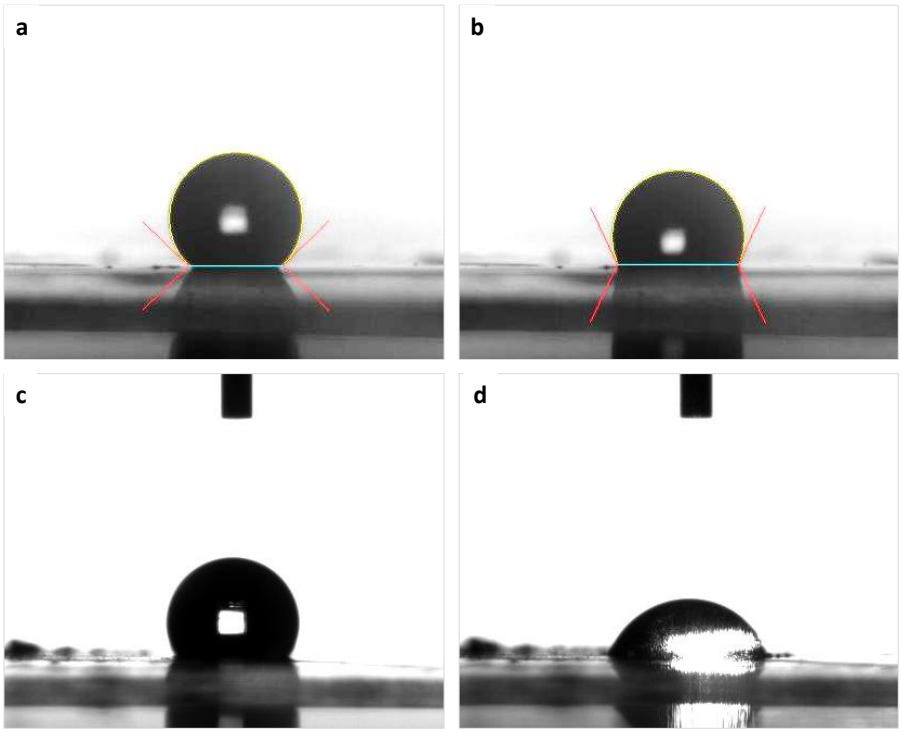

Figure 42 – Dynamic photoresponsive behaviour evaluated with CA measurements. a) CA of sample **T01** before green light exposition (CA = 135°) b) CA of sample **T01** after green light exposition (CA = 115°) **c**) CA of sample **T03** before green light exposition (CA 125°) **d**) CA of sample **T03** after green light exposition (CA = 72°).

These measurements confirm that **Mix1** is not suitable for the preparation of reconfigurable superhydrophobic surfaces due to the possible evaporation of the solvent.

Since **Mix2** requires irradiation by UV light for 4 min to undergo the complete deformation, the measurement of the CA was performed in three steps:

- Measuring the CA of the sample before the UV irradiation
- Exposition of the sample at UV light for 4 minutes
- Measuring the CA after the UV irradiation

In this case, we did not observe a change in CA. The CA measured before (**Figure 43a**) and after the UV light exposition (**Figure 43b**) had the same values. Probably the deformation of the structure was not enough to vary the hydrophobic properties of the surfaces. The same result was also observed after silanization.

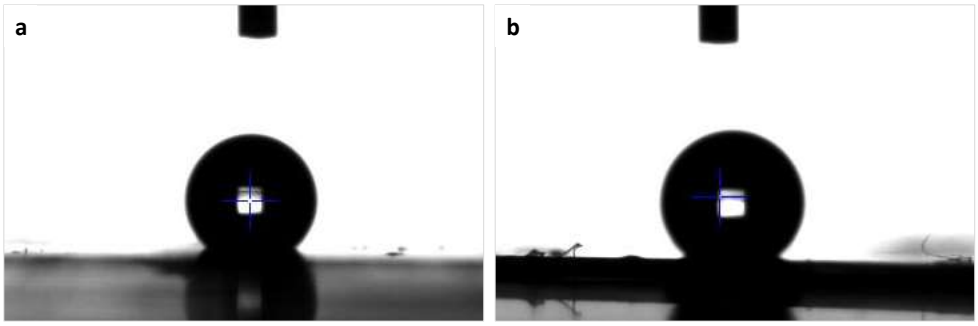

Figure 43 – CA measurements for sample O03 before (a) exposition to UV light (CA = 136°) and after (**b**) exposition to UV light (CA = 135°)

The results described are summarized in the graph below (**Figure 44**).

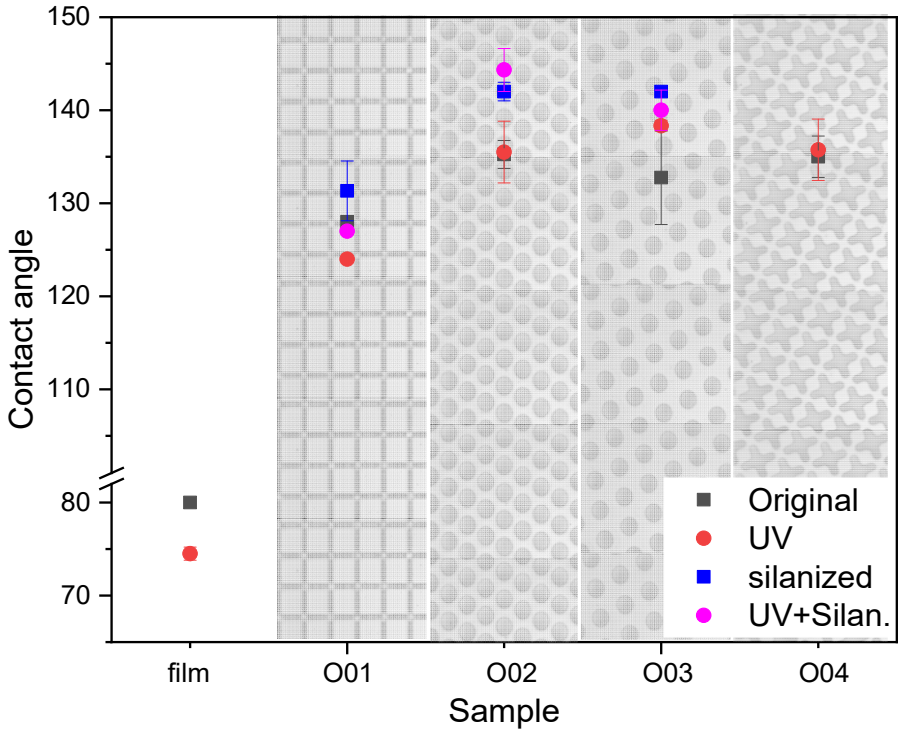

Figure 44 – Summarized results of CA measurements for samples obtained with Mix2.

Although we were able to fabricate micropatterned surfaces with hydrophobic properties, a photo dynamic control of the hydrophobicity of the surfaces was not yet achieved. Further studies will aim to increase the height of the pillars and to improve the LC alignment in order to induce a local deformation that will drive the droplet motion on the surface by light irradiation.

2.4 Micro-structuration of splayed aligned film

Inspired by the work of Zhao and co-workers [146], we engineered a LCE film whose surface was micro patterned to have a superhydrophobic behaviour and a high surface energy. The surface was designed to be able to hold a water micro droplet and our aim was to control its release by light irradiation. The drop-on-demand release represents a powerful way for self-cleaning properties of such structures, and the possibility to be remotely exploited when triggered by light was not yet evaluate.

The sample consists in an array of LCE micropillars on the surface of an LCE film with a splayed alignment (a cell formed by a PVA coated glass, for the planar side, and PI1211 coated glass, for the homeotropic side, was used for such purpose). After infiltration at the isotropic temperature of the mixture, the cell was maintained in the nematic phase temperature (about 55° C) and then polymerized for 10 minutes with a 405 nm lamp (**Figure 45a-b**). The PI coated glass was removed and a LCE droplet was put on the film (**Figure 45c-d**); a piece of PDMS negative mold was casted on it and warmed at 70° C to allow the infiltration of the LCE mixture inside the PDMS holes. In this case, despite the isotropic temperature of the mixture is higher than 70° C, the mixture was infiltrate at 70° C to not compromise the film below, which is thermo-responsive at high temperature. The microstructured layer is then polymerized for 20 minutes with a lamp at 405 nm (**Figure 45 e-f**).

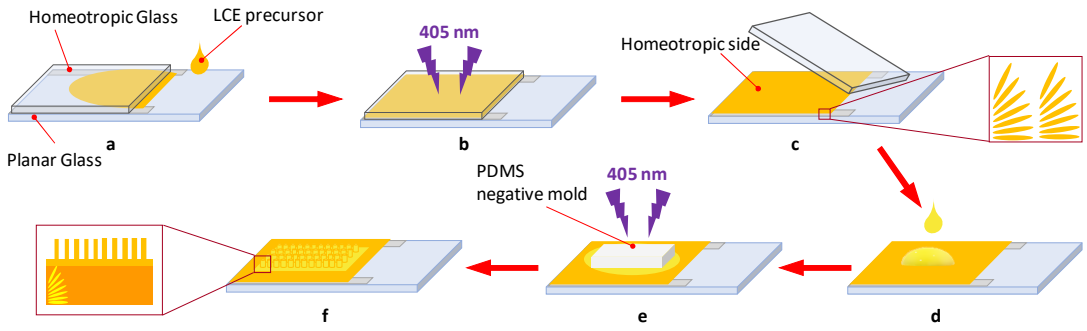

Figure 45 – Schematic procedure for fabrication of splayed-aligned and superficially micro-structured films. LCE precursor is capillary filled into the cell at isotropic temperature of the mixture (**a**). After cooling at nematic temperature and alignment of the mesogens, polymerization is carried out (**b**). The PI coated glass is removed (**c**) and a small amount of LCE mixture is put on the top of the film at 70 °C (**d**). The PDMS mold is laid over the LCE drop and pressed on it. After infiltration, the photopolymerization reaction allows to form the polymeric network and finally, the gentle removal of the PDMS mold allows to obtain micro-pillars on the film (**f**).

A piece of micro-patterned film was cutted and we tested if the bending of the film can modify the hydrophobicity of the surface thus releasing the droplet deposited on the surface.

The structure is thus composed by two layers with two different roles, the splayed film once activated by UV light bends modifying the pillars spacing and the micropillars are responsible for

the superhydrophobic behaviour of the surface. We performed an experiment in which a water droplet was put on the micro-patterned film and then it was irradiated with a lamp at 385 nm to have the *trans-cis* isomerization of the dye that results in the film bending. To come back at the starting condition the film was exposed with a green lamp at 505 nm (**Figure 46a-f**).

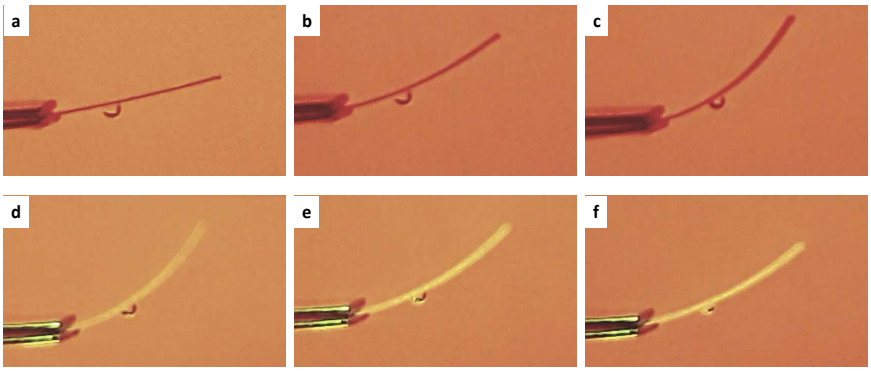

Figure 46 – Photoresponsive behaviour of the splayed-aligned and superficially micro-structured films with a water droplet on it.

Unfortunately, contact angle variation under light exposure is not relevant for tuning the hydrophobic properties of the surface, and further modification in the mixture composition are under evaluation. For example, we are investigating the possibility to vary the type and the % mol/mol of the employed monomers and/or dye in the polymer network in order to reach bigger deformation and the consequent change in wettability of the micro-structured surface.

As described in literature, the photoisomerization behaviour of azobenzene chromophores in crosslinked LC polymer strongly depends on the concentration and location of the azobenzene [147].

With the aim to optimize the micro-patterned surfaces, we explored different mixtures with photoinduced behaviour caused by an isomerization process. The best results were obtained by the mixture (M**ix3**, shown in **Scheme 6**) based on the side-on monomer described by Keller et all [120] combined with the photoactive crosslinker **5.**

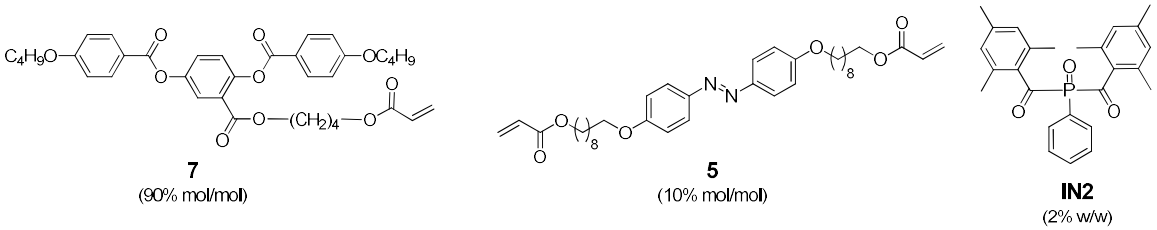

Scheme 6 – Chemical structures and correspondent amount in % used in Mix3

In **Figure 47**, the photoinduced bending of a piece of film is shown. The UV light causes a big bending of the polymer (**Figure 47b**) and the exposition with visible light (505 nm) allows to recovery the initial shape (**Figure 47c**).

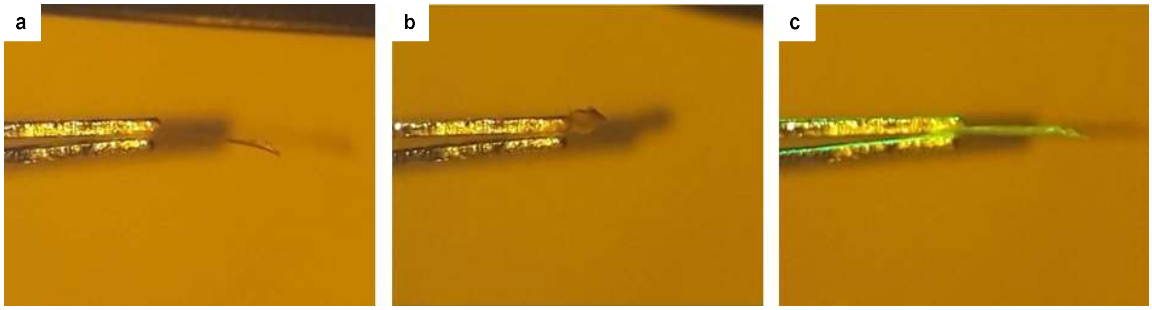

Figure 47 – Photoresponsivity of a splayed-aligned film obtained with Mix3. **a**-**b**) The big bending of the film is caused by the exposition of UV light (382 nm) in 4 minutes **c)** The recovery of the initial state is caused by irradiation with a wavelength in the visible region at 505 nm.

Further characterizations of this mixture and fabrication of micro-structures are currently on going in our laboratories.

Moreover, the use of different monomers or reactions to produce LCE micro-structures could be promising solution to overcome the described drawbacks and limited deformation performed by **Mix2**. In this respect, in Chapter 3 we will show a new synthetic strategy for the fabrication of more responsive polymers.

2.5 Experimental part

General methods. UV-Vis spectra were recorded with a Perkin-Elmer Lambda 950 spectrophotometer. An inverted microscope (Zeiss, Axio Observer A1) with cross polarizers was used to observe the LC phases. Scanning electron microscope (SEM) pictures were collected with a Phenom-World instruments. The samples were mounted on aluminium stubs using conductive carbon tape and coated with a 10 nm thick layer of gold with a sputter coater (Quorum Q150T E). Contact angles measurements were performed using a sessile drop technique. A custom made apparatus was employed for this purpose. Droplets of water with volumes of about 5 µL were deposited on the samples with the rate of 20 mL/hr. At least four images of the liquid droplets deposited on the surfaces were analysed to extract the contact angle at the three phase contact line.

Materials: Commercial reagents were used as received. **1**, **2**, **4**, **5** and **6** were purchased from Synthon Chemicals; **IN1** was purchased from Sigma-Aldrich and **IN2** was purchased from Ciba Speciality Chemicals. **3** and **7** were synthetized in our laboratory and the synthesis are described in other work [109].

Fabrication of micro-patterned surfaces

Micro-patterned substrates were prepared by soft lithographic technique. A master sample was replicated by a PDMS (polydimethylsiloxane) mold that is used as template for the pattern replication.

Master fabrication – Master samples was bought by a company (JD Photo Data) which provided to fabricate silicon master using UV lithography. A UV photomask is made from a transparent material, typically fused silicon, on which a pattern is defined in an absorbing thin film such as chromium. The photomask is brought into proximity or even contact with the resist coated substrate using a dedicated exposure system. The substrate is then exposed through the photomask by a UV light source (Hg-lamp with an i-line notch filter that gives a typical UV source with a wavelength of 365 nm). After exposure the substrate is developed, and the pattern is formed.

Fabrication of PDMS mold – Monomeric PDMS mixture was prepared by mixing the two components of a commercially available PDMS kit (Sylgard 184) in a 10:1 w/w ratio (base and

curing agent) and then casted on the silicon master. After curing at 100° C for 30 minutes, the crosslinked PDMS mold was peeled off by the master.

Fabrication of micro-pillars on the microscope slide – A small amount of a mixture (**Mix1** and **Mix2**) was heated to the isotropic phase (80°C for **Mix1** and 100°C for **Mix2**) on a microscope slide positioned a top a rare earth permanent magnet. The soft mold in PDMS was gently pressed down on the melted sample, which filled the inner structure of the mold. The temperature was then slowly decreased (-1.0 °C/min) to reach the temperature at which the sample is in its nematic phase (45 °C for **Mix1** and 55 °C for **Mix2**). Keeping the temperature constant, the sample was then irradiated through the mold using a UV lamp (ThorLabs M385CP1-C4, λ = 385 nm for **Mix1**, λ = 405 nm for **Mix2**) for 1 hour to promote the photopolymerization-photo-cross-linking of the monomer mixture. After cooling at room temperature, the PDMS mold was peeled off, leaving a thin glassy polymer film covered by a regular array of pillars.

Contact angle measurements – Sessile drop technique was used for contact angle measurements. One water droplet of 2 μL is deposed on the surface of the sample (10 mL/hr) by a contact angle meter equipped with a CCD camera. At least four images of the liquid droplets deposited on the surfaces were analysed to extract the contact angle at the three-phase contact line. Photoresponsive experiments were conducted measuring the CA in real time for **Mix1** and before and after exposition at light for **Mix2**.

Silanization of the micro-structured surfaces – To improve the hydrophobicity of the micro-patterned surfaces a treatment with an alkyl silane was performed. Previously, oxygen plasma activation of the micro-structured surfaces to promote the incorporation of silane molecules was performed. The samples were plasma oxidized in a remote plasma reactor (Harrick PDC 001) for 10 minutes to avoid direct bombardment of the surface. Then, the samples were immersed in a solution of octadecyltrichlorosilane (OTS) 5% wt in hexadecane for 5 minutes and then washed with pure solvent and dried.

Fabrication of micro-pillars on a splayed aligned film

Cell preparation – Glass slides were spin-coated with PI-KEM LTD 6800 Spin coater (series SCS P6808P) instrument. To render planar molecular alignment, an aqueous solution of PVA (Mw 13.000-23.000 87-89% hydrolysed, purchased by Sigma Aldrich) 0.5 % in weight was deposited on the glass and spin coated at 4000 rpm for 2 minutes. The glasses were then dried for 18 h. To

induce homeotropic alignment, glass slides were spin coated with a commercial solution of PI1211 (Nissan Chemical Industries) at 4000 rpm for 1 minutes. The glasses were heated at 180 °C for 30 minutes. PVA coated glasses were rubbed unidirectionally with a cylinder covered by a velvet cloth. To assemble the cell, PVA-coated glass slide was placed with the polymeric layer upwards, and a strip of PET Mylar film (100 µm) was positioned at the extremity of the glass. Then, second glass was place, with the polymer layer facing down, on the Mylar spacer, and the cell was fixed with an adhesive.

Fabrication of splayed LCE films – A mixture of monomer **1** as mono-functional mesogen (51% mol), **4** (18%), **5** (7%), **6** (21%) and **IN4** (3%) as photoinitiator was prepared. The mixture (TNI = 60 °C) was melted to its isotropic phase at 100 °C and injected into the capillary cells. The filled cells were cooled down (~ 1.0 °C/min) to the mixture nematic temperature (~55 °C) followed by photo-initiated cross-linking by 405 nm UV light (ThorLabs M385CP1-C4) for 10 minutes. Then the cells were cleaved while LCE films were still attached to the planar glass slide.

Fabrication of LCE micropillars – a small amount of LCE mixture (with 5% in weight of photoinitiator) was put on the previously prepared splayed LCE attached to glass substrate. A piece of PDMS mold was casted on the LCE mixture and pressed on it and the sample was heated up to 70 °C to melt the LCE precursor and fill the holes. After cooling to nematic temperature (~55 °C) cross-linking took place for 15 minutes. Finally the PDMS mold was peeled off gently and micro-patterned LCE films was detached from glass. Again, to reduce the surface energy and increase the hydrophobicity of the samples, the fabricated LCE micropillars were treated with OTS (5% in weight in hexadecane).

Light induced deformation observation – micro-structured surfaces obtained with **Mix1** (containing the **3** azo dye) were illuminated with a DPSS 532 nm laser through a 20x, 0.25 NA (Plan Achromat, Olympus) objective placed above the sample structure and the movement movies were recorded by a CMOS camera (frame rate 25.8 fps); while micro-structured surfaces obtained with **Mix2** (containing **5** azo dye) were irradiated with a 385 nm (ThorLabs M385L2-C4, I=1.8 $mWcm^{-2}$) and a 505 nm (ThorbLabs M505L3-C1, I=2.7 $mWcm^{-2}$) LED lamps.

Chapter 3 - Liquid Crystalline Elastomers by thiol-yne click reaction: synthesis and properties

3.1 Introduction

The polymerization reaction between thiols and alkynes, also called "thiol-yne coupling" (TYC) has been rediscovered in the last decade as click reaction to be used in materials chemistry, including the preparation of polymers, and more recently for surface modification [148]. First examples of this reaction were reported by Finzi [149] and Kohler [150] in 1930s, but the application of this coupling reaction in material chemistry was very limited until 2009. To the best of our knowledge the only examples were reported by Fairbanks et al. [151] and Chan and co-workers [152].

Like the thiol-ene coupling (TEC), TYC can be considered a click reaction from many point of view: it is orthogonally with other synthetic strategies, it presents mild reaction conditions and an ease workup, it is compatible with water, and presents high reaction rates, good regioselectivity and high yields.

Similarly to the TEC reaction, thiol-yne reactions are induced by photo-irradiation via a radical initiator. However, differently from TEC, they consist of a two-step reaction in which individual thiols are added sequentially (**Scheme 7**) [153].

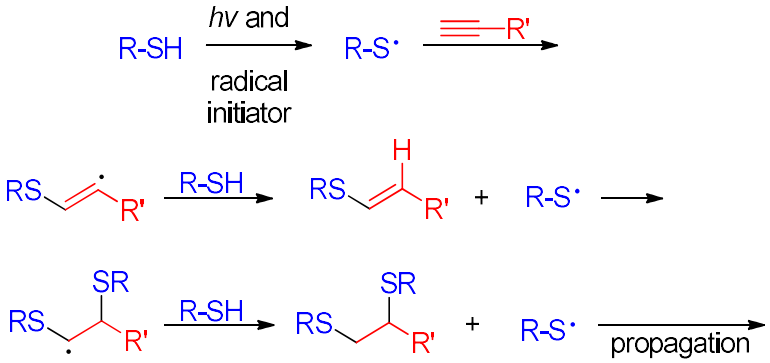

Scheme 7 – Mechanism of initiation and propagation of thiol-yne photopolymerization performed under radical conditions

Both thiol-ene and thiol-yne photopolymerizations of multifunctional monomers proceed via a radical-mediated step-growth mechanism, involving alternation between propagation and chain transfer reactions. The step-growth mechanism leads to lower shrinkage stress and homogeneous networks containing a relatively low amount of unreacted, leachable compounds [154], [155]. Moreover, the ability of a peroxy radical to extract a hydrogen from a thiol imparts these reactions with exceptional resistance to oxygen inhibition [156], [157], overcoming the typical drawback of the normal acrylate polymerization to be vulnerable to inhibition by molecular oxygen [158].

The addition of a thiol to a terminal carbon-carbon triple bond can lead to the formation of six possible products (**Scheme 8**), each of which can be obtained essentially quantitatively under specific experimental conditions; the formation of the monoaddition products **A**-**C** and the double addition dithiolacetal derivatives **D** and **E**, can be obtained employing appropriate catalysts [159].

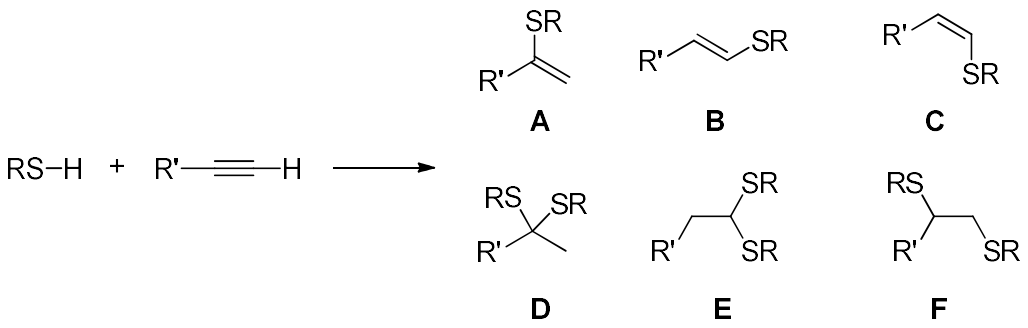

Scheme 8 – Possible addition products for the mono- and bis-hydrothiolation of a terminal alkyne bond

The 1,2-addition product (**F**, **Scheme 8**) is readily obtained under radical-mediated conditions with two or more equivalents of thiol. The mechanism of addition to give the general product **F** is formally represented by the sequential thiol-ene and thiol-yne reactions (**Scheme 9**).

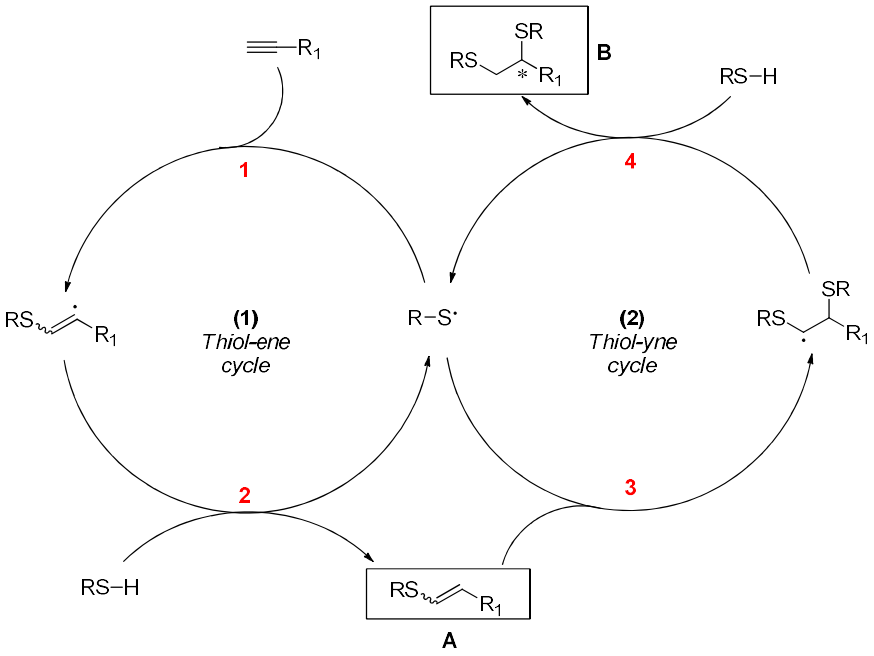

Scheme 9 –Sequential addition and hydrogen abstraction steps of 1) primary alkyne and the 2) subsequent vinyl sulphide during a thiol-yne polymerization

Thiyl radical, R-S•, is firstly generated by the use of a photoinitiator, and, in the presence of an alkyne, readily react with it resulting in the intermediate vinylthioether radical (step 1). Step 2 involves a chain transfer reaction between the intermediate vinyl-based radical with an additional thiol to give the vinylthioether intermediate, **A**. Importantly, **A** is also highly reactive towards thiyl radical and will react with R-S•, step 3, to give an intermediate carbon-centred radical that undergoes a second chain transfer reaction, step 4, yielding the target 1,2-bisaddition dithioether product, **B** [151].

Polymers obtained with the thiol-yne reaction are characterized by low cross-link density which can be tuned by changing the stoichiometric ratio between the thiol, the terminal alkyne and the bifunctional alkyne (used as cross-linker). Thus, they are very different from networks formed by chain-growth polymerizations of multifunctional (meth)acrylates, that presents high cross-link density resulting in many mechanical and thermal properties, including high strength and high glass transition temperature (T_g) [160].

The possibility to use this reaction to produce LCEs was already explored by our research group. In a preliminary work, we demonstrated LCE with a mixed main-chain/side chain architecture [117] able to undergo bigger deformation than previously reported side-chain LCEs prepared by acrylate polymerization [161]. Moreover, Direct Laser Writing (DLW) technique was employed for the fabrication of biocompatible 2D patterned structures having different geometries exploring thiol-yne reaction [162], and preliminary biological tests on these micropatterned surfaces were performed to evaluate their biocompatibility.
In this Chapter we describe the synthesis of a small library of thiols and alkynes and the study of their LC properties (DSC measurements and POM observation). Later on, such molecules are employed to prepare polymeric films, those properties are evaluated both mechanically (DMA measurements) and thermo-responsively. Finally, a simple example of application of these polymers in soft robotic field is shown, with the fabrication of a shape-change thermo-responsive structure.

3.2 Results and discussion

3.2.1 Design of the new mesogens

In order to obtain LCE having a mixed main-chain/side-chain architecture (**Scheme 10**) and to study the relationship between the polymer architecture and the final material properties, we designed a small library of monomers (thiols and alkynes, **Scheme 11** and **12**) functionalized respectively with two thiol groups at the end of the flexible spacer or bearing an alkyne group. To allow the cross-linking of the network, we used the cross-linker **CL1** (**Scheme 12**), bearing two alkyne functionalities according to previous study in our group [117].

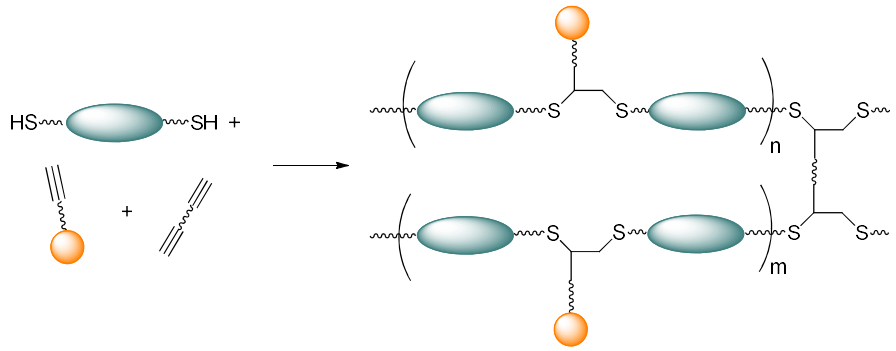

Scheme 10 – Structure of LCEs based on thiol-yne click chemistry

Regarding the mesogenic dithiols, we designed molecules containing a different number of aromatic rings in the core, parameter that is known to influences the mesomorphic properties of the molecules [163], [164]. In particular, we choose to prepare dithiols with three (**Thio1**) or two aromatic rings (**Thio2**) in the core (**Scheme 11**). Such molecules are responsible of the main chain architecture.

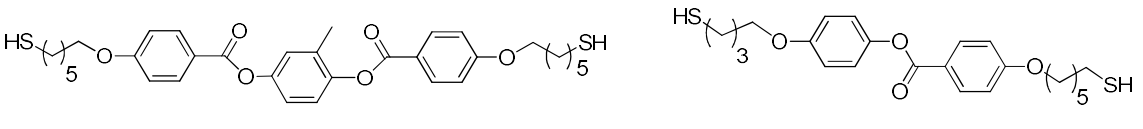

Thio1 Thio2

Scheme 11 – Chemical structures of thiols used in this thesis work

On the other hand, the side-chain component, since we are aiming at a mixed main-chain/side chain architectures, is guaranteed by the other mesogens containing the alkyne moiety. Therefore, we synthetized different mesogenic alkynes (**Scheme 12**) with molecular structure chosen on the basis of many reports on acrylate-based monomers [106], [165]. We chose to prepare a "side-on" monomer (**Alk1)**, able to maximise the coupling with the polymer backbone [166], and a series of "end-on" monomers having different terminal groups (**Alk2**, **Alk3, Alk5**). Interestingly, we obtained an additional mesogen from the synthesis of the others. **Alk4** is in fact one of the intermediates obtained from the synthesis of the other compounds, and it can be

considered a mesogen thanks to the ability of benzoic acid derivatives to form liquid crystalline phases by hydrogen bonding and dimerization (**Figure 48)** [167].

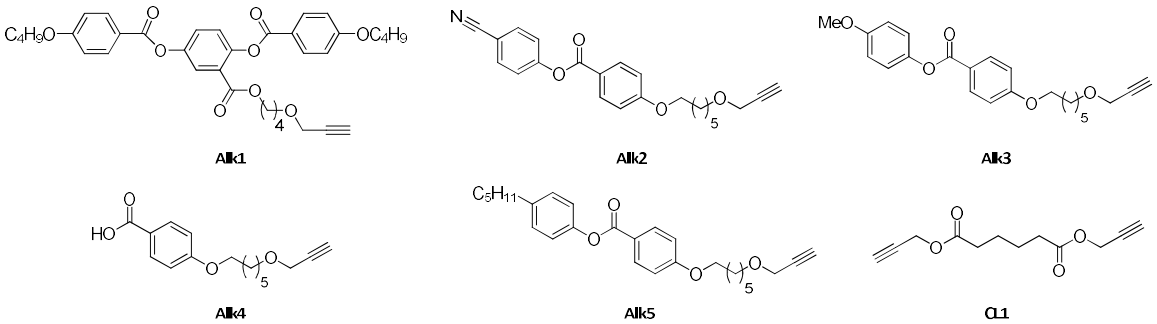

Scheme 12 – Chemical structures of alkynes and cross-linker used in this work

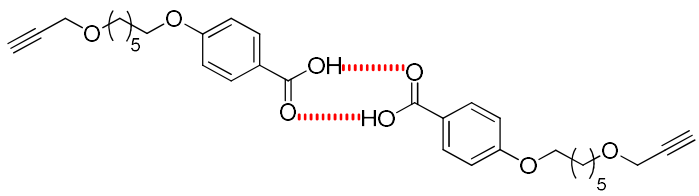

Figure 48 – Hydrogen bond between two molecules of Alk4

4.2.2 Synthesis of monomers

Monomer **Thio1** was synthetized following the synthetic route shown in **Scheme 13**.

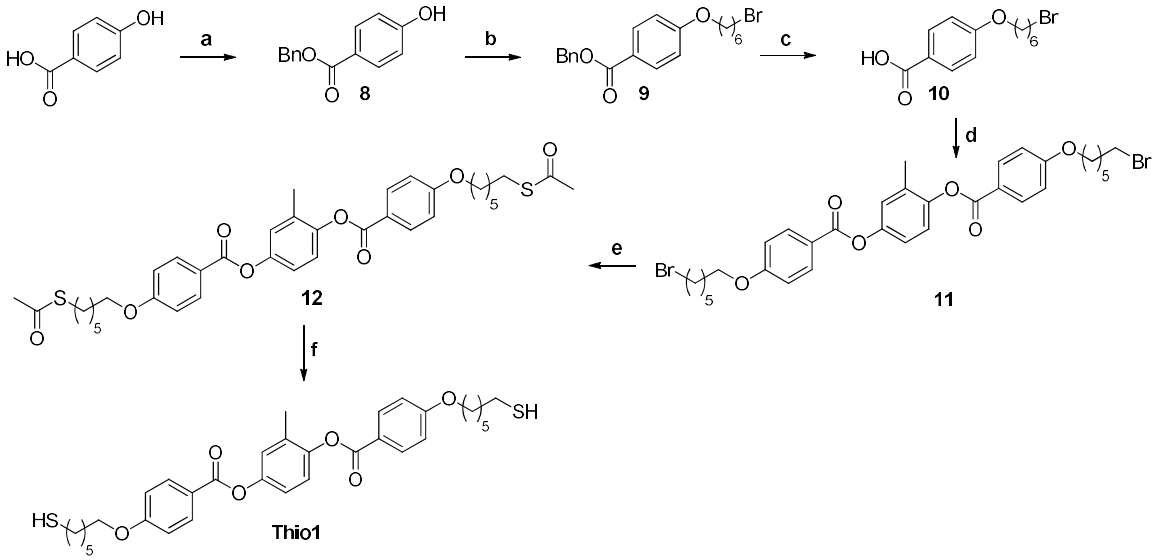

Scheme 13 – Synthetic route for synthesis of Thio1. Reagents and conditions: a) 4-hydroxybenzoic acid, $NaHCO_3$, DMF, benzyl bromide, 90 °C, 18 h, 95%; b) 1,6-dibromohexane, K_2CO_3, acetone, reflux, 18 h, 68%; c) cyclohexene:ethanol 1:1, $Pd(OH)_2$ 10% in weight, reflux, 18 h, 76%; d) DMF dry, oxalyl chloride, CH_2Cl_2, room temperature, 4 h, then methylhydroquinone, TEA dry, THF dry, room temperature, 18 h, 62%; e) KSAc, DMF, room temperature, 4 h, 94%; f) $NaBH_4$, THF:H_2O 1:5, room temperature, 24 h, 68%.

The first step is the protection of the carboxylic acid moiety, needed to introduce selectively an alkyl chain on the hydroxyl group. Benzyl 4-hydroxybenzoate (**8**) was subjected to a Williamson

reaction with 1,6-dibromohexane to give the monoalkylated product **9**. This step involves the reaction of an alkoxide ion, often generated in situ by a carbonate base or potassium hydroxide, with an alkyl halide via an S_N2 substitution. A wide range of solvents can be used, but protic and apolar ones tend to strongly slow the reaction rate while acetonitrile and DMF are commonly used. If less reactive alkyl chlorides are used, the reaction rate can be improved by the addition of a catalytic amount of an iodide salt, which undergoes halide exchange with the chloride to yield a more reactive iodide derivative. To minimize the amount of the disubstituted product, four equivalents of 1,6-dibromohexane were used favoring the statistically favorite monosubstituted product. In these conditions, it is possible obtain the desired product with a yield of 68%. The benzyl ester **9** was hydrogenated to remove the benzyl group with $Pd(OH)_2/C$ as catalyst in a mixture of cyclohexene and ethanol at reflux affording **10** in 76% yield. The conditions resulted a safer alternative to the common procedure based on the use of the more dangerous molecular H_2. In such reaction, the catalyst acts as a transfer hydrogenation medium from a donor molecule (in our case the cyclohexene) to the reactant. The stability of the oxidized donor molecule (1,3-cyclohexadiene) drives the reaction.

The acid **10** was esterified with methyl hydroquinone in order to obtain **11**. The reaction is not trivial and different conditions were attempted in order to gain the desired product with high yields. First, we used a Steglich procedure with *N*,*N*'-dicyclohexylcarbodiimide (DCC) as coupling agent [168]. This esterification method is a variation used to obtain a peptide bond. In general, the reaction using a carbodiimide proceeds via formation of a highly reactive *O*-acylisourea (**Scheme 14**), which is attacked by the hydroxyl function of the alcohol, forming the ester bond.

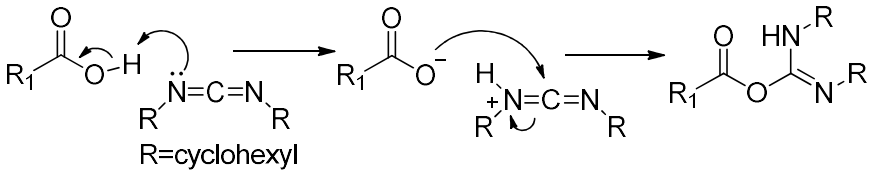

Scheme 14 – Mechanism of formation of *O*-acylisourea

In our case, using DCC, a large amount of byproducts was formed, obtaining the desired product in 34% yield. We thus moved our attention on different coupling reagents, and we tested the 1-ethyl-3-(3-dimethylaminopropyl)carbodiimide (EDC) with DMAP obtaining the product in 6% yields, and its hydrochloride form EDC·HCl achieving **11** in 40% yield [169].

A more efficient strategy resulted in the interconversion of **10** to the corresponding acyl chloride by the use of oxalyl chloride and a catalytic amount of DMF. The subsequently coupling with methylhydroquinone allowed to obtain the desired product in 62% yield.

Obtaining thiols from the corresponding bromide derivate is not trivial with our molecules, because of the presence of the ester groups inside the molecules. Generally, the synthesis of

thiols from bromide is performed passing through a salt derivative, for examples using Bunte salts ($RSSO_2Na$) [165], or a thiouronium salt [171], followed by its hydrolysis in hard acid or basic conditions. An alternative strategy involves the use of tetrabutylammonium trimethylsilylthiolate ($Me_3SiS^-Bu_4N^+$) generated in situ by adding a solution of tetrabutylammonium fluoride (TBAF) to hexamethyldisilathiane in THF, which reacts rapidly with the bromide to generate the thiol [172]. This last strategy is usually very simple and effective, but on our molecules, we demonstrated it inefficient because it resulted in a poor control of the reaction.

In our case the strategy involving the formation of the isothiouronium salt was not effective due to the hard-basic conditions required for the hydrolysis, thus we decided to hydrolyze the corresponding thioacetate derivative (**12**). Intermediate **12** was obtained by treatment of the bromide derivative **11** with potassium thioacetate, obtaining the desired product in high yields (94%); also, in this case, different procedures were tried to obtain the dithiol derivative (**Thio1**) (**Scheme 15**) (**Table 2**).

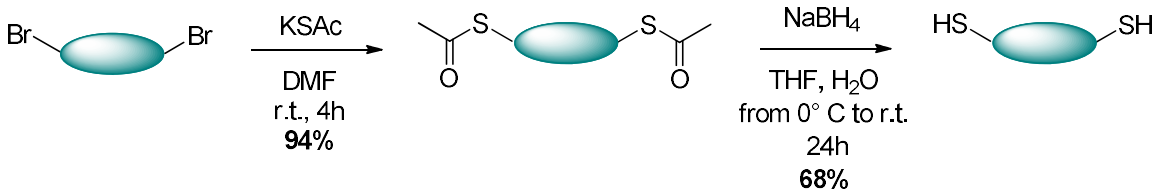

Scheme 15 – Scheme of the reaction to obtain thiol derivative starting from bromide derivative using KSAc in DMF in step1 and subsequently hydrolysis using $NaBH_4$ in water (step2).

Reagent (eq)	Solvent	Conditions	Result	Comments
NaSMe (4)	Methanol	r.t, N_2, 2 h	✗	Hydrolysis of the ester bond
NaSMe	DMF	r.t., N_2, 18 h	✗	No reaction
K_2CO_3 (4)	Methanol	r.t., N_2, 2 h	✗	Hydrolysis of the ester bond
K_2CO_3 (4)	DMF	r.t., N_2, 18 h	✗	No reaction
K_2CO_3 (4)	CH_2Cl_2	r.t., N_2	✗	Hydrolysis of the ester bond
$NaBH_4$ (5)	THF/H_2O	r.t., 48 h	✗	Reaction not complete
$NaBH_4$ (10)	THF/H_2O	r.t., 48 h	✗	Reaction not complete
$NaBH_4$ (30)	THF/H_2O	r.t., 24 h	✓	

Table 2 – Reaction conditions used to obtain thiol derivative passing by the hydrolysis of thioacetate derivative

All the attempts are summarized in **Table 2**. The hydrolysis promoted by NaSMe [173], both in methanol and DMF, has led to the hydrolysis of the ester bond, such as using K_2CO_3 in different

solvents [174], while using K_2CO_3 in DMF, did not led to any reaction. Finally, the use of sodium borohydride in high excess (30 equivalents) in a mixture of water and THF [175] for 24 hours gave product **Thio1** in 68% yield.

Synthesis of the monomer **Thio2** followed a similar synthetic approach as reported in **Scheme 16**. Molecule **13** was obtained in 65% yield by a Williamson reaction between 4-(benzyloxy)phenol and 1,4-dibromobutane. Similarly to for **10**, **13** was hydrogenated to remove the benzyl group with $Pd(OH)_2/C$ as catalyst affording **14** in quantitative yield. The esterification reaction between **14** and **10**, provided the dibromide derivative (**15**) in 80% yield using DCC and DMAP.

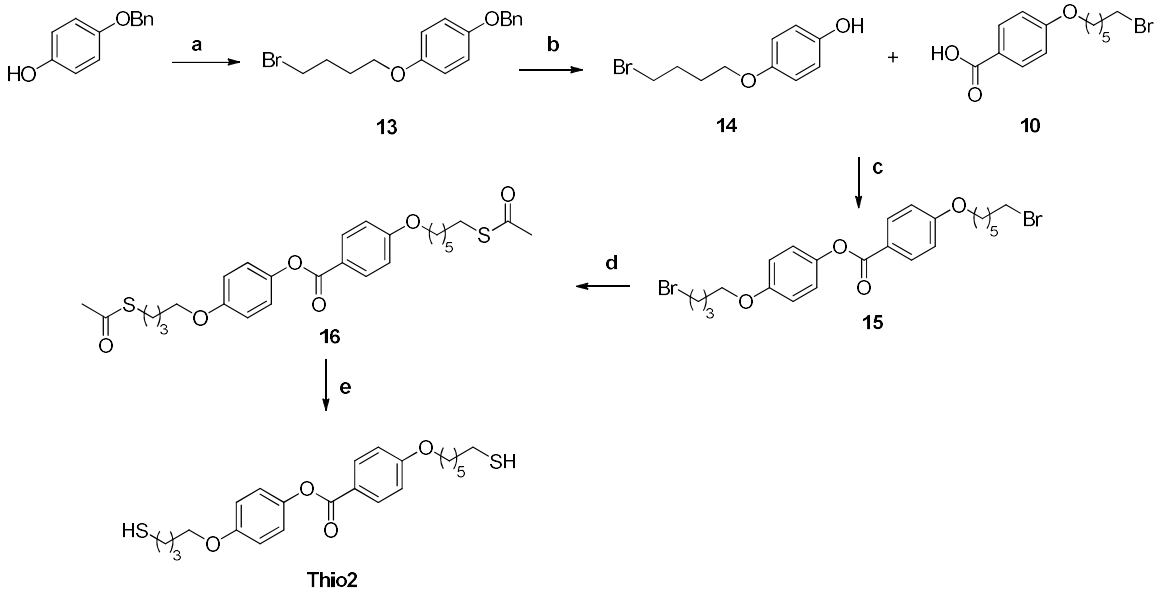

Scheme 16 – Synthetic route to obtain Thio2. Reagents and conditions: a) 1,4-dibromobutane, K_2CO_3, acetone, reflux, 18 h, 65%; b) cyclohexene:ethanol 1:1, $Pd(OH)_2$ 10% in weight, reflux, 18 h, 100%; CH_2Cl_2 dry, DCC, DMAP, room temperature, 18 h, 80%; KSAc, DMF, room temperature, 2.5 h, 88%; $NaBH_4$, THF:H_2O 1:5, room temperature, 24 h, 67%.

As for **11**, bromide derivative **15** was treated with potassium thioacetate to obtain **16** in 88% yield and, finally, hydrolysis of the dithioacetate derivative **16,** in the same conditions reported for **Thio1**, afforded **Thio2** in 67% yield. In this case the purification of the monomer, after the reaction with $NaBH_4$, was performed through FCC on alumina to better separate the desired product to a little amount of starting material present in the crude mixture.

As regards the preparation of alkynes, we started with the synthesis of the **Alk1**, already used in a previous work [117]. It was prepared by esterification between the mesogenic unit **19** and **20** (**Scheme 17**). Synthesis of **19** was performed following a procedure already described in literature [106].

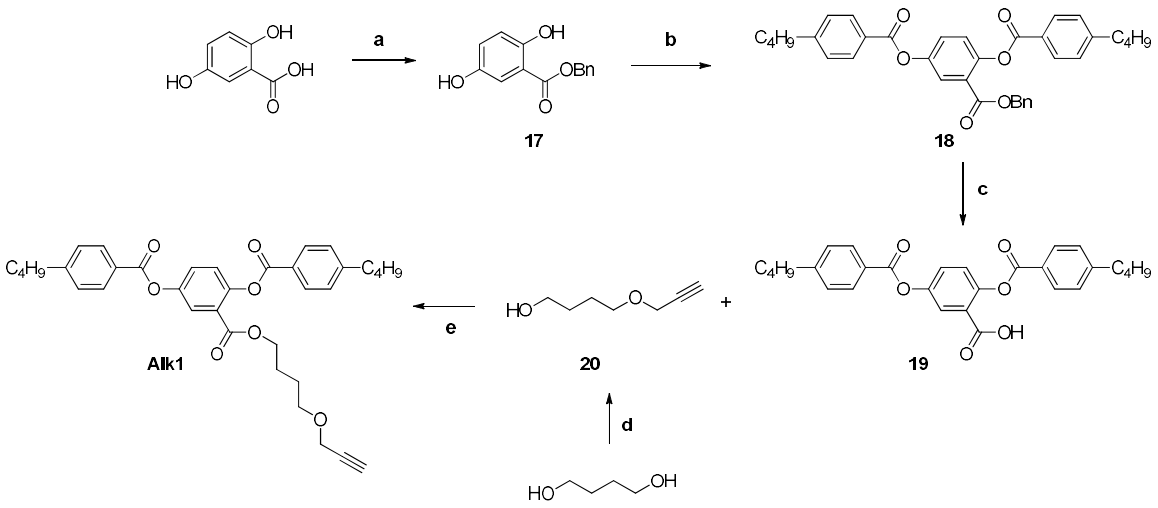

Scheme 17 – Synthetic route to obtain Alk1. Reagents and conditions: a) $NaHCO_3$, DMF, 70 °C, 1 h, then benzyl bromide, 70 °C, 4 h, 90%; b) 4-butyloxybenzoic acid, DCC, DMAP, CH_2Cl_2 dry, room temperature, 12 h, 81%; c) Pd/C 10% in weight, H_2, CH_2C_2, room temperature, 48 h, 89%; d) NaH, DMF, 0 °C, 30 minutes, then propargyl bromide (80% w/w in toluene), DMF, room temperature, 18 h, 71%; e) DCC, DMAP, CH_2Cl_2, 18 h, 75%.

The carboxylic group of the 2,5-dihydroxybenzoic acid was protected as benzylic ester with $NaHCO_3$ in DMF at 70 °C: using the benzyl bromide in stoichiometric amount, only the carboxylate group reacts leading to the formation of the desired product. Then the phenol groups of **17** were esterified with 4-butyloxybenzoic acid affording **18**: such protection strategy was required to avoid the intramolecular coupling of the 2,5-dihydroxybenzoic acid and the formation of other side products. The benzyl group was then removed with a hydrogenolysis to give **19** in 85% yield over three steps. **20** was prepared by monopropargylation of the 1,4 butanediol. The reaction started with deprotonation of the hydroxyl groups of 1,4 butanediol by dropwise addition of a solution of NaH, then it proceeds with the addition of propargyl bromide. Four equivalents of 1,4 butanediol with respect to the alkyne were required to avoid the formation of the disubstituted product affording **20** in 71% yield.

The propargylation of 6-chlorohexan-1-ol, to obtain **21** in 69% yield, was performed in the same way described for **20** (**Scheme 18**).

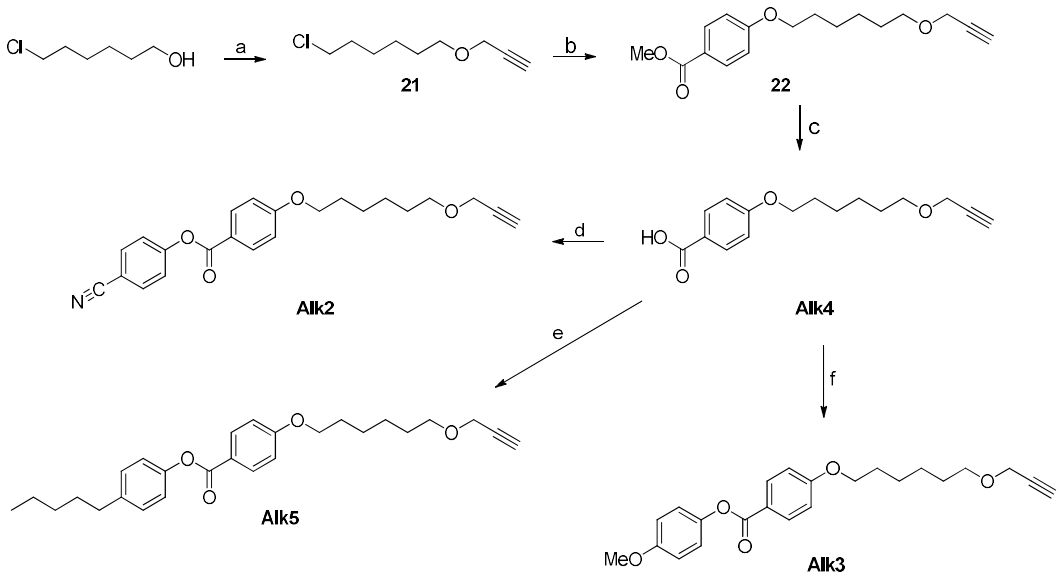

Scheme 18 – Synthetic route to obtain Alk2, Alk3, Alk4 and Alk5. Reagents and conditions: a) NaH, DMF, 0 °C, 30 minutes, then propargyl bromide, DMF, room temperature, 18 h, 71%; b) methyl 4-hydroxybenzoate, K_2CO_3, NaI, DMF, 85 °C, 18 h, 100%; KOH, methanol, 50 °C, 18 h, 78%; d) DCC, DMAP, CH_2Cl_2, room temperature, 10 minutes, then 4-hydroxybenzonitrile, room temperature, 18 h, 54%; e) DCC, DMAP, CH_2Cl_2, room temperature, 10 minutes, then 4-pentylphenol, room temperature, 18 h, 69%; f) DCC, DMAP, CH_2Cl_2, room temperature, 10 minutes, then 4-methoxyphenol, room temperature, 18 h, 63%.

Then, **21** was subjected to a Williamson reaction using DMF as solvent and, in this case, to improve the reaction rate a catalytic amount of sodium iodide was added, obtaining **22** in high yield. The hydrolysis of **22** afforded **Alk4** in 78% yield. **Alk2**, **Alk3** and **Alk5** were prepared in a single synthetic procedure from the common intermediate **Alk4** by esterification with different para-substituted hydroquinones as reported in **Scheme 18** mediated by DCC and DMAP in 54, 69 and 63 % yield, respectively.

3.2.3 Mesomorphic properties of molecules

Mesomorphic behaviour of molecules was characterized by DSC and POM.

The transition temperatures for the mesogenic dithiols are summarized in **Table 3**.

Monomer	Phase transition temperatures [°C][a]	
Thio1	h: Cr 81 N 163 (2.1) I	c: I 161 (2.1) N 45 Cr
Thio2	h: Cr 62 N 77 (0.56) I	c: I 76 (0.57) N 50 LC 17.3 Cr

Table 3 – Thermal properties of monomers obtained during the second heating (h)-cooling (c) cycle of DSC experiments. [a]Determined from the onset of the transition peak. In bracket is reported the enthalpy of the transition (kJ/mol) determined from the integration of peak.

In **Figure 49** the DSC traces and the POM images of **Thio1** (**Figure 49a** and **b**) and **Thio2** (**Figure 49c** and **d**) are shown.

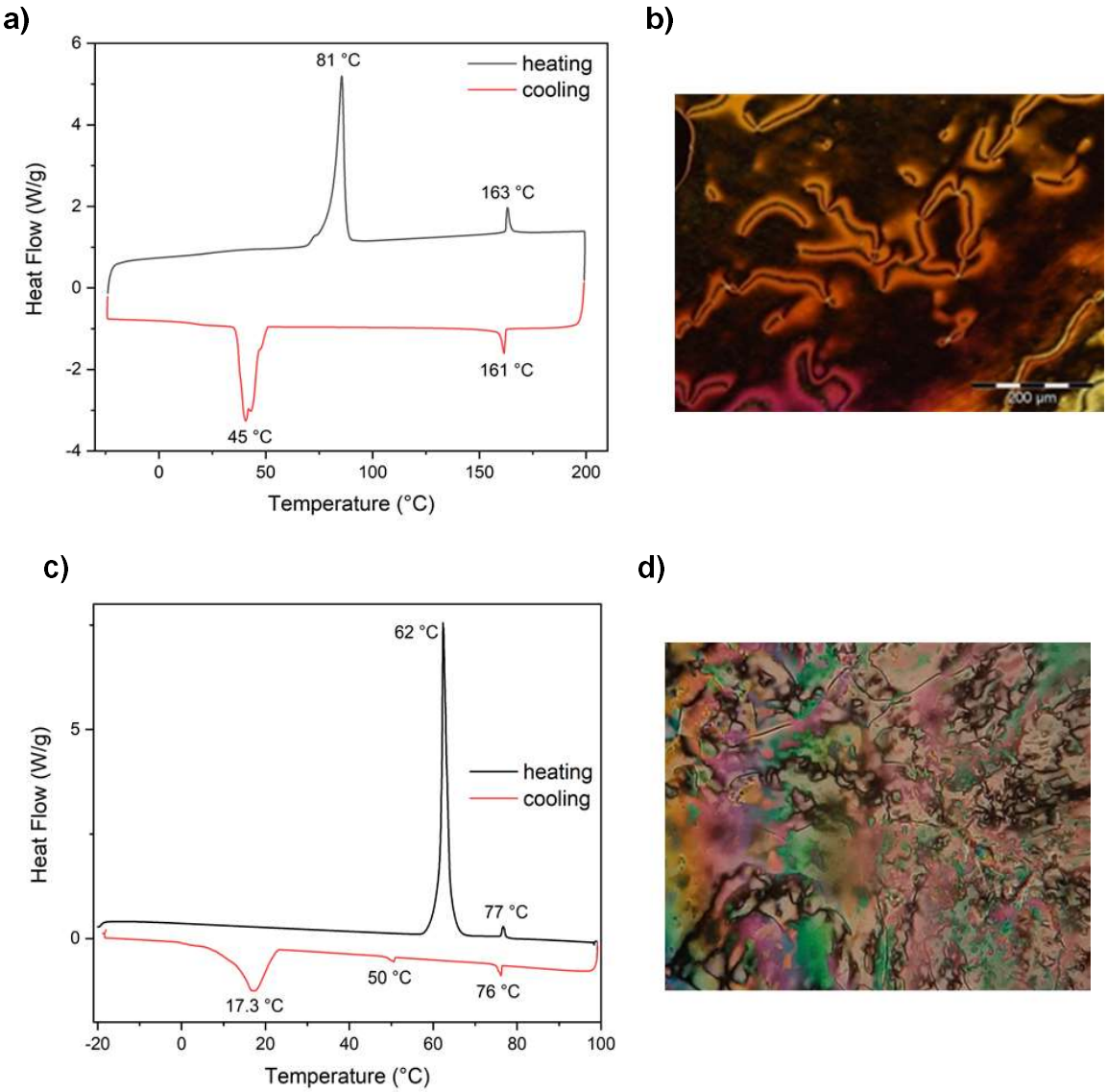

Figure 49 a) DSC traces (10 °C/min) corresponding to the first cycle of heating and sixth cycle of cooling of mesogens **Thio1 b)** POM image of **Thio1** at 90 °C **c)** DSC traces (10 °C/min) corresponding to the first cycle of heating and sixth cycle of cooling of mesogens **Thio2 d)** POM image of **Thio2** at 67 °C.

Both **Thio1** and **Thio2** present an enantiotropic nematic phase. **Thio1** shows on heating a peak around 85.5° C attributable at the melting temperature and the peak of the LC phase at 163.2° C; on cooling the same peak at 162° C was observed and the nematic phase nature was confirmed by POM picture, showing the *Schlieren* texture at 130° C (**Figure 49b**). **Thio2** on heating presents a melting point around 62.3° C and a lower transition temperature than **Thio1**, around 76.3° C. On cooling, the DSC shows a second exothermic peak at 50° C attributable to another LC phase (**Figure 49c** and **d**).

Transition temperatures related to alkynes are summarized in **Table 4**.

Monomer	Phase transition temperatures [°C][a]		T_g [°C][b]
Alk1[d]	h: Cr 71 N 88 (1.01) I	c: I 86 (1.08) N[c]	-20.4
Alk2	-	-	-
Alk3[e]	h: Cr 67 I	c: I 48 Cr	-
Alk4[e]	h: Cr 102 N 110 (1.82) I	c: I 110 (2.62) N 88.6 (1.86) Sm 48.2 Cr	-
Alk5	-	-	

Table 4 – Thermal properties of alkynes. [a]Determined from the onset of the transition peak. In bracket is reported the enthalpy of the transition (kJ/mol) determined from the integration of peak. [b]Determined from the midpoint of the baseline jump. [c]Crystallization was not observe on cooling down until -50 °C. [d]Obtained during the second heating (h) -cooling (c) cycle. [e]Obtained during the third heating (h) and second cooling (c) cycle of DSC experiments.

Alk1 presents an enantiotropic nematic phase. On heating the LC phase is observed at 88° C (**Figure 50a**) and the crystallization in not observed during the cooling stage. As confirmed by POM, the liquid crystal phase has a nematic nature (**Figure 50b**).

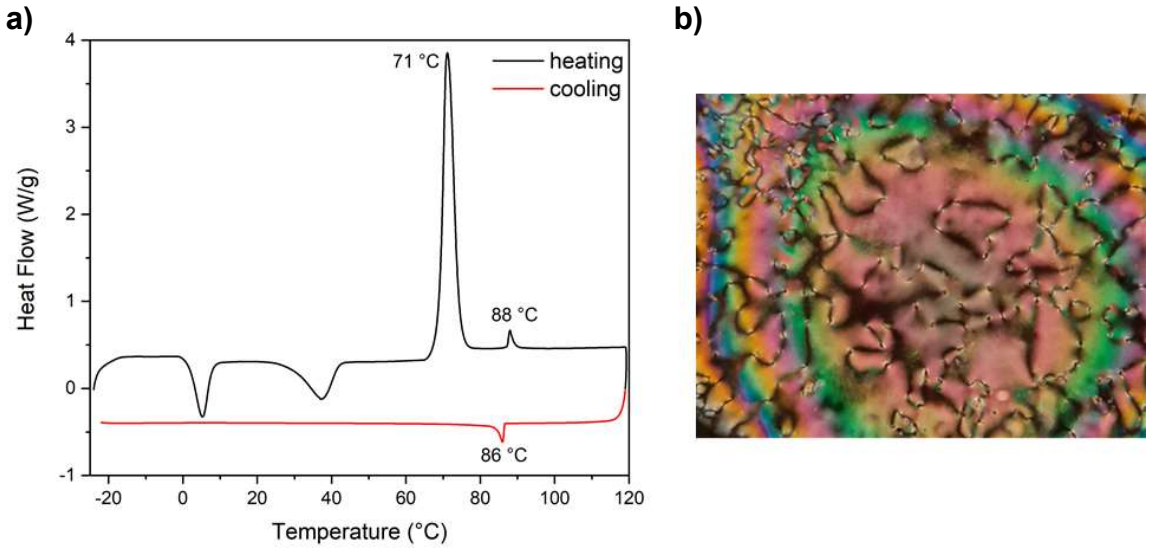

Figure 50 – a) DSC traces (10 °C/min) corresponding to the second cycle of heating and cooling of mesogens Alk1 **b)** POM image of **Alk1** at 85 °C.

Mesomorphic properties of **Alk2** were not studied by DSC analysis, because when mixed with other components, smectic phases are obtained that, for their nature are complicate to be aligned and are not useful for our purpose. **Alk4** shows, during heating, high melting temperature (around 105° C) and one enantiotropic pick (around 110.2° C) corresponding at the nematic phase, as confirmed by POM (**Figure 51b**). During cooling we observed the same pick correspondent to the

nematic phase around 110° and an additional one correspondent to a monotropic phase at 88.6° C, which can be associated to a smectic phase, most likely a SmA (**Figure 51c**).

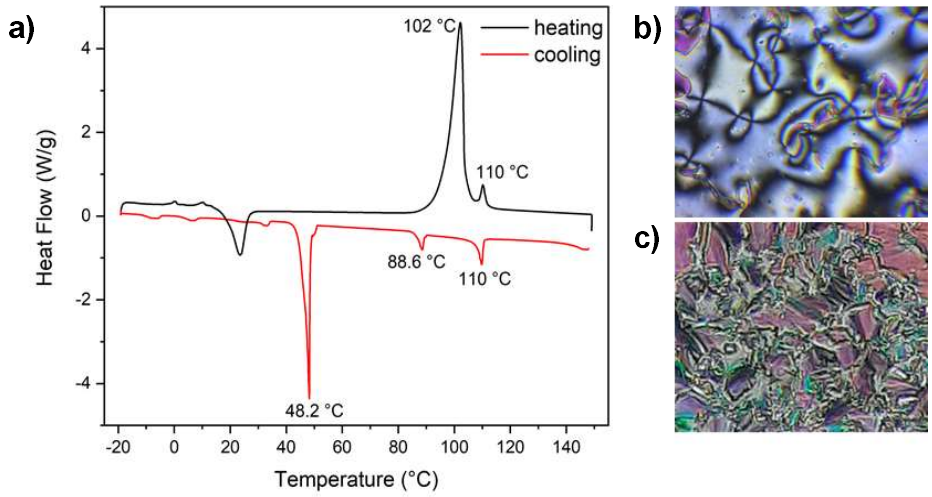

Figure 51 a) DSC traces (10 °C/min) corresponding to the third cycle of heating and second cycle of cooling of mesogens **Alk4 b)** POM image of **Alk4** at 110 °C in which *Schlieren* textures show a nematic phase **c)** POM image of **Alk4** at 90° C attributable at a smectic phase.

Alk3 does not present any liquid crystalline phase, and the DSC trace shows only the pick correspondent to its melting point around 67° C (**Figure 52**). **Alk5** demonstrated to be a liquid at room temperature, thus it is not useful for our purpose and was no further analysed.

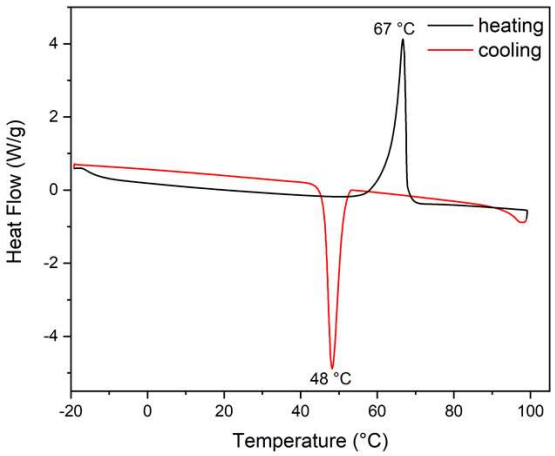

Figure 52 – DSC traces (10 °C/min) corresponding to the third cycle of hating and second cycle of cooling of monomer **Alk3**. This molecule does not present a LC phase.

3.2.4 Preparation and characterization of LCE films

Previous studies demonstrated as films obtained using **CL1** as crosslinker in 20 % mol/mol showed good mechanical properties, while lowering its amount led to a very sticky and difficult to handle material. For this reason, we focused our attention on mixture containing **CL1** in 20 % mol/mol. Once fixed the crosslinker amount, the stoichiometry of the reaction [151], [152], [176] guide the

composition of the mixtures, and the standard mixtures used are composed by dithiols in 60% mol/mol, alkyne in 20% mol/mol , and crosslinker in 20% mol/mol. Furthermore, all mixtures contain an UV photoinitiator (**Irgacure 369, IN1**, **Figure 53**) in 4% w/w needed to initiate the radical thiol-yne photopolymerization [117].

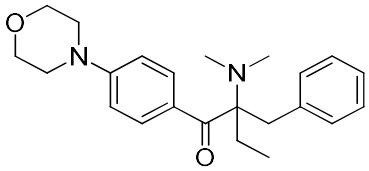

IN1

Figure 53 – Chemical structure of photoinitiator Irgacure 369 (IN1) used to perform the photopolymerization reaction between thiols and alkynes

Mixtures and their resultant polymers are noted according to the following nomenclature:

$$\mathbf{LCE_{a\text{-}b}}$$

where:

- *a* is the number associated to the thiol used;
- *b* is the number associated to the alkyne used;

In order to investigate the relationship between the architecture of the polymer and its stimulated deformation, we also prepared a homogeneous film not containing the alkyne in side-chain but only composed by the thiol and the crosslinker (**LCE_1**), thus presenting a main-chain architecture (**Figure 54**).

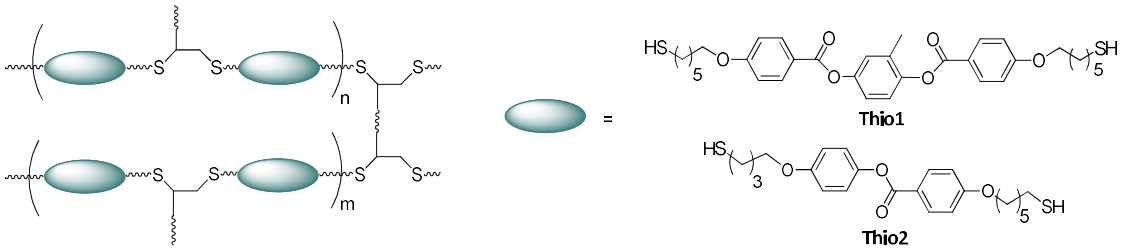

Figure 54 – Main-chain architecture obtained with 67% mol of thiol and 33% mol of CL1 and IN1 (4% w/w).

Such mixture was firstly observed at POM in order to detect the nematic to isotropic transition temperature and, thus to determine the best polymerization temperature **Thio1** was mixed with **Alk1**, **Alk3** and **Alk4** leading to the corresponding **$LCE_{1\text{-}1}$**, **$LCE_{1\text{-}3}$** and **$LCE_{1\text{-}4}$**. As reported above **Alk2** was not further investigate because of its smectic nature. **Thio2** only presented functional mixture with **Alk1** (**$LCE_{2\text{-}1}$**), while when mixed with the other alkynes smectic or even no LC phases were obtained.

Table 5 summarizes the transition temperatures detected by POM for all mixtures analysed.

Mixture	Phase transition temperatures [°C]	
LCE_1	h: Cr 85 N – I	c: I 102 N
$LCE_{1\text{-}1}$	h: Cr 90 N 120 I	c: I 110 N
$LCE_{1\text{-}3}$	h: Cr 80 N 120 I	c: I 94 N
$LCE_{1\text{-}4}$	h: Cr 80 N 120 I	c: I 108 N
$LCE_{2\text{-}1}$	h: Cr 45 N 60 I	c: I 50 N

Table 5 – Transition temperatures from LC to I phase determined by observation at POM.

As expected, mixtures containing **Thio1** show a higher transition temperature (around 100 °C) than the ones containing **Thio2** (around 50 °C). After cooling, any of the reported mixtures crystallize for several hours. This behaviour is very appealing to study the lithographic patterning of the materials since the process requires room temperature nematic monomers[121], [177].

To obtain the films, we prepared cells composed by two glasses coated with a sacrificial layer and separated by apposite spacers (75 µm), as shown in **Figure 55**.

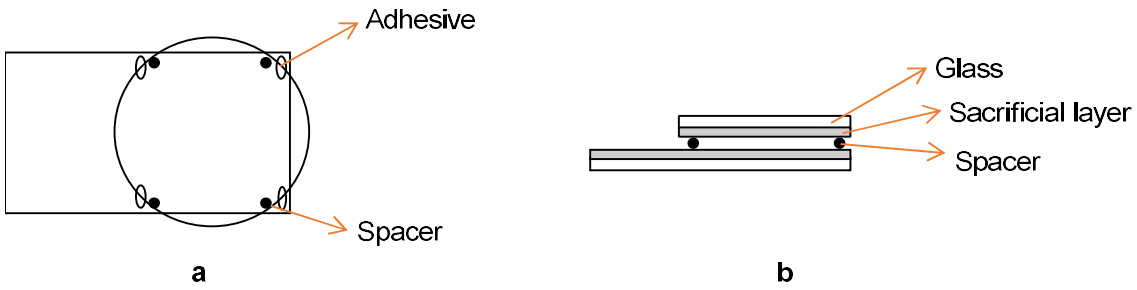

Figure 55 – Cell for LCE-based film preparation: a) top view **b)** lateral view

The monomer mixture was melted at its isotropic temperature and infiltrated by capillarity in the cell (**Figure 58a**). Cooling down slowly the cell from the isotropic to the nematic phase temperature, the LC mixture aligned through epitaxial growth on the coating surface. Type and quality of the reached alignment was evaluated and checked by POM observation by measuring the transmittance of the sample as a function of the rotating angle in respect to the cross polarizer. In a homogeneous LC, the transmittance changes and regular maximum and minimum values are observed by rotation of 90° of the polarizer with respect to the rubbing direction, while a homeotropic LC shows a very low transmittance without an angular dependence (**Figure 56**) [178].

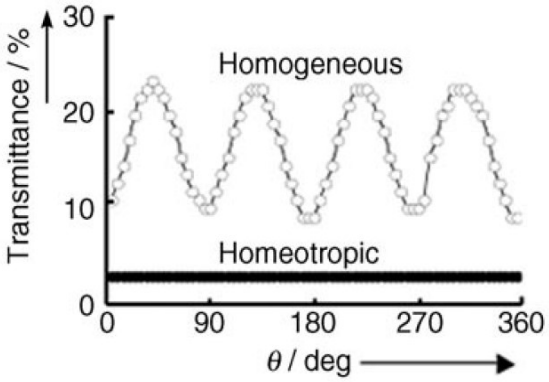

Figure 56 – Optical properties of homogeneous and homeotropic LCs analysed by POM. Images adacted from [178].

As an example, **Figure 57** shows the POM images of a cell infiltrated with a LC mixture (**$LCE_{2\text{-}1}$**) at different angles.

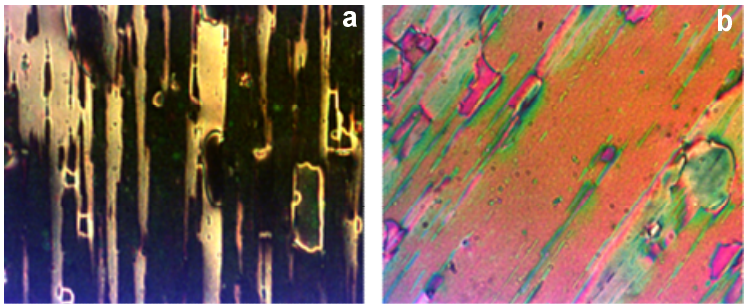

Figure 57 – POM images of the mixture $LCE_{2\text{-}1}$ infiltrated into a cell with a homogeneous alignment at nematic phase temperature. a) at 90 ° in respect to the polarizer **b**) rotate of 45°.

As evident from **Figure 57a**, we were not able to obtain a perfect alignment , nevertheless, this is the best result obtained with these mixtures, and it is possible to observe a strong change in the transmittance intensity when the sample is rotate to 45° with respect to the analyser (**Figure 57b**). Once the proper alignment is obtained, the temperature was maintained constant and polymerization is performed by irradiation with a UV lamp (**Figure 58b**). Such step requires 1 h at the temperature of the nematic phase and, to ensure a complete polymerization, 30 minutes at 100 °C for the mixtures containing **Thio1** or 30 minutes at 75 °C for the mixture containing **Thio2**. After polymerization, films were removed from the cell and their alignment was checked by POM (**Figure 58c**).

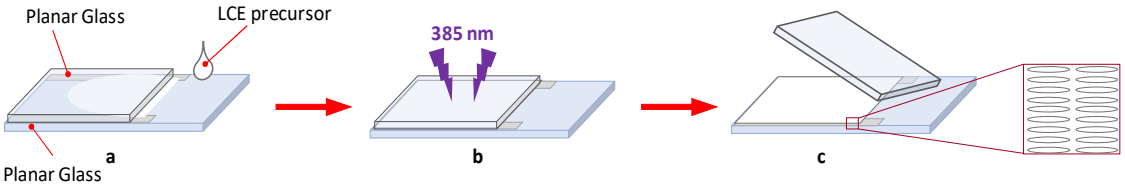

Figure 58 – Schematic fabrication of LCE-based polymeric film. a) infiltration of the LCE precursor into the cell at isotropic phase temperature b) polymerization with a UV source c) cleavage of the cell.

FT-IR spectra of the unpolymerized mixture, and then polymerized film, were recorded to check the polymerization grade of the samples. **Figure 59** shows the FTIR spectra of **LCE_{1-1}** (**Figure 59a**) and **LCE_{2-1}** (**Figure 59b**) confirming the polymerization of the mixtures by the disappearance of the pick relative to the C-H bond stretching of the terminal alkyne (3288 cm^{-1}).

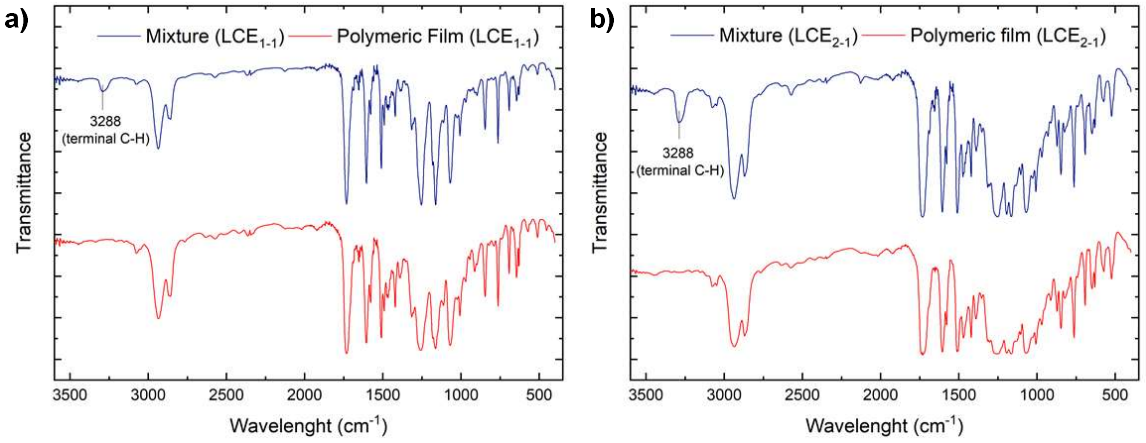

Figure 59 – FT-IR spectra of the LCE mixture acquired before (blue line) and after (red line) photopolymerization for LCE_{1-1} (a) and LCE_{2-1} (b).

The thermal properties of the polymers were studied by DMA and DSC analysis and the results are summarized in **Table 6**.

Film	T_g [°C][a]	T_{NI} [°C][b]	ΔH_{NI} [J/g][c]
LCE_{1-1}	16	146.5	2.12
LCE_{1-3}	8.9	150.2	0.95
LCE_{1-4}	22.7	151.0	1.26
LCE_{2-1}	1.2	84.2	1.3

Table 6 – Thermal properties of LCE films. [a]Determined from the midpoint of the baseline jump in DSC traces. [b] and [d] Determined respectively from the maximum and the area of the transition peak in the DSC traces.

As expected, changing the number of aromatic rings inside the core of the thiols composing the main chain of the polymers, from three of **Thio1** to two of **Thio2**, the transition temperature from nematic to isotropic phase strongly decreases, while only changing the alkyne. T_{NI} remains very similar for all samples prepared (**LCE_{1-1}**, **LCE_{1-3}**, **LCE_{1-4}**). Such results demonstrated how using this

reaction it is possible to simply and strongly modulate the T_{NI} of the LCE obtained by tailoring their chemical structure. In particular, such effect is mostly affected by the thiols in main-chain, while it seems to not be dependent from the alkynes in side-chain.

All T_g values are below the room temperatures, accordingly with experimental data reported in literature [151], [152] (**Figure 60** and **Table 6**) and, as expected, the polymer containing **Thio2** (presenting two aromatic rings in the main chain), shows lower T_g (1.2 °C) than polymers containing **Thio1** (having three aromatic rings in the core, 16, 8.9 and 22.7 °C, for **LCE_{1-1}**, **LCE_{1-3}** and **LCE_{1-4}**, respectively). Indeed, the introduction of stiff chemical groups interferes with the flowing process and hence increase the T_g. This effect is a consequence of the π-π stacking between the aromatic rings of adjacent chains, which increases with the number of the aromatic rings in the core of the mesogens. When the number of the aromatic rings in the main chain is comparable (polymers prepared by **Thio1**, **LCE_{1-1}**, **LCE_{1-3}** and **LCE_{1-4}**), the T_g behaviour is affected by the architecture: a *side-on* architecture (**LCE_{1-1}**) presents a T_g around 16° C, while an *end-on* architecture (**LCE_{1-3}**), presents a lower T_g, around 9° C. Interestingly, polymer **LCE_{1-4}**, also presenting an *end-on* architecture, shows the higher T_g of the series (23.5 °C). However, in this case the parameter is probably affect by the ability of the mesogen to form H-bonds influencing the cross-linkage of the main chains, and consequently increasing the hard-like properties of the final material.

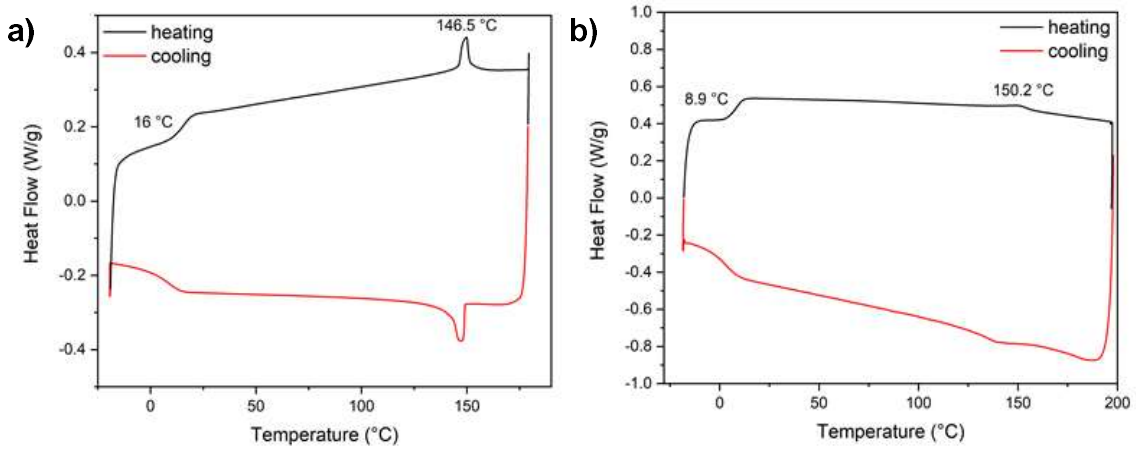

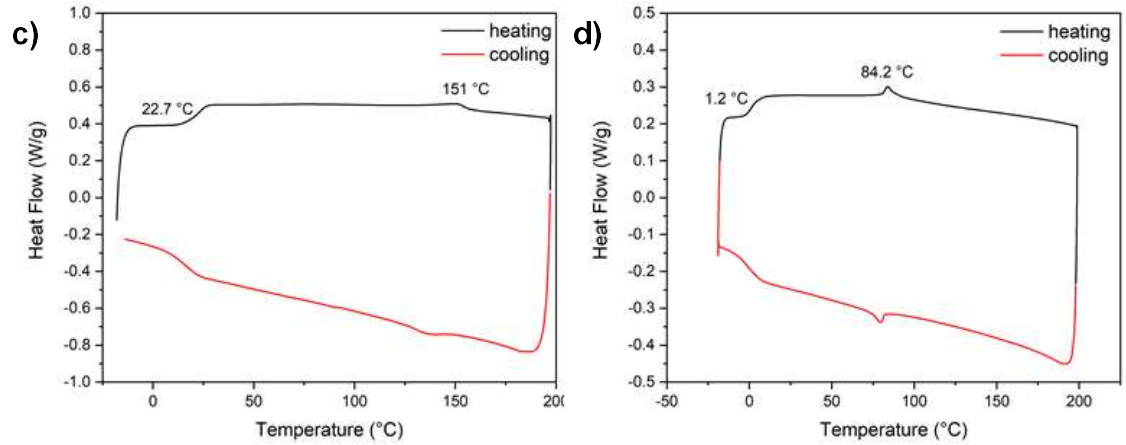

Figure 60 – DSC traces (10 °C/min) corresponding to the second cycle of heating of LCE films of samples $LCE_{1\text{-}1}$ (a), $LCE_{1\text{-}3}$ (b), LCE 1-4 (c) and **$LCE_{2\text{-}1}$ (d).**

Mechanical properties of the polymeric films were evaluated by DMA tests, in which the viscoelastic properties of the materials were studied under conditions of low applied stretching force along the mesogens alignment direction or perpendicular to it. All samples display a viscoelastic behaviour, hence a mixture of viscous and elastic behaviours, when they are under mechanical stress. The elastic portion (E') of the viscoelastic behaviour is more pronounced at low temperature, because the molecular network is less flexible and stiffer. On the other hand, at high temperature the molecular system is more flexible.

Temperature sweep is a test performed to characterize polymer structures and to describe the internal superstructure of the macromolecules. The temperature-dependent functions of storage modulus (E'), loss modulus (E'') and the loss factor (δ) are shown in **Figure 61** for every thiol-yne based polymers.

The outcomes of the temperature sweep show that from -50 to 90° C, the viscoelastic materials have a solid-like structure. Indeed, the elastic modulus (E') is higher than the viscous one (E''). At low temperatures (from -50 to 15° C) the materials have a strong consistence, in fact E' is more than one order of magnitude higher if compared to E''. Between 15° C and about 30° C the two moduli are superimposed, these means that a transition from a stiffer to a softer polymer occurs, T_g, in agreement with the DSC thermograms. At higher temperatures (above 40° C) the absolute values of both moduli decreases and also their difference, because the consistence of the materials become softer.

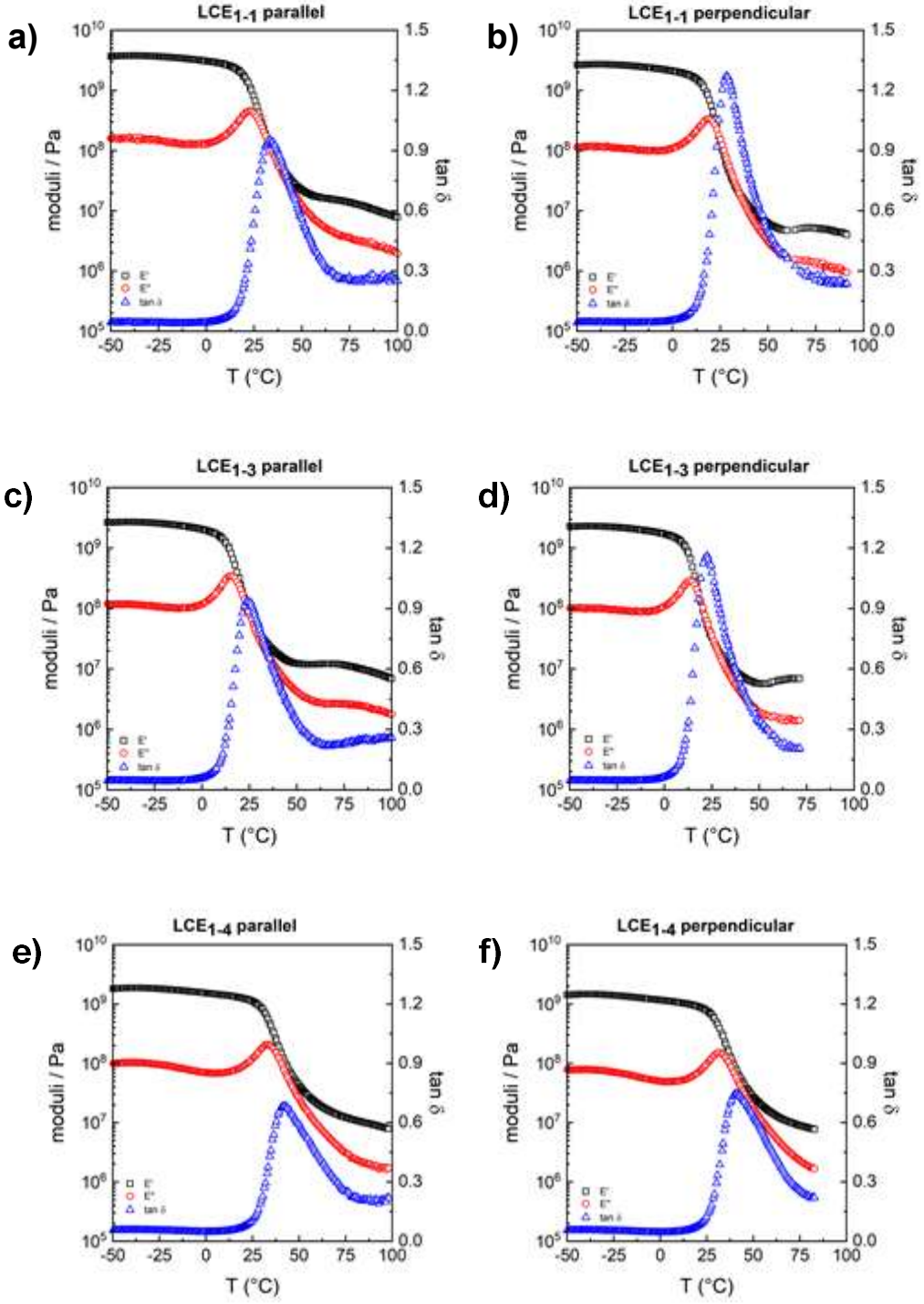
a)
LCE1-1 parallel
b)
LCE1-1 perpendicular
c)
LCE1-3 parallel
d)
LCE1-3 perpendicular
e)
LCE1-4 parallel
f)
LCE1-4 perpendicular
moduli / Pa
tan δ
T (°C)

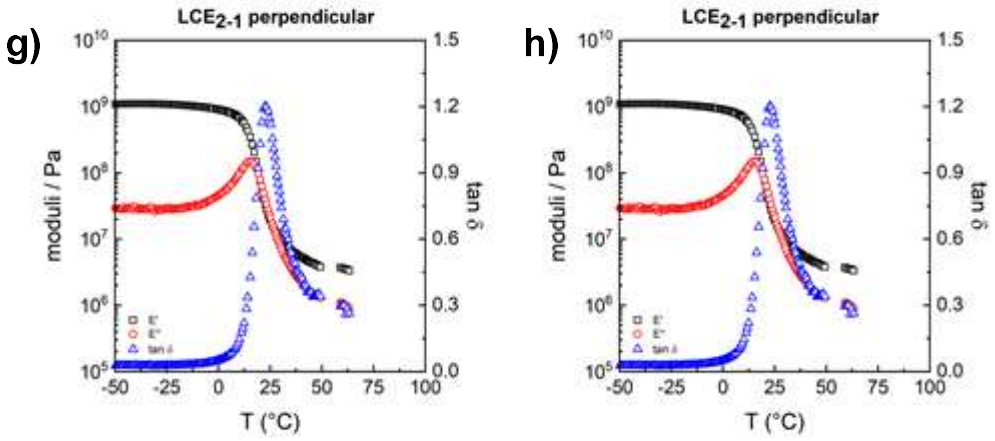

Figure 61 – DMA traces of polymeric films under conditions of low applied stretching force along the mesogens alignment direction or perpendicular to it.

The evaluation of the thermoresponsivity of the polymers was performed measuring the variation in length of a strip of film along the alignment axis, with respect to the variation of the temperature.

The pictures in **Figure 62** demonstrate that the contraction is reproducible (independently from the size of the polymer strip) and that a complete recovery take place after cooling (**Figure 62e**).

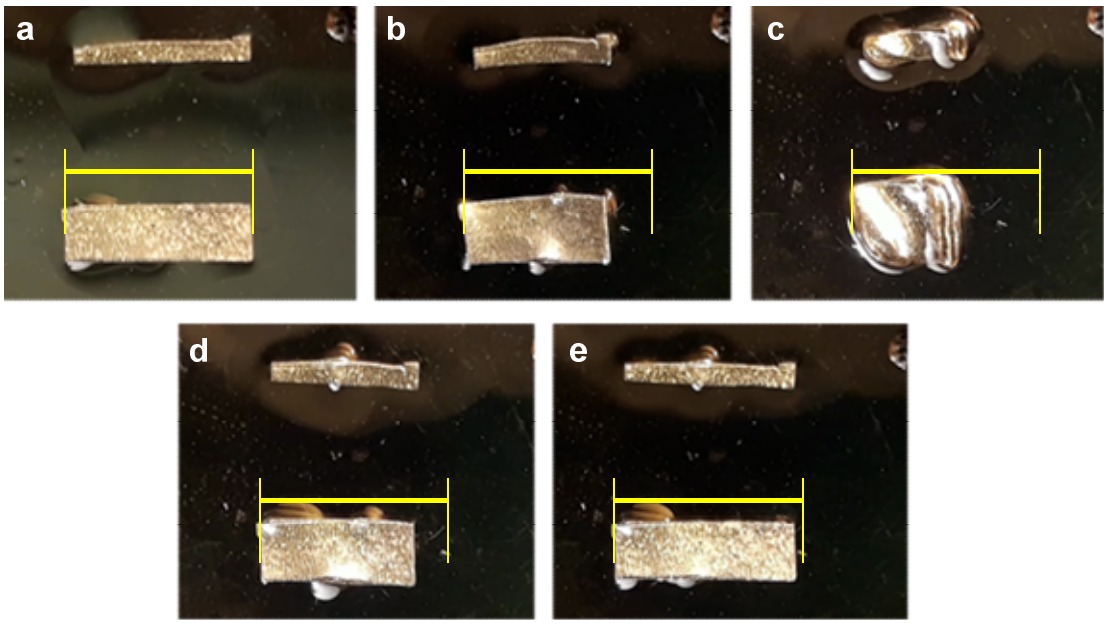

Figure 62 – Thermoresponsivity evaluation of a polymeric film of sample $LCE_{1\text{-}1}$ at room temperature (a), at 80 °C **(b),** at 150 °C **(c)** and again at 80 °C **(d),** at room temperature. The yellow bar indicates the sample size and it measures 1 cm.

The shape-recovery was estimated measuring the original length of the polymer strip (before the thermal cycle) and the length of the same polymer strip after the thermal cycle. The results are

reported in the graph in **Figure 63a**, and the percentage of the recovery are summarized in the table showed in **Figure63b**.

a)

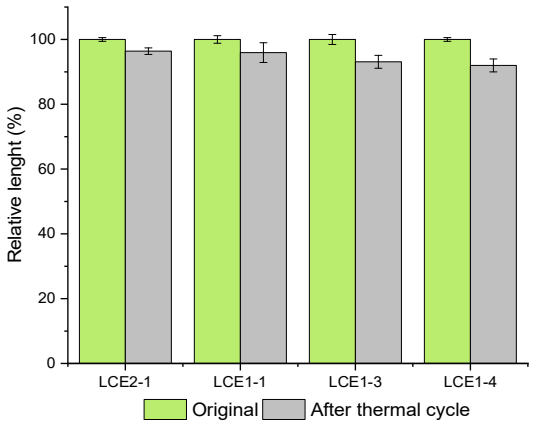

b)

Sample	Recovery (%)
$LCE_{1\text{-}1}$	99
$LCE_{1\text{-}3}$	99
$LCE_{1\text{-}4}$	99
$LCE_{2\text{-}1}$	99

Figure 63 – Estimation of shape-recovery in one thermal cycle. a) Relative length for every sample before the thermal cycle (in green) and after a complete thermal cycle (in grey) **b)** Percentage in recovery calculate for every sample after one thermal cycle

After a first thermal cycle (from 25 to 200° C), the polymer strips recovery their original dimension with a loss of length of about 1%. Probably, this is not a real loss of length but a loss of solvent of a post curing effect due to the first heating cycle. Further evaluations on this effect are under investigation.

The profiles of the deformations along the alignment axis, are shown in the graph below (**Figure 64**), in which the length of the polymer strip (in percentage) is plotted with respect to the variation of the temperature.

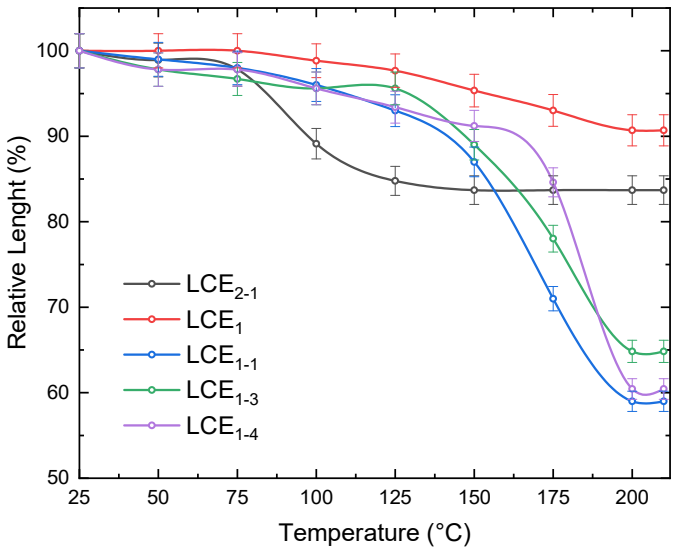

Figure 64 – Relative length (%) vs temperature. The film obtained with Thio2 (showing a two aromatic ring core) shows lower temperature of contraction but less % contraction at higher temperatures (black line). The film obtained with **CL1**, which correspond to a main-chain architecture, does not show significant contraction (< 10%).

The main chain polymer, obtained without addition of alkyne, (red line, **LCE$_1$**), shows a modest deformation (about 10% at 200°C), in line with some acrylate based LCE [179], as a result of the dense degree of crosslinking. Introduction of the alkynes in the composition leads to a decrease of the crosslinking degree and an increase in the deformations.

Polymers obtained using **Thio1** (containing three aromatic rings in the core, green, purple and blue lines corresponding to **LCE$_{1-1}$**, **LCE$_{1-3}$** and **LCE$_{1-4}$**, respectively), show high transition temperature but also big deformations (about 40%). Variation of the architecture from side-on to end-on in the side-chain component (**LCE$_{1-1}$** vs **LCE$_{1-3}$** and **LCE$_{1-4}$**), seems to not significantly influence the response of the polymers; while changing the thiol, from **Thio1** to **Thio2** containing two aromatic rings in the core (black line, **LCE$_{2-1}$**), leads to a decrease in the contraction temperature but also in a lower contraction percentage at higher temperature than previous discussed samples. From the literature, it is evident that also the mixed main-chain/side-chain architecture chosen for the discussed polymers plays a big role on polymer deformation degree [117].

These results are summarized in **Table 7**.

Film	Contraction (length %) at 200° C
LCE_1	9 %
LCE_{1-1}	41 %
LCE_{1-3}	35 %
LCE_{1-4}	39 %
LCE_{2-1}	16 %

Table 7 – Contraction in length (%) calculated for every sample during at the maximum contraction value, which correspond at 200 °C.

Polymers obtained with this reaction are very promising to fabricate materials able to undergo bigger deformations then acrylate-based materials. However, such synthetic approach still suffers from some drawbacks, such as the high polymerization and transition temperatures, that make difficult the integration with advanced polymerization techniques like the Direct Laser Writing Technique, used to prepare micro-actuators, and further studies are undergoing in our laboratories to improve this aspects. In fact, even though these drawbacks, thiol-yne still remain extremely interesting because of its peculiarity to lead to polymers which properties can be modulate by simple chemical modification both in the main-chain and side-chain components.
Moreover, the same characteristic could be used to develop materials which can undergo a shape change in a selective way, by the combination and integration of both elastomers (one with **Thio1** and one with **Thio2**). For this purpose, we prepared a structure combining two thiol-yne based polymers to form a square, in which two sides are made with one elastomer (**LCE_{1-1}**) and the other two are made with the other one (**LCE_{2-1}**), attached to each other with a small amount of adhesive, as shown in **Figure 65**.

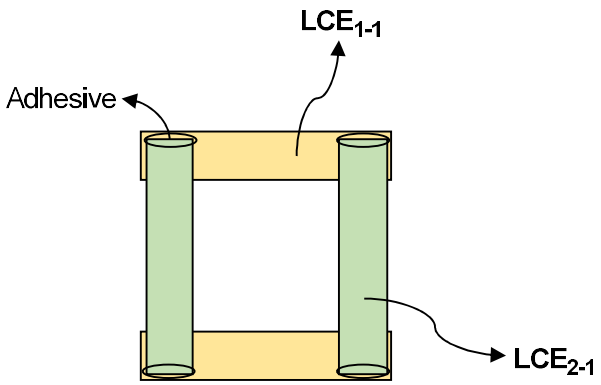

Figure 65 – Schematic fabrication of a composite obtained with two LCE-based film which are differentiated by a different thermoresponsive behaviour. In green a polymer characterized by lower temperatures of contraction; in orange a polymer characterized by higher temperatures of contraction.

To evaluate the selective contraction, the structure was put on a silicone oil drop on the top of a glass plate, and heated to induce the isotropic phase transition, as shown in **Figure 66**.

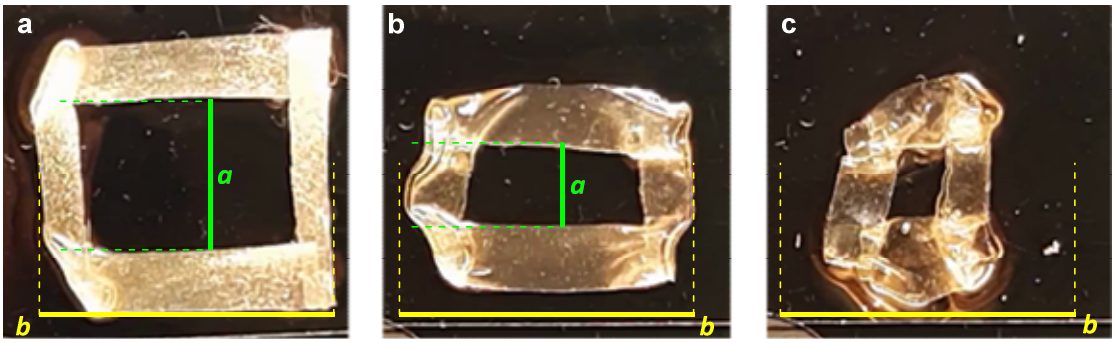

Figure 66 – Thermoresponsive behaviour of the composite. a) at room temperature **b)** at 90 °C, the deformation of one side (*a*, marked in green) is observed, while the other side stay approximatively unvaried (*b*, marked in yellow) **c)** at 180° C, the contraction of the other side too is observed.

At 90° C (**Figure 66b**) the contraction of **$LCE_{2\text{-}1}$** is at his maximum value, while **$LCE_{1\text{-}1}$** is not contracting (**Figure 66b**); at 180° C we have the complete deformation of both elastomers (**Figure 66c**).

The simple example demonstrated the selective thermal response of the device. Implementation on the materials and on the design could lead to more complex devices to be use for example in microfluidics to allow the selective modification of thermal valves or in micro-robotics to obtain thermal sensitive robots.

3.3 Experimental part

General methods. All reagents, solvents, and catalysts were commercially available and used as received, unless otherwise stated. All reactions were carried out under magnetic stirring and monitored by TLC on 0.25 mm silica gel plates (Merck F254). Column chromatography were carried out on Silica Gel 60 (32–63 μm) or on silica gel (230–400 mesh, Sigma-Aldrich) and on Alumina activated (Brockman I, 58 Å pore size, Sigma-Aldrich). Yields refer to spectroscopically and analytically pure compounds unless otherwise stated. 1H NMR spectra were recorded on a Varian Mercury-400 or on a Varian INOVA 400 instruments at 25 °C. 13C NMR spectra were recorded on a Varian Gemini-200 spectrometer. IR spectra were recorded with a BX FTIR Perkin-Elmer system spectrophotometer. ESIMS spectra were recorded with a Thermo Scientific™ LCQ fleet ion trap mass spectrometer. Elemental analyses were performed with a Perkin-Elmer 2400 analyzer. Thermal stability was characterized using a Q-5000 TA thermogravimetric analyzer at 10 °C/min under a nitrogen atmosphere up to 600 °C. Thermal transitions were measured using a DSC TA Instruments Q-20 calorimeter under a nitrogen atmosphere (heating and cooling rate: 10 °C/min). The light source was a photocalorimetry accessory from TA Instruments composed by a 200 W high pressure Hg source provided with a 250–450 nm filter. Light was transmitted to the sample through an extended range dual-quartz light guide. Polarized optical microscopy (POM) was performed using an Olympus BH-2 polarizing microscope fitted with a Linkam THMS600 hot stage.

benzyl 4-hydroxybenzoate (**8**). To a mixture of 4-hydroxybenzoic acid (5 g, 36.20 mmol) and $NaHCO_3$ (6.08 g, 74.40 mmol) in DMF (55 mL), benzyl bromide (6.2 g, 36.20 mmol) was added. The mixture was stirred at 90° C for 18h. After cooling, water was added (50 mL) and the mixture was extracted with AcOEt (40 mL x3). The combined organic layers were washed with water (150 mL x2), dried over Na_2SO_4 and filtered. After the evaporation of the solvent, under reduced pressure, the crude product is obtained with a yield of 95% (7.91 g, 34.65 mmol) and used without purification. ^{1}H-NMR (200 MHz, $CDCl_3$) δ = 8.03–7.97 (m, 2H, Ar), 7.43-7.37 (m, 5H, Ar), 6.88-6.83 (m, 2H, Ar), 5.34 (s, 2H, Bn) ppm.

benzyl 4-((6-bromohexyl)oxy)benzoate (**9**). A mixture of **8** (7.22 g, 31.63 mmol), 1,6-dibromohexane (30.25 g, 124 mmol), K_2CO_3 (6.42 g, 46.45 mmol) and acetone (125 mL) was stirred at reflux for 18h. After cooling to room temperature, the mixture was filtered through Celite pad and the filtrate was evaporated under reduced pressure. The crude product was purified by FCC (only EP, and then EP:AcOEt 7:1, R_f = 0.58) affording the desired product in 68% yield (8.35 g, 21.33 mmol). ^{1}H-NMR (400 MHz, $CDCl_3$) δ = 8.05-8.02 (m, 2H, Ar), 7.46-7.32 (m, 5H, Ar), 6.92-6.89

(m, 2H, Ar), 5.34 (s, 2H, Bn), 4.00 (t, *J* = 8 Hz, 2H, ArO-*CH*$_2$), 3.42 (t, *J* = 8 Hz, 2H, -*CH*$_2$Br), 1.91-.1.79 (m, 4H, aliphatic, -C*H*$_2$-), 1.52-1.49 (m, 4H, aliphatic, -*CH*$_2$-) ppm.

4-((6-bromohexyl)oxy)benzoic acid (**10**). To a solution of **9** (12.4 g, 31.7 mmol) in cyclohexene (65 mL) and ethanol (65 mL), 10% of $Pd(OH)_2$ (1.24 g) was added. The mixture was stirred on reflux for 18h, filtered through Celite pad and the filtrate was evaporated under reduced pressure. The crude product was crystallized by methanol and obtained pure product as white solid in 76% yield (7.71 g, 25.6 mmol). ^{1}H-NMR (400 MHz, $CDCl_3$) δ = 8.06-8.04 (m, 2H, Ar), 6.94-6.92 (m, 2H, Ar), 4.04 (t, *J* = 6 Hz ,2H, ArO-*CH*$_2$), 3.43 (t, *J* = 8 Hz ,2H, ArO-*CH*$_2$), 1.92-.1.82 (m, 4H, aliphatic, -CH_2), 1.53-1.52 (m, 4H, aliphatic, -CH_2-) ppm.

2-methyl-1,4-phenylene bis(4-((6-bromohexyl)oxy)benzoate) (**11**).

1. Procedure with DCC and DMAP

To a solution of **10** (242.61 mg, 0.80 mmol) in CH_2Cl_2 dry (3 mL), DCC (190 mg, 0.92 mmol), DMAP (93 mg, 0.76 mmol) and p-toluenesulfonic acid (13.08 mg, 0.076 mmol) were added under N_2 atmosphere at room temperature for 18 h. The mixture was concentrated under reduced pressure and purified by FCC (Hex:AcOEt 4:1 R_f = 0.41) to provide the product as a white solid in 34% yield (95 mg, 0.13 mmol). ^{1}H-NMR (200 MHz, $CDCl_3$) δ = 8.19-8.12 (m, 4H, Ar), 7.20-6.95 (m, 7H, Ar), 4.06 (t, J = 6 Hz, 4H, ArO-*CH*$_2$), 3.44 (t, J = 6 Hz, 4H, ArO-*CH*$_2$), 2.24 (s, 3H, Me), 1.95-1.82 (m, 8H, aliphatic, -C*H*$_2$-), 1.57-1.50 (m, 8H, aliphatic, -C*H*$_2$-) ppm.

2. Procedure with EDC and DMAP

To a solution of **10** (1.00 g, 3.32 mmol) in THF dry (35 mL), methylhydroquinone (206.07 mg, 1.66 mmol), EDC (566 mg, 3.65 mmol) and DMAP (61.08 mg, 0.50 mmol) were added under N_2 atmosphere. The reaction was stirred at room temperature and under N_2 atmosphere for 18 h. A solution of NH_4Cl (35 mL) was added and the product was extract with AcOEt (20 mL x3). The organic phase was dried, filtered and concentrate under reduced pressure. The purification through FCC (EP:AcOEt 2:1 R_f = 0.6) provided a white solid in 6% yield (75 mg, 0.10 mmol). ^{1}H-NMR (200 MHz, $CDCl_3$) δ = 8.21-8.15 (m, 4H, Ar), 7.24-7.00 (m, 7H, Ar), 4.12 (t, J = 2 Hz, 4H, ArO-*CH*$_2$), 3.45 (t, J = 6 Hz, 4H, ArO-*CH*$_2$), 2.10 (s, 3H, Me), 2.00-1.79 (m, 8H, aliphatic, -C*H*$_2$-), 1.60-1.49 (m, 8H, aliphatic, -C*H*$_2$-) ppm.

3. Procedure with EDC·HCl and DMAP

To a solution of **10** (2.295 g, 7.62 mmol) in DMF dry (25 mL), EDC·HCl (1.70 g, 8.89 mmol) and DMAP (775.8 mg, 6.35 mmol) were added under N_2 atmosphere and at room temperature. After 20 minutes, 2-methylhydroquinone (315.31 mg, 2.54 mmol) was added and the mixture was stirred at room temperature under N_2 atmosphere for 18 h. The mixture was diluted with water (50 mL) and extracted with AcOEt (30 mL x3). The combined organic phases were washed with H_2O (100 mL x2), dried with Na_2SO_4, filtered and evaporated under reduced pressure. The resulting residue was purified by crystallization by ethanol to provide the product as a white solid in 40% yield (700 mg, 1.01 mmol). ^{1}H-NMR (400 MHz, $CDCl_3$) δ = 8.18-8.13 (m, 4H, Ar), 7.17 (d, J = 12 Hz, 1H, Ar), 7.13 (d, J = 2.4 Hz, 1H), 6.97 (dd, J = 12, 2.4 Hz, 1H, Ar), 6.99-6.96 (m, 4H, Ar), 4.08-4.04 (m, 4H, ArO-*CH*$_2$), 3.57 (t, J = 4 Hz, 4H, ArO-*CH*$_2$), 2.25 (s, 3H, Me), 1.86-1.80 (m, 8H, aliphatic, -C*H*$_2$-), 1.55-1.53 (m, 8H, aliphatic, -C*H*$_2$-) ppm.

4. Procedure with oxalyl chloride

2-methyl-1,4-phenylene bis(4-((6-bromohexyl)oxy)benzoate) (**11**). To a solution of **10** (1.66 g, 5.51 mmol) in CH_2Cl_2 (55 mL), DMF dry (85.6 uL) and then oxalyl chloride (1.4 g, 11.11 mmol) were added dropwise at 0° C under N_2 atmosphere. After 4 hours the reaction mixture was concentrated under reduce pressure and used for the next step. In the same flask of the previous step, methylhydroquinone (342 mg, 2.75 mmol) was added under N_2 atmosphere and the solids were solubilized in THF dry (55 mL). TEA dry (835 mg, 8.26 mmol) was added dropwise and the reaction was stirred under N_2 atmosphere for 18 h. At the organic phase, CH_2Cl_2 (50 mL) was added and then washed with a solution of NH_4Cl (100 mL). The aqueous phase was extracted with CH_2Cl_2 (50 mL x3), dried over Na_2SO_4, filtered and concentrated under reduced pressure. The crude product was purified by FCC (EP:AcOEt 4:1, R_f = 0.24) to provide the product in 62% yield (1.19 g, 1.72 mmol). ^{1}H-NMR (200 MHz, $CDCl_3$) δ = 8.19-8.12 (m, 4H, Ar), 7.26-6.95 (m, 7H, Ar), 4.06 (t, J = 6 Hz, 4H, ArO-*CH*$_2$), 3.44 (t, J = 8 Hz, 4H, ArO-*CH*$_2$), 2.24 (s, 3H, Me), 1.95- 1.85 (m, 8H, aliphatic, -C*H*$_2$-), 1.56-1.52 (m, 8H, aliphatic, -C*H*$_2$-) ppm.

2-methyl-1,4-phenylene bis(4-((6-(acetylthio)hexyl)oxy)benzoate) (**12**). To a solution of **11** (700 mg, 1.014 mmol) in DMF (20 mL), KSAc (695 mg, 6.084 mmol) was added. The mixture was stirred at room temperature for 4 h. Water was added (15 mL) and the product was extracted with AcOEt (15 mL x3). The combined organic layers were washed with brine (20 mL) and then with water several times. Finally, the organic layer was dried with Na_2SO_4, filtered and concentrated under reduced pressure. The white solid was crystallized by ethanol, providing the pure product in 94% yield (654 mg, 0.96 mmol). ^{1}H-NMR (400 MHz, $CDCl_3$) δ = 8.17-8.12 (m, 4H, Ar), 7.17 (d, J = 8 Hz,

1H, Ar), 7.12 (d, J = 4 Hz, 1H, Ar), 7.07 (dd, J = 8, 4 Hz, 1H, Ar), 6.99-6.95 (m, 7H, Ar), 4.06-4.02 (m, 4H, ArO-C*H*$_2$-), 2.89 (t, J = 8 Hz, 4H, AcOS-C*H*$_2$-), 2.33 (s, 6H, Me), 2.24 (s, 3H, Me), 1.84-1.79 (m, 4H, aliphatic, -C*H*$_2$), 1.66-1.59 (m, 4H, aliphatic, -C*H*$_2$-), 1.53-1.43 (m, 8H, aliphatic, -C*H*$_2$-) ppm.

2-methyl-1,4-phenylene bis(4-((6-mercaptohexyl)oxy)benzoate) (**Thio1**). To a mixture of **12** (500 mg, 0.734 mmol) in THF (2 mL), $NaBH_4$ (835 mg, 22.00 mmol) was added at 0°C. After 10 minutes, water was added (10 mL) and the mixture was heating to room temperature and stirred for 24 h. After this time, a solution of HCl 3N (10 mL) was added and the product was extracted with AcOEt (15 mL x3). The combined organic layers were dried over Na_2SO_4, filtered and evaporated under reduced pressure. The crude product was purified by crystallization by ethanol, affording the desired product in 68% yield. ^{1}H-NMR (200 MHz, $CDCl_3$) δ = 8.25-8.18 (m, 4H, Ar), 7.32-7.01 (m, 7H, Ar), 4.11 (t, J = 8 Hz, 4H, ArO-C*H*$_2$-), 2.68-2.57 (m, 4H, HS-C*H*$_2$-), 2.31 (s, 3H, Me), 1.94-1.84 (m, 4H, aliphatic, -C*H*$_2$), 1.77-1.70 (m, 4H, aliphatic, -C*H*$_2$), 1.64-1.52 (m, 8H, aliphatic, -C*H*$_2$), 1.42 (t, J = 6 Hz, 2H, -SH) ppm. ^{13}C NMR (100 MHz, $CDCl_3$) δ = 164.9 (s, C=O), 164.5 (s, C=O), 163.5 (s, 2C, Ar), 148.4 (s, Ar), 147.1 (s, Ar), 132.3 (d, 4C, Ar), 131.8 (s, Ar), 124.1 (d, Ar), 122.9 (d, Ar), 121.6 (s, Ar), 121.5 (d, Ar), 120.0 (s, Ar), 114.4, 114.3, (d, 4C, Ar), 68.1 (t, 2C, ArO-*C*H$_2$), 33.9, 29.0, 28.1, 25.5 (t, 8C, aliphatic –CH$_2$-), 24.5 (t, 2C, A-*C*H$_2$Br), 16.4 (q, Me). IR (KBr): 2938, 2856, 1730, 1603, 1510, 1182 cm^{-1}; MS (MALDI-TOF) *m/z*: 619.3 ([M+Na]$^+$; 100); Anal. Calcd for $C_{33}H_{40}O_6S_2$ (596.80): C 66.41, H 6.76, S 10.75; found C 66.25, H 6.99, S 10.99.

1-(benzyloxy)-4-(4-bromobutoxy)benzene (**13**). A mixture of 4-(benzyloxy)phenol (2.5 g, 12.48 mmol), 1,4-dibromobutane (10.78 g, 49.94 mmol), K_2CO_3 (2.6 g, 18.727 mmol) and acetone (125 mL) was stirred at reflux for 18h. After cooling to room temperature, the mixture was filtered through Celite pad and washed with acetone. The filtrate was evaporated under reduced pressure. The crude product was crystallized by ethanol affording the desired product **13** in 65% yield (4.185 g, 12.485 mmol). ^{1}H-NMR (200 MHz, $CDCl_3$) δ = 7.41-7.34 (m, 5H, Ar), 6.92-6.79 (m, 4H, Ar), 5.02 (s, 2H, Bn), 3.94 (t, J = 6 Hz, 2H, ArO-*CH*$_2$), 3.49 (t, J = 6 Hz, 2H, -*CH*$_2$Br), 2.17-1.92 (m, 4H, aliphatic -C*H*$_2$-) ppm.

4-(4-bromobutoxy)phenol (**14**). To a solution of **13** (9.5 g, 28.34 mmol) in cyclohexene (95 mL) and ethanol (95 mL), 10% of $Pd(OH)_2$ (950 mg) was added. The mixture was stirred on reflux for 18h, filtered through Celite pad and the filtrate was evaporated under reduced pressure. The crude was purified by FCC (EP:AcOEt 5:1 Rf = 0.73), providing the desired product in quantitative yield

(6.94 g, 28.34 mmol). ^{1}H-NMR (200 MHz, $CDCl_3$) δ = 6.81-6.72 (m, 4H, Ar), 3.93 (t, *J* = 6 Hz ,2H, ArO-*CH_2*), 3.48 (t, *J* = 8 Hz ,2H, -*CH_2*Br), 2.14-1.84 (m, 4H, aliphatic, -C*H_2*) ppm.

4-(4-bromobutoxy)phenyl 4-((6-bromohexyl)oxy)benzoate (**15**). To a solution of **14** (3.662 g, 15 mmol) and **10** (4.5 g, 15 mmol) in CH_2Cl_2 dry (150 mL), DCC (3.082 g, 15 mmol)and DMAP (0.2 g, 1.64 mmol) were added under N_2 atmosphere. The mixture was stirred for 18 h and then filtered. The organic phase was washed with water (100 mL), acetic acid 5% v/v and then with water (100 mL). After it was dried on Na_2SO_4, filtered and concentrate under reduce pressure to obtain the crude as yellow solid. The successive purification through crystallization by ethanol allows to obtain the pure product as white solid in 80% yield (6.4 g, 12.11 mmol). ^{1}H-NMR (200 MHz, $CDCl_3$) δ = 8.15-8.11 (m, 2H, Ar), 7.13-7.08 (m, 2H, Ar), 6.98-6.89 (m, 4H, Ar), 4.08-3.57 (m, 4H, ArO-*CH_2*), 3.53-3.40 (m, 4H, -*CH_2*-Br), 2.15-1.81 (m, 8H, aliphatic, -C*H_2*), 1.57-1.50 (m, 4H, aliphatic, -C*H_2*) ppm.

4-(4-(acetylthio)butoxy)phenyl 4-((6-(acetylthio)hexyl)oxy)benzoate (**16**). To a solution of **15** (2.88 g, 5.45 mmol) in DMF (50 mL), KSAc (3.73 g, 32.7 mmol) was added. The solution was stirred for 2h30m at room temperature. Then, water was added (50 mL) and the product was extracted with AcOEt (30 mL x3). The combined organic layers were dried on Na_2SO_4, filtered and concentrate under reduce pressure to obtain the crude as brown solid. The crude product was purified by crystallization by ethanol to obtain the pure product as white solid in 88% yield (2.50 g, 4.81 mmol). ^{1}H-NMR (400 MHz, $CDCl_3$) δ = 8.13-8.10 (m, 2H, *H_1*,*H_2*), 7.11-7.07 (m, 2H, *H_3*, *H_4*), 6.96-6.89 (m, 4H, *H_5*, *H_6*, *H_7*, *H_8*), 4.03 (t, J = 4 Hz, 2H, ArO-*CH_2*), 3.97 (t, J = 4 Hz, 2H, ArO-*CH_2*), 2.95 (t, J = 8 Hz, 2H, -*CH_2*-SAcO), 2.88 (t, J = 8 Hz, 2H, -*CH_2*-SAcO), 2.34 (s, 3H, *CH_3*), 2.33 (s, 3H, *CH_3*), 1.88-1.75 (m, 6H, aliphatic, -*CH_2*), 1.65-1.58 (m, 2H, aliphatic, -*CH_2*), 1.54-1.43 (m, 4H, aliphatic, -*CH_2*) ppm.

4-(4-mercaptobutoxy)phenyl 4-((6-mercaptohexyl)oxy)benzoate (**Thio2**). In a solution of **16** (1.50 g, 2.90 mmol) in THF (10 mL), $NaBH_4$ (3.30 g, 87 mmol) was added. At 0° C water (50 mL) was added and the reaction was stirred for 24 h at room temperature. Then, THF was distillate under reduced pressure, water was added, and the product was extracted with CH_2Cl_2 (20 mL x3). The combined organic layers were dried on Na_2SO_4, filtered and concentrate under reduce pressure to obtain the crude which purified by FCC on alumina (EP:AcOEt 6:1 R_f = 0.61) and obtain the pure product in 67% yield (845 mg, 1.94 mmol). ^{1}H-NMR (400 MHz, $CDCl_3$) δ = 8.14-8.12 (m, 2H, *H_1*,*H_2*), 7.11-7.09 (m, 2H, *H_3*, *H_4*), 6.97-6.90 (m, 4H, *H_5*, *H_6*, *H_7*, *H_8*), 4.04 (t, J = 4 Hz, 2H, ArO-*CH_2*), 3.98 (t, J = 4 Hz, 2H, -*CH_2*-SAcO), 1.92-1.79 (m, 6H, aliphatic, -*CH_2*), 1.70-1.63 (m, 2H, aliphatic, -*CH_2*), 1.50-

1.48 (m, 4H, aliphatic, -*CH*$_2$), 1.41-1.33 (m, 2H, -S*H*) ppm. ^{13}C NMR (50 MHz,) δ = 165 (s, C=O), 163.1 (s, Ar), 156.33 (s, Ar), 144.29 (s, Ar), 132 (s, 2C, Ar), 122.3 (s, 2C, Ar), 121.5 (s, Ar), 114.83 (s, 2C, Ar), 114 (s, 2C, Ar) 76.8 (t, ArO-*C*H$_2$), 76.5 (t, ArO-*C*H$_2$), 33.6, 30.4, 28.7, 27.8, 27.7, 25.3 (s, 6C, aliphatic, -*C*H$_2$-)24.3 (-*C*H$_2$-SH), 24.2 (-*C*H$_2$-SH) ppm. IR (KBr): 2937, 2862, 2571, 1722, 1606, 1514, 1512, 1280, 1197 cm^{-1}.

benzyl 2,5-dihydroxybenzoate (**17**). A mixture of 2,5diydroxybenzoic acid (2.15 g, 13.95 mmol) $NaHCO_3$ (3.39 g, 84.01 mmol) in DMF (20 mL) was stirred at 70 °C for 1 h. Then benzyl bromide (1.66 mL, 13.95 mmol) was added and the mixture was heated for 4 h. The mixture was cooled, diluted with water (100 mL) and extracted with 100 mL of AcOEt (100 mL x2). The organic phases were washed with water (200 mL x2), dried over Na_2SO_4, filtered and evaporated under reduced pressure affording the desired product in 90% yield (3.05 g, 12.49 mmol) as a white solid. ^{1}H-NMR (400 MHz, $CDCl_3$) δ = 7.45-7.37 (m, 5H, Ar), 7.32 (d *J* = 3.0 Hz, 1H, Ar), 7.01 (dd, *J* = 8.9, 3.0 Hz, 1H, Ar), 6.89 (d, *J* = 8.9 Hz, 1H, Ar), 5.37 (s, 2H, Bn), 4.46 (s, 2H, OH) ppm.

2-((benzyloxy)carbonyl)-1,4-phenylene bis(4-butylbenzoate) (**18**). A mixture of **17** (3.05 g, 12.49 mmol), 4-butyloxybenzoic acid (5.33 g, 27.38 mmol), DCC (5.67 g, 27.48 mmol) and DMAP (335 mg, 2.75 mmol) in dry CH_2Cl_2 (100 mL) was stirred at room temperature under Ar atmosphere for 12 h. The *N*,*N*-dicyclohexylurea was filtered and the filtrate was washed with water (100 mL), 5% acetic acid solution (100 mL) and water (100 mL). The organic layers were dried over Na_2SO_4, filtered and evaporated under reduced pressure. The crude material was recrystallized from ethanol affording the desired product in 81% yield (6.07 g, 10.17 mmol) as a white solid. ^{1}H-NMR (400 MHz, $CDCl_3$) δ = 8.15-8.12 (m, 2H, Ar), 8.08-8.06 (m, 2H, Ar), 7.91 (d, *J* = 2.9 Hz, 1H, Ar), 7.53 (d, *J* = 8.9 Hz, 1H, Ar), 7.46 (dd, *J* = 8.9, 2.9 Hz, 1H, Ar), 7.26-7.24 (m, 5H, Ar), 6.99-6.96 (m, 2H, Ar), 6.93-6.90 (m, 2H, Ar), 5.19 (s, 2H, Bn), 4.06 (t, *J* = 6.5 Hz, 4H, ArO-*CH*$_2$-A), 1.86-1.75 (m, 4H, aliphatic -*CH*$_2$-), 1.57-1.48 (m, 4H, aliphatic -*CH*$_2$-), 1.00 (t, *J* = 7.1 Hz, 6H, Me) ppm.

2,5-bis((4-butylbenzoyl)oxy)benzoic acid (**19**). A solution of **18** (6.07 g, 10.17 mmol) in CH_2Cl_2 (150 mL) was hydrogenate in the presence of 10 % Pd/C (600 mg) for 48 h. The mixture was filtered through a Celite pad, washed with CH_2Cl_2 and evaporated to give the product in 89% yield (4.61 g, 9.10 mmol) as a white solid. ^{1}H-NMR (400 MHz, $CDCl_3$) δ = 8.15-8.12 (m, 4H, Ar), 7.94 (d, *J* = 2.7 Hz, 1H, Ar), 7.51 (dd, *J* = 8.6, 2.7 Hz, 1H, Ar), 7.30 (d, *J* = 8.6 Hz, 1H, Ar), 6.99-6.95 (m, 4H, Ar), 4.08-4.03 (m, 4H, ArO-*CH*$_2$-A), 1.84-1.76 (m, 4H, aliphatic -*CH*$_2$-), 1.56-1.48 (m, 4H, aliphatic -*CH*$_2$-), 1.00 (t, *J* = 7.4 Hz, 6H, Me) ppm.

4-(prop-2-yn-1-yloxy)butan-1-ol (**20**). A solution of 1,4-butanediol (25 g, 278 mmol) in DMF (40 mL) was added dropwise into a suspension of sodium hydride (60% w/w in mineral oil, 10.3 g, 257 mmol) in DMF (70 mL) at 0 °C. After being stirred for 30' at 0 °C, a solution of propargyl bromide (80% w/w in toluene, 10.33 g, 69.5 mmol) in DMF (25 mL) was added. The mixture was stirred for 18 h at room temperature the water was added (400 mL) and the product was extracted with AcOEt (300 mL). The organic phase was washed twice with water, dried over $MgSO_4$, filtered and concentrated under reduced pressure. The crude product was purified by FCC (hexane:AcOEt 1:1, R_f = 0.35) affording the desired product in 71 % yield (6.3 g, 49.2 mmol) as a yellow liquid. ^{1}H-NMR (400 MHz, $CDCl_3$) δ = 4.13 (d, *J* = 2.4 Hz, 2H, OC*H2*-C≡CH), 3.64 (t, *J* = 5.8 Hz, 2H, C*H*$_2$OCH$_2$-C≡CH), 3.55 (t, *J* = 5.8 Hz, 2H, C*H*$_2$OH),2.56 (broad s, 1H, OH), 2.42 (t, *J* = 2.4 Hz, 1H, OCH$_2$-C≡C*H*), 1.70-1.62 (m, 4H, aliphatic -*CH*$_2$-) ppm.

2-((4-(prop-2-yn-1-yloxy)butoxy)carbonyl)-1,4-phenylene bis(4-butylbenzoate) (**Alk1**). A solution of **19** (2 g, 3.95 mmol), **20** (506 mg, 3.95 mmol), DCC (896 mg, 4.34 mmol) and DMAP (53 mg, 0.43 mmol) in 100 mL of dry CH_2Cl_2 was stirred at room temperature under Ar atmosphere for 18 h. The *N*,*N*-dicyclohexylurea was filtered and the filtrate was washed with water (100 mL), 5% acetic acid solution (100 mL) and water (100 mL). The organic layers were dried over $MgSO_4$, filtered and evaporated under reduced pressure. The crude material was purified by FCC (hexane:AcOEt 8:1, R_f = 0.14) affording the desired product in 75% yield (1.82 g, 2.96 mmol) as a white solid. If the product contains impurities it can be recrystallized from ethanol. ^{1}H-NMR (400 MHz, $CDCl_3$) δ = 8.17-8.14 (m, 4H, Ar), 7.89 (d, *J* = 2.8 Hz, 1H, Ar), 7.46 (dd, *J* = 8.7, 2.8 Hz, 1H, Ar), 7.26 (d, *J* = 8.7 Hz, 1H, Ar), 7.00-6.97 (m, 4H, Ar), 4.21-4.18 (m, 2H, OC*H*$_2$-C≡CH), 4.07-4.05 (m, 6H, ArO-C*H*$_2$-A), 5.40 (t, *J* = 6.0 Hz, 2H, C*H*$_2$OCH2- C≡CH), 2.39 (t, *J* = 2.4 Hz, 1H, OCH$_2$-C≡C*H*), 1.85-1.78 (m, 4H, aliphatic -*CH*$_2$-), 1.60-1.50 (m, 8H, aliphatic -*CH*$_2$-), 1.00 (t, *J* = 7.4 Hz, 6H, Me) ppm; ^{13}C NMR (100 MHz, $CDCl_3$) δ 165.0, 164.7, 164.2, 163.9, 163.7, 148.5, 148.3 (s, 7C, 3C=0, 4Ar), 132.6 (d, 2C,Ar), 132.5 (d, 2C,Ar), 127.3, 125.1, 125.0 (d, 3C, Ar), 124.9, 121.6, 121.2 (s, 3C, Ar), 114.5 (d, 4C, Ar), 79.9 (s, OCH$_2$-*C*≡CH), 74.3 (d, OCH$_2$-C≡*C*H), 69.4 (t, *C*H$_2$OCH$_2$-C≡CH), 68.2, 68.1 (t, 2C, ArO-*C*H$_2$-A), 65.3 (t, O*C*H$_2$-C≡CH), 58.1 (t, *C*H$_2$CO), 31.3 (t, 2C, aliphatic –CH$_2$-), 26.0, 25.3, 19.3 (t, 4C, aliphatic –CH$_2$-), 13.9 (q, 2C, Me) ppm; IR (KBr): 3265, 2958, 2873, 2124, 1713, 1699, 1512, 1421, 1252, 1162 cm^{-1}; MS (ESI) *m/z*: 639.0 ([M+Na]$^+$; 100); Anal. Calcd for $C_{36}H_{40}O_9$ (616.70): C 70.11, H 6.54; found C 69.88, H 6.82.

1-chloro-6-(prop-2-yn-1-yloxy)hexane (**21**). A solution of 6-chlorohexan-1-ol (5 g, 136.62 mmol) in DMF (15 mL) was added dropwise into a suspension of sodium hydride (60% w/w in mineral oil, 1.31 g, 54.9 mmol) in DMF (24 mL) at 0 °C. After being stirred for 30' at 0 °C, a solution of propargyl bromide (80% w/w in toluene, 6.53 g, 54.9 mmol) in DMF (10 mL) was added. The mixture was stirred for 18 h at room temperature the water was added (40 mL) and the product was extracted with AcOEt (50 mL x2). The organic phase was washed twice with water, dried over $MgSO_4$, filtered and concentrated under reduced pressure. The crude product was purified by FCC (hexane:AcOEt 5:1, R_f = 0.67) affording the desired product in 71 % yield (6.3 g, 49.2 mmol) as a yellow liquid. ^{1}H-NMR (400 MHz, $CDCl_3$) δ = 4.13 (d, *J* = 2.4 Hz, 2H, OC*H*$_2$-C≡CH), 3.64 (t, *J* = 5.8 Hz, 2H, C*H*$_2$OCH$_2$-C≡CH), 3.55 (t, *J* = 5.8 Hz, 2H, C*H*$_2$OH),2.56 (broad s, 1H, OH), 2.42 (t, *J* = 2.4 Hz, 1H, OCH$_2$-C≡C*H*), 1.70-1.62 (m, 4H, aliphatic -*CH*$_2$-) ppm.

methyl 4-((6-(prop-2-yn-1-yloxy)hexyl)oxy)benzoate (**22**). A solution of **21** (5.7 g,32.61 mmol), methyl 4-hydroxybenzoate (15 g, 97.847 mmol), K_2CO_3 (5.41 g, 39.132 mmol) and NaI (4.89 g, 32.61 mmol) in DMF (125 mL) was stirred for 18 h at 85 °C. Then, water was added (75 mL) and the product was extracted with Et_2O (100 mL x3). The organic phases were washed with water (500 mL x2), dried over Na_2SO_4, filtered and concentrate under reduced pressure, providing the pure product in 100% yield (9.5 g, 32.61 mmol). ^{1}H-NMR (200 MHz, $CDCl_3$) δ = 8.06-8.00 (m, 2H, Ar), 6.98-6.90 (m, 2H, Ar), (d, *J* = 2 Hz, 2H, OC*H*$_2$-C≡CH), 4.07 (t, J = 6 Hz, 2H, C*H*$_2$OCH$_2$-C≡CH), 3.95 (s, 3H, O-C*H*$_3$), 3.59 (t, J = 6Hz, 2H, Ar-O-*CH*$_2$-), 2.48 (t, J = 2Hz, 1H, OCH$_2$-C≡C*H*), 1.94-1.8 (m, 8H, aliphatic, -C*H*$_2$-).

4-((6-(prop-2-yn-1-yloxy)hexyl)oxy)benzoic acid (**Alk4**). A solution of **22** (8.00 g, 27.59 mmol) in methanol (100 mL) was stirred for 18 h at 50 °C in presence of KOH (5.417 g, 95.56 mmol). The methanol was evaporated under reduced pressure and water was added (50 mL), then the solution was acidified with HCl 1M until to pH 1. The precipitate was filtered and washed several times with water, dried and purified by FCC (EP:AcOEt 2:1 R*f* = 0.18) providing the pure product in 78% yield (5.94 g, 21.49 mmol). ^{1}H-NMR (200 MHz, $CDCl_3$) δ = 8.05 (d, *J* = 8 Hz, 2H, Ar), 6.92 (d, *J* = 10 Hz, 2H, Ar), 4.14 (d, *J* = 2 Hz, 2H, OC*H*$_2$-C≡CH), 4.02 (t, *J* = 8 Hz, 2H, Ar-O-C*H*$_2$-), 3.53 (t, J = 8 Hz, 2H, C*H*$_2$OCH$_2$-C≡CH), 2.42 (t, *J* = 2 Hz, 1H, OCH$_2$-C≡C*H*), 1.86-1.79 (m, 2H, aliphatic -*CH*$_2$-), 1.68-1.47 (m, 6H, aliphatic -*CH*$_2$-) ppm. ^{13}C NMR (50 MHz, $CDCl_3$) δ = 171.1 (C=O), 163.4 (s, Ar), 132.4 (s, 2C, Ar), 121.2 (s, Ar), 114 (s, 2C, Ar), 80 (s, -OCH$_2$*C*≡CH), 76.6 (s, -C≡*C*H), 74 (s, -*C*H$_2$-OCH$_2$C≡CH), 69 (s, ArO-*C*H$_2$), 58 (s, -O*C*H$_2$-C≡CH), 29.2, 28.8, 25.6 (aliphatic, -*C*H$_2$-). IR (KBr): 3294, 2943, 2856, 2667, 1687, 1606, 1255, 1172 cm^{-1}.

4-cyanophenyl 4-((6-(prop-2-yn-1-yloxy)hexyl)oxy)benzoate (**Alk2**). A solution of **Alk4** (300 mg, 1.08 mmol), DCC (224 mg, 1.08 mmol) and DMAP (14.6 mg, 0.12 mmol) in dry CH_2Cl_2 (12 mL) was stirred at room temperature under N_2 atmosphere. After 10 minutes, 4-hydroxybenzonitrile (130 mg, 1.08 mmol) was added under N_2 atmosphere and the mixture was stirred for 18 h at room temperature. The *N*,*N*-dicyclohexylurea was filtered and the filtrate was washed with water (30 mL), 5% acetic acid solution (30 mL) and water (30 mL). The organic layers were dried over Na_2SO_4, filtered and evaporated under reduced pressure. The crude material was recrystallized from ethanol affording the desired product in 54% yield (224 mg, 0.59 mmol) as a white solid. ^{1}H-NMR (200 MHz, $CDCl_3$) δ = 8.12 (d, *J* = 8 Hz, 2H, Ar), 7.73 (d, *J* = 8 Hz, 2H, Ar), 7.35 (d, *J* = 8 Hz, 2H, Ar), 6.97 (d, *J* = 10 Hz, 2H, Ar), 4.14 (d, J = 2 Hz, OC*H*$_2$-C≡CH), 4.05 (t, *J* = 8 Hz, 2H, Ar-O-C*H*$_2$-), 3.54 (t, *J* = 6, 2H, C*H*$_2$OCH$_2$-C≡CH), 2.42 (t, *J* = 2 Hz, 1H, OCH$_2$-C≡C*H*), 1.88-1.81 (m, 2H, aliphatic -*CH*$_2$-), 1.68-1.49 (m, 6H, aliphatic -*CH*$_2$-) ppm.

4-pentylphenyl 4-((6-(prop-2-yn-1-yloxy)hexyl)oxy)benzoate (**Alk5**). A solution of **Alk4** (300 mg, 1.08 mmol), DCC (224 mg, 1.08 mmol) and DMAP (14.6 mg, 0.12 mmol) in dry CH_2Cl_2 (12 mL) was stirred at room temperature under N_2 atmosphere. After 10 minutes, 4-pentylphenol (179 mg, 1.08 mmol) was added under N_2 atmosphere and the mixture was stirred for 18 h at room temperature. The *N*,*N*-dicyclohexylurea was filtered and the filtrate was washed with water (30 mL), 5% acetic acid solution (30 mL) and water (30 mL). The organic layers were dried over Na_2SO_4, filtered and evaporated under reduced pressure. The crude material was purified by FCC (EP:AcOEt 6:1 Rf = 0.61) affording the desired product in 69% yield (318 mg, 0.75 mmol) as colourless oil. ^{1}H-NMR (200 MHz, $CDCl_3$) δ = 8.13 (d, *J* = 8 Hz, 2H, Ar), 7.21 (d, *J* = 10 Hz, 2H, Ar), 7.15-7.07 (m, 2H, Ar), 7.00-6.94 (m, 2H, Ar), 4.14 (d, *J* = 2 Hz, OC*H*$_2$-C≡CH), 4.04 (t, *J* = 8 Hz, 2H, Ar-O-C*H*$_2$-), 3.54 (t, *J* = 6, 2H, C*H*$_2$OCH$_2$-C≡CH), 2.62 (t, *J* = 6 Hz, 2H, Ar-C*H*$_2$-), 2.42 (t, *J* = 2 Hz, 1H, OCH$_2$-C≡C*H*), 1.84 (t, *J* = 6 Hz, 2H, -C*H*2-Me), 1.65-1.25 (m, 4H, aliphatic -*CH*$_2$-), 0.90 (t, *J* = 6 Hz, 3H, Me) ppm.

4-methoxyphenyl 4-((6-(prop-2-yn-1-yloxy)hexyl)oxy)benzoate (**Alk3**). A solution of **Alk4** (500 mg, 1.80 mmol), DCC (373.25 mg, 1.80 mmol) and DMAP (24.31 mg, 0.12 mmol) in dry CH_2Cl_2 (18 mL) was stirred at room temperature under N_2 atmosphere. After 10 minutes, 4-methoxyphenol (225 mg, 1.80 mmol) was added under N_2 atmosphere and the mixture was stirred for 18 h at room temperature. The *N*,*N*-dicyclohexylurea was filtered and the filtrate was washed with water (50 mL), 5% acetic acid solution (50 mL) and water (50 mL). The organic layers were dried over Na_2SO_4,

filtered and evaporated under reduced pressure. The crude material was recrystallized from ethanol affording the desired product in 63% yield (441 mg, 1.15 mmol) as a white solid. ^{1}H-NMR (200 MHz, $CDCl_3$) δ = 8.13 (d, *J* = 8 Hz, 2H, Ar), 7.11 (d, *J* = 10 Hz, 2H, Ar), 6.98-6.91 (m, 4H, Ar), 4.14 (d, J = 2 Hz, OC*H*$_2$-C≡CH), 4.04 (t, *J* = 8 Hz, 2H, Ar-O-C*H*$_2$-), 3.54 (t, *J* = 6, 2H, C*H*$_2$OCH$_2$-C≡CH), 2.42 (t, *J* = 2 Hz, 1H, OCH$_2$-C≡C*H*), 1.87-1.77 (m, 2H, aliphatic -*CH*$_2$-), 1.68-1.49 (m, 6H, aliphatic -*CH*$_2$-) ppm; ^{13}C (50 MHz, $CDCl_3$) δ = 165.1 (C=O), 163.2 (s, Ar), 157 (s, Ar), 144.3 (s, Ar), 132 (s, 2C, Ar), 122.3 (s, 2C, Ar), 121.5 (s, Ar), 114.3 (s, 2C, Ar), 114 (s, 2C, Ar), 79.8 (s, *C*≡CH), 76.8 (d, OCH$_2$-C≡*C*H), 74 (s, -*C*H$_2$-O), 70 (ArO-*C*H$_2$), 68 (s, -O*C*H$_2$-C≡CH), 57.8 (s, -O*C*H$_3$), 29.2, 28.8, 25.6 (aliphatic -*C*H$_2$-) ppm; IR (KBr): 3265, 2951, 2850, 2372, 2312, 1730, 1610, 1512, 1269, 1199 cm^{-1}.

Fabrication of LCE Films.

Mixtures **LCE$_1$**, **LCE$_{1\text{-}1}$**, **LCE$_{1\text{-}3}$**, **LCE$_{1\text{-}4}$**, **LCE$_{2\text{-}1}$** and **Irgacure 389 IN1** (4% w/w in respect to the other monomers) were infiltrated in a glass rubbed cell with a 75 µm gap (Mylar) at the isotropic phase temperature of the mixture, reported in **Table 5**. The inner surfaces of the cell were spin-coated with PVA solution (0.5% in water for the glass down and 5% in water for the glass on the top), dried for 18 h and rubbed with a velvet cloth. After infiltration the cell was cooled down 2 °C/min to a temperature in which the mixture reaches the homogeneous alignment and then irradiated 1 hour with a UV lamp (ThorLabs M385CP1-C4, λ = 385 nm) and 30 minutes at 70 °C for **LCE$_{2\text{-}1}$** and 100 °C for the other mixtures. After polymerization, cell was leave in water for 24 h to facilitate the detach of the glass by the film; finally the film was gently peeled off.

Contraction experiments. Two pieces of each film, different in size, one cut 1 cm in length and 1 mm in width and the other one 1 cm in length and 3 mm in width, were put on a silicone oil drop on the top of a glass plate, then was heated to induce the isotropic phase (200 °C) and cooled down to room temperature. During the experiments a video sequence was recorded and then, the extrapolated frame, at the desired temperature value, was analysed with an image processing program (ImageJ) to measure the length with high precision.

Chapter 4 - Micro-patterned surfaces for cellular growth

4.1 Introduction

In this study we evaluated how human induced pluripotent stem cells-derived cardiomyocytes (hiPSC-CMs) can develop a functional differentiation on micro-patterned hydrogel substrates. The proposed methodology can be applied to model mechanistic hypothesis on disease progression and pharmacological interventions in patient-derived hiPSC.

Human induced pluripotent stem cells are cells generated through genetic reprogramming of somatic cells of healthy or unhealthy subjects. Since induced pluripotent stem cells are self-renewing and pluripotent, they represent an unlimited source of patient-derived cells, which can be turned into any type of tissue the body, preserving the genetic background of the patient. For our purpose, hiPSC were obtained by healthy subjects and then differentiated into cardiomyocytes to study *in vitro* functional and molecular mechanisms or modelling the cardiac pathology of these patients in-a-dish.

However, hiPSC-CMs have generally immature structure and function compared to native cardiomyocytes and resemble more closely features of developing cardiomyocytes [180]. For this reason, the use of biomimetic substrates able to impact cardiac maturation features, cell adaptiveness to extracellular cues and exacerbate disease-related mechanisms are needed. In our study we patterned microstructured surfaces by hydrogels, three-dimensional polymeric networks formed by crosslinking of hydrophilic polymeric chains. Thanks to their ability to absorb and retain water, hydrogels are often used in regenerative medicine and tissue engineering as scaffolds to allow cell attachment, growth and differentiation, by mimicking the *in vivo* physical environment [181]–[183]. Poly(ethylene glycol) (PEG)-based hydrogels were chosen as biocompatible material for this work for his favourable nonfouling character and tunable crosslink density [75], [184]. In particular, acrylate PEG derivatives can be photopolymerized to obtain hydrogels that may have complex shapes and microstructures [185], [186]. Furthermore, the stiffness (Young modulus) of the hydrogel-based surfaces was in the order of 100 kPa closely mimicking the physiological conditions of the human cardiac extracellular matrix [76].

To induce a physiological cellular organization *in vitro*, we used aligned hydrogel grooves, which can help to drive the functional differentiation of hiPSC-cardiomyocytes, taking in consideration later-stages of the maturation (60, 75 and 90 days post-differentiation) in which hiPSC respond to field stimulation at various pacing frequencies and to inotropic agents, likely resembling calcium handling features of human adult cardiomyocytes.

Finally, we studied how patterns at different rigidity, prepared using mixtures of PEG-DA and Diethylene glycol diacrylate (DEG-DA) at different percentage, can influence the functional response during the cellular maturation.

4.2 Results and discussion

4.2.1 Fabrication of hydrogel-based substrates by soft-lithography

In order to obtain the micropatterned surfaces we used soft-lithography by a PDMS mold, as described in Chapter 2.

A previous work, in which the patterns were realized in a polyurethane acrylate material, reported that the optimal geometry of the micro-grooves is of 1:1 groove width:ridge width ratio and groove/ridge widths of 800 nm based on hiPSC-CM myofibril (the subcellular contractile organelles) alignment and sarcomere length [69]. For this reason, we started fabricating micro-patterns with different size. The silica masters are obtained in two different ways. Two samples of silica were fabricated with RIE technique (Reactive Ion Etching) and the other one with MACE technique (Metal-Assisted Chemical Etching). In **Table 8** are reported the dimensions of the silica master used.

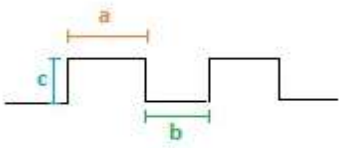

MACE Sample 9	RIE Sample 11	RIE Sample 13
a = 0.8 µm	a = 0.4 µm	a = 0.6 µm
b = 1.2 µm	b = 1.6 µm	b = 1.4 µm
c = 2.0 µm	c = 1.2 µm	c = 1.5 µm

Table 8 – Dimensions of the silica masters obtained with both technique (RIE and MACE)

To prevent the peeling-off of the PEG hydrogel by the glass slides, we treated the glass surfaces with a silanizing solution [187]. The slides were washed in a basic piranha solution (water, aqueous ammonia and hydrogen peroxide 5:1:1 v/v) and then immersed in a solution 0.032 mM of MAPTMS (3-(trimethoxysilyl)propyl methacrylate) in ethanol and dilute acetic acid (3:100 v/v). Subsequently, the photopolymerization of the hydrogel on the glass using the different PDMS masters allowed to obtain the structures showed in **Figure 67**.

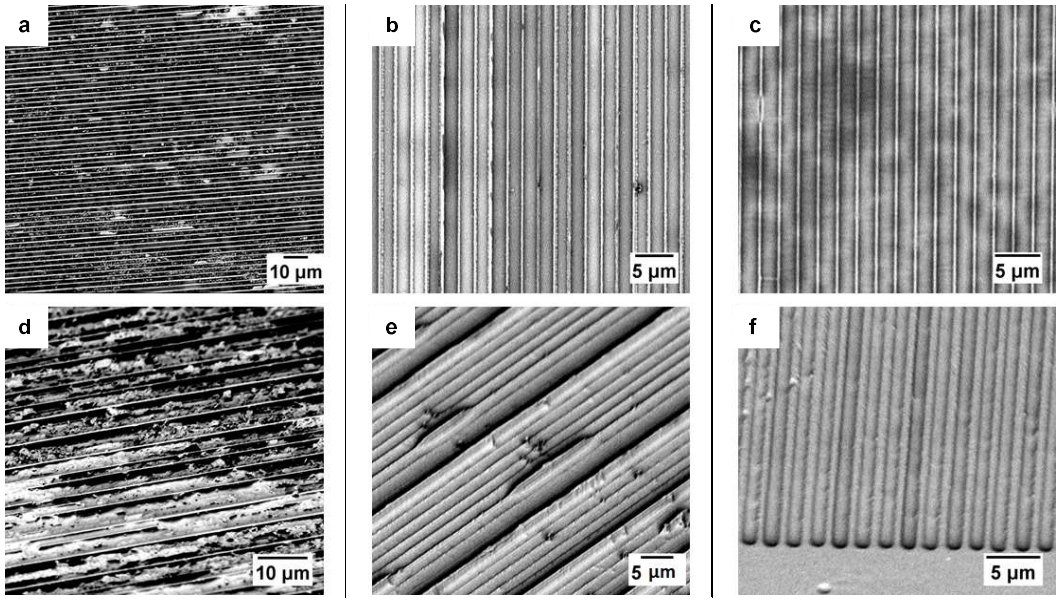

Figure 67 – SEM pictures of silica masters and polymerized hydrogels for sample9 (a and d), sample 11 (b and **e)** and **sample 13 (c** and **f).**

SEM pictures demonstrate as the silica master obtained with MACE technique is not homogeneous, and the hydrogel pattern fabricated with this sample is affected by many defects (**Figure 67a** and **d**). The silica masters obtained with RIE technique are more homogeneous (**Figure 67 b** and **c**), but hydrogel patterns obtained with sample 11 are not regular (**Figure 67e**). For this reason, we choose to perform the biological characterization using only silica sample 13 as master and the relative PDMS master fabricated starting from it.

4.2.2 Biological experiments

The biological experiments were performed in the laboratory of Dr. Raffaele Coppini and Dr. Cecilia Ferrantini of the University of Florence. In this paragraph will be briefly show the results obtained in this collaboration.

In order to evaluate the functional differentiation of the hiPSC-CMs on PEG-based micro-patterned surfaces, action potential (AP) and calcium transients (CaT) were simultaneous optical recorded [188] at specific time points in later stages hiPSC-CMs (day 60, 75 and 90 post differentiation) cultured on biomimetic substrates with micropatterned topography and physiological stiffness in the range of kPa. We performed simultaneous recordings of action potential (AP) and calcium transients (CaT) with fluorescent indicators at single cell level.

4.2.2.1 Evaluation of the action potential (AP) at different time points

The quantification of the action potential was measured by acquiring the voltage-sensitive fluorescent dye (Fluovolt, Ex/em 522/535 nm) signal at day (d) 75 and 90 (**Figure 68a**). At day 75,

AP duration (APD) did not show a significant rate adaptation (APD50 at 1 and 2 Hz were comparable). At day 90, instead, APD50 was shortened at 2 Hz compared to 1 Hz, highlighting that mature hiPSC-CMs acquired a typical rate-dependent APD adaptation (**Figure 68b**).

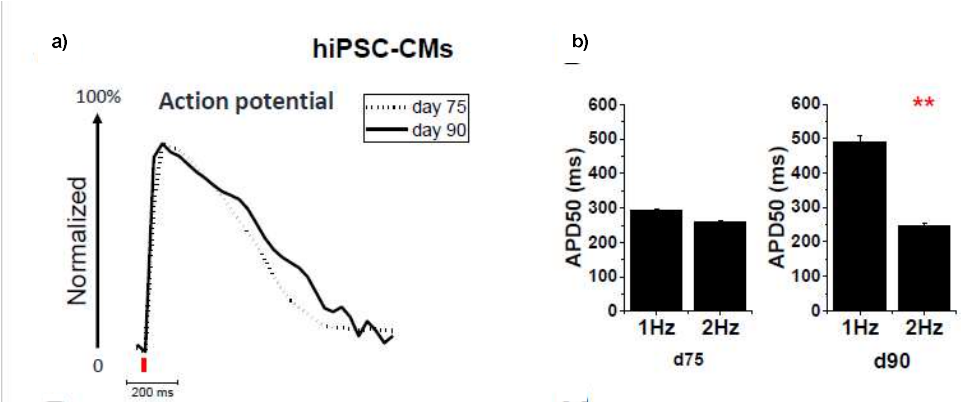

Figure 68 – Single hiPSC-CMs matured on hydrogel-based micropatterned surfaces were subjected to optical measurements of action potentials. a) AP traces of day 75 vs. day 90**. b)** AP profile recorded both at 1 and 2 Hz to evaluate APD50 (ms) and the response to frequency changes at both day 75 and 90.

4.2.2.2 Evaluation of Calcium Transient (CaT) at different time points

Calcium transients were measured simultaneously with AP using Cal630 (Ex/Em 608/626 nm), at each time point. At both 1 and 2 Hz, the kinetics of calcium rise (time to peak, TTP) and decay (ratio between TTP and time to 50% of CaT decay, RT50) became more rapid with maturation (**Figure 69a**). Calcium transient amplitude was similar at day 60 and 75, but it increased by 50% at d90 (**Figure 69b**).

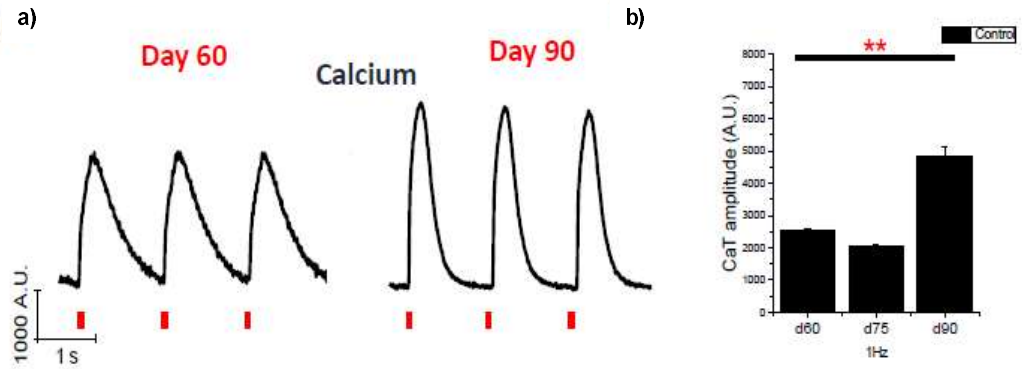

Figure 69 – Representative CaT profiles at day 60 and 90 and average CaT amplitude at day 60, 75 and 90.

4.2.2.3 Evaluation of Sarcoplasmic Reticulum Contribution to Calcium Handling

The sarcoplasmic reticulum (SR) is the main store of calcium in cardiomyocytes and his contribution was measured using two different protocol.

- Evaluation of the calcium transient potentiation after a stimulation pause. hiPSC-CMs were paced at 2 Hz and, following a stimulation pause of 5 s, the amplitude of the first CaT after stimulation is resumed, and the pause was measured to evaluate the rest-mediated potentiation. If, during the pause, the content of calcium is stored in the reticulum, after application of a new stimulus, the potentiation of the first calcium transient after the stimulus reflects the contribution of the sarcoplasmic reticulum compared to the contribution of the extracellular calcium. CaT amplitude after the rest pause displayed a modest potentiation over the amplitude before the pause at day 60. However, the amplitude of post-rest CaTs almost doubled at day 90, suggesting increased SR loading capacity during maturation (**Figure 70**).

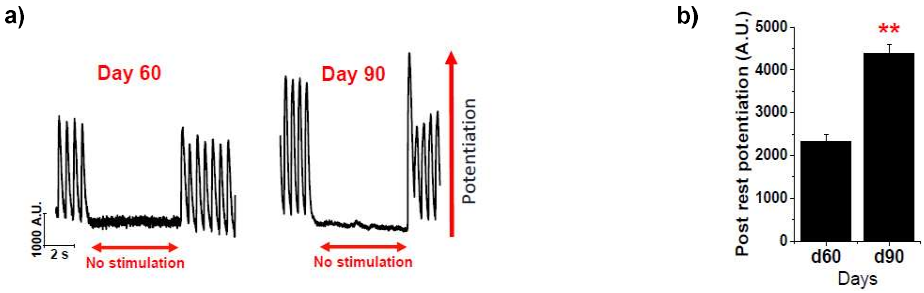

Figure 70 – Sarcoplasmatic reticulum contribution during hiPSC-CM maturation. a) the post-rest potentiation of CaT amplitude expressed as the % increase of CaT amplitude**.**

- Direct evaluation of the calcium transient potentiation measuring caffeine-induced calcium transient (quick exposure to 10 µM caffeine) after a pacing train of 2 Hz. In day 60, the relative caffeine-induced CaT amplitude was higher compared to that of hAdult-CMs (**Figure 71**).

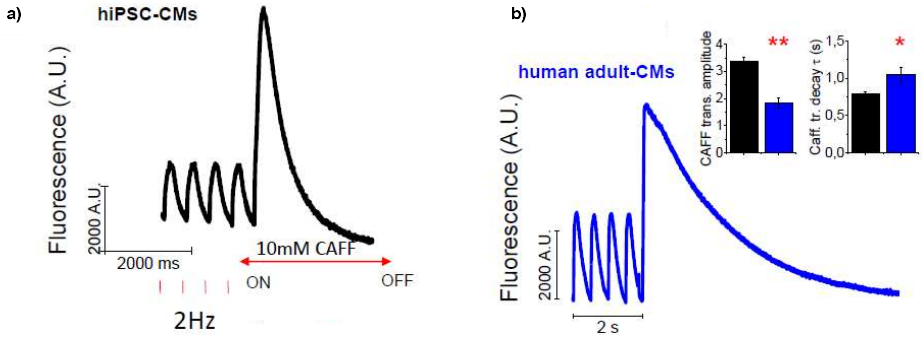

Figure 71 – Sarcoplasmatic reticulum contribution during hiPSC-CM maturation tested by caffeine-induced CaTs.

These results indicate a significant contribution of calcium release from the SR to the amplitude of calcium transients starting from day 60 and suggest that the enhanced SR calcium load is the main determinant of the progressive increase of CaT amplitude of hiPSC-CMs from day 60 to day 90.

4.2.2.4 Evaluation of Membrane Potential and Spontaneous Action Potential of Earlier-Stage hiPSC-CMs

To support the previous results, we measured APs in early-stage hiPSC-CMS (day 20, 30, 60 post differentiation), during stimulation with short current pulses in the current-clamp configuration at different frequencies (0.5-1-2 Hz, **Figure 72**).

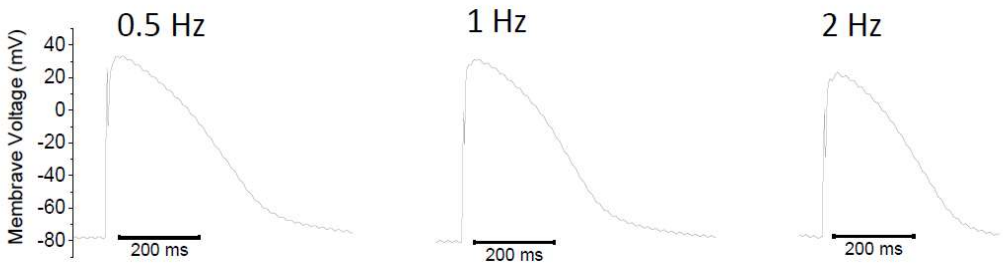

Figure 72 – Action potential recording by patch clamp in earlier stages hiPSC-CMs.

Figure 73 shows that, compared to the earliest-stage (d20), hiPSC-CMs at later stages of maturation showed progressively more negative resting membrane potentials (RMP, mV, **Figure 73a**), larger AP amplitude (mV, **Figure 73b**) and prolongation of AP duration (ADP_{50}, **Figure 73c**).

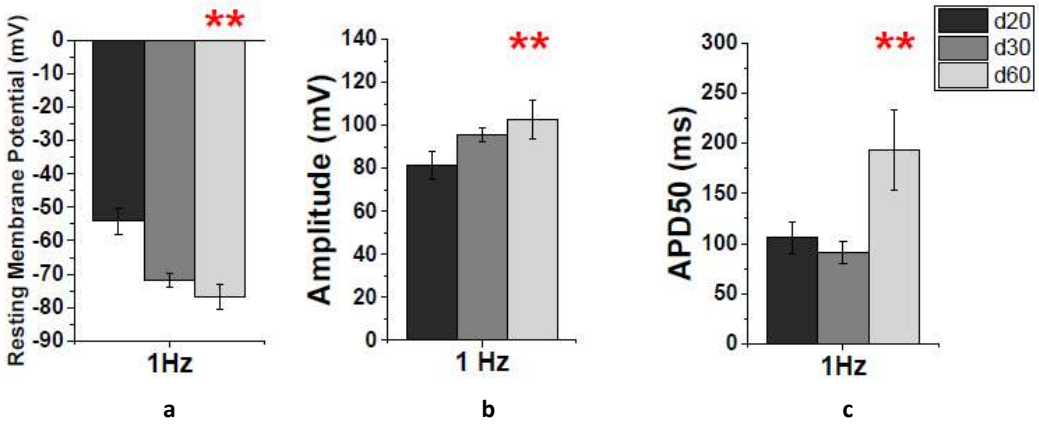

Figure 73 - Average of resting membrane potential (mV), AP amplitude (mV), time from stimulus to 50% repolarization (APD50, ms)

Notably, spontaneous beating frequency, measured in patched cells without stimulation, showed a progressive reduction from day 20 to 60 post differentiation (**Figure 74**). Of note, mature hiPSC-CMs (from day 60) do not show a significant spontaneous beating activity.

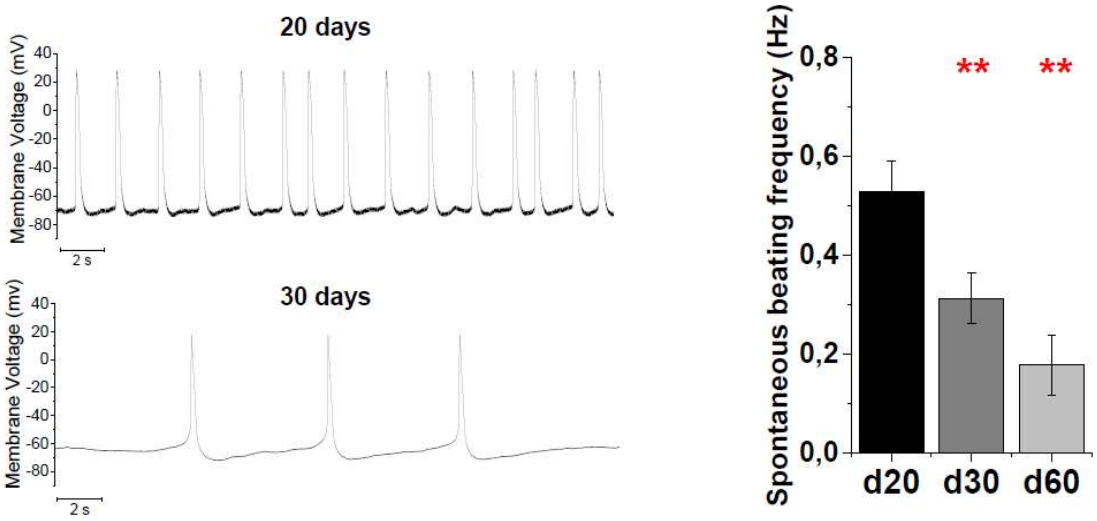

Figure 74 - Spontaneous beating frequency of action potential from day 20 to day 60.

4.2.2.5 Effects of micro-topographic pattern on sarcomere development

Finally, images of hiPSC-CMs were used to evaluate the sarcomere length within cells cultured on micro-patterned surfaces (**Figure 75**). Sarcomere length is directly related to force production from cell contractions [189], [190], and can be correlated to the Frank-Starling law on the nanoscale [191]. It has been reported that adult cardiomyocytes have sarcomere lengths in the region of 1.8-2.0 µm, whereas immature human pluripotent stem cell-derived cardiomyocytes often have sarcomere lengths of approximately 1.5 µm [74], [192].

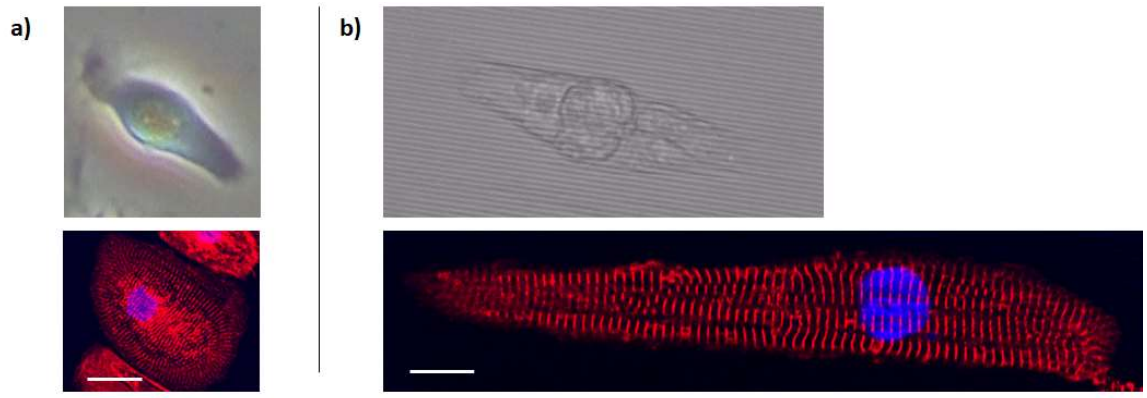

Figure 75 – Optical images (top panel) and confocal images (bottom panel) of hiPSC-cardiomyocytes cultured a) on Petri dish and **b)** on hydrogel-based micro-patterned substrates. Scale bar: 20 µm.

In **Figure 75** are reported the optical pictures of a single hiPSC-CMs cultured on a Petri dish (**Figure 75a**) and on hydrogel-based micro-patterned substrates (**Figure 75b**). The elongated shape of the cell grew up on the patterned substrate is well visible in the immunostained images, shown in **Figure75** (bottom). The red coloration (α-actinin) indicates the Z lines of the sarcomere (contractile unit) and in blue is coloured the nucleus.

The sarcomere length of cells on patterned substrates was 1.8 µm, which is substantial increase in length compared to other studies on hiPSC-CMs of a similar age (1.65 µm).

4.2.3 Relation between the rigidity of the substrate and maturation of the cardiomyocyte activity

The reticulation density of the polymer can be modified for tuning the mechanical properties of the final material. The introduction of higher rigidity is a consequence of an increment of reticulation of the system, allowing to obtain also a decrease of the swelling phenomena.

In order to obtain pattern with different rigidity, we mixed PEG-DA (250 Mn) with DEG-DA (diethylene glycol diacrylate), a monomer characterized by shorter carbon chains than PEG-DA. Increasing the concentration of DEG-DA, we can increase the reticulation density of the polymer and hence the micro-structured substrates are characterized by a higher rigidity.

We prepared three different mixtures in the following way:

- **MixA**: obtained with 25% of PEG-DA and 75% of DEG-DA
- **MixB**: obtained with 50% of DEG-DA and 50% of PEG-DA
- **MixC**: obtained with 75% of PEG-DA and 25% of DEG-DA

4.1.1.1 Biological test on hydrogel-based micro-patterned surface with different rigidity

In the same way explained before, we tested the same cellular line, on hydrogel-based micropatterned substrates obtained with different rigidity and preliminary results are shown in **Figure 76**.

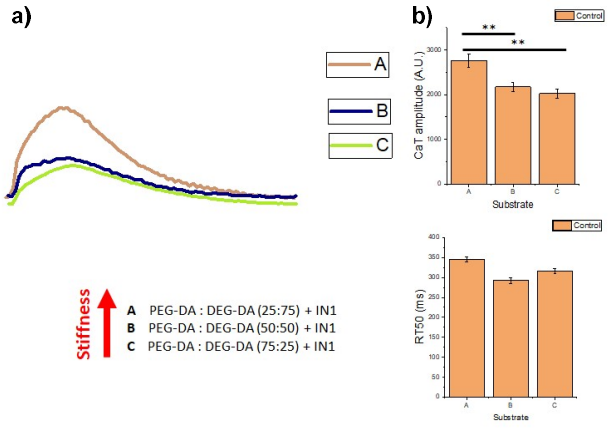

Figure 76 – Action potential of hiPSC-cardiomyocytes cultured on nano-topographic substrates at different rigidity.

In **Figure 76a**, the action potentials of the cells cultivated on the patterned substrates with different rigidity (A, B and C) are showed. The tests show an increase of the action potential as the rigidity of the substrate increase. Substrate A, characterized by a high rigidity, shows higher AP

behaviours, highlighting as changing the chemical composition of the patterned hydrogels influences the functional maturation of the selected cellular lines.

These biomimetic substrate with micropatterned topography and tunable stiffness can be applied to study different hiPSC-CM disease. At the moment, our materials are employed towards physiophatological studies on Duchenne Muscular Dystrophy (DMD) patient-derived cell lines. In this disease, the absence of dystrophin, a protein working as “shocking adsober” in the patient muscles (including the heart) leads to a severe cardiac dysfutncion. The impact of substrate stiffness in DMD-hiPSC-CMs is currently under investigation.

4.3 Experimental part

Materials and methods.

Fabrication of micro-patterned surfaces

Micro-patterned substrates were prepared by soft lithographic technique. A master sample was replicated by a PDMS (polydimethylsiloxane) (Sylgard 184, Sigma-Aldrich) mold that is used as template for the pattern replication.

Master fabrication – Master samples was bought by a company (JD Photo Data) which provided to fabricate silicon master using UV lithography. A UV photomask is made from a transparent material, typically fused silica, on which a pattern is defined in an absorbing thin film such as chromium. The photomask is brought into proximity or even contact with the resist coated substrate using a dedicated exposure system. The substrate is then exposed through the photomask by a UV light source (Hg-lamp with an i-line notch filter that gives a typical UV source with a wavelength of 365 nm). After exposure the substrate is developed, and the pattern is formed.

Fabrication of PDMS mold – Monomeric PDMS mixture was prepared by mixing the two components of a commercially available PDMS kit in a 10:1 w/w ratio (base and curing agent) and then casted on the silicon master. After curing at 100° C for 30 minutes, the crosslinked PDMS mold was peeled off by the master.

Master fabrication – Master samples was obtained by laser writer lithography (Heidelberg µPG101 laser writer, 800 nm resolution). A commercial optical resist (AZ 1505 Merck Performance Materials GmbH) was spun over 2 cm x 2 cm Si wafers and exposed to a laser spot (λ = 375 nm) with beam intensity of 16 mW. The length of the linear stripes was set to 1 cm, while their width and spacing were fixed to 1 µm. After exposure process, the samples were developed for 30 s in a 1:1 solution of AZ Developer (Merck Performance Materials GmbH) in water, and subsequently rinsed in deionized water for 120 s.

Glass slides treatment – Glasses to support the PEG patterns were silanized to prevent the peeling-off of the hydrogel during the cell culture. First, glasses were washed with an alkaline piranha solution (water, aqueous ammonia and hydrogen peroxide 5:1:1 v/v) at 70° C for 15 minutes. Then, the glasses were rinsed with water and the isopropyl alcohol and, after drying, they were

immersed in a solution of MAPTMS (3-(trimethoxysilyl)propyl methacrylate) (Sigma Aldrich) 0,064 mM in ethanol for 1 hour. At the end, glasses were washed with isopropanol and dried.

PEG-DA pattern printing- A small amount (~20 µL) of a solution of PEG-DA (250 Mn, Sigma Aldrich) and photoinitiator Irgacure 389 (1% w/w) was dropped on a silanized glass slides and then, the PDMS mold was directly placed onto the surface. Irradiation by UV light (ThorLabs M385CP1-C4, λ = 385 nm) for 10 minutes allowed the formation of the crosslinked PEG-DA network. PDMS mold was gently peeled off from the substrates and used again after washing in water and methanol. Images of mold and micropatterned PEG-DA hydrogels were obtained by scanning electron microscopy (SEM).

The following biological experiments were performed in the laboratory of Dr. Raffaele Coppini and Dr. Cecilia Ferrantini of the University of Florence:

Tissue processing and cell isolation

Surgical septal specimens from patients (hAdult-CMs) were washed with standard cardioplegic solution and processed within 30 min from excision. Ventricular tissue was minced and subjected to enzymatic dissociation to obtain viable single myocytes, as previously described [193], [194].

Maturation on PEG-DA hydrogel with nanopatterned topography

Single hiPSC-CMs are obtained from beating monolayers by 10 minutes of cell dissociation with Tryple (Life Technologies). Plating media is composed by RPMI/B27 and 10µM ROCK inhibitor. Cells are seeded at the density of 20,000 cells/cm2 onto biomimetic substrates and fed every other day until experimental days. Dual recording experiments of long-term cultured hiPSC-CMs were performed at day 60, 75 and 90. For patch clamp recordings, hiPSC-CMs were used at day 15, 30 and 60 from cardiac induction.

Dual recording of action potential and calcium transient

For dual recording hiPSC-CMs were loaded with 2µl/ml Fluovolt (Thermo Fisher), 2µl of Cal630 (AAT Bioquest) and 5µl of Power LoadTM (Thermo Fisher) for 30min at 37°C and then washed with pre-warmed culture media before placing the cover slide into the experimental chamber. The experimental chamber features platinum electrodes for electrical field stimulation, connected to a stimulator (DigiTimer, UK) delivering short (3ms) voltage pulses. During measurements, cells were continuously perfused with heated Tyrode buffer to keep the temperature at 37°C. For

fluorescence studies, cells were simultaneously illuminated by LED light at 2 different wavelengths, blue (488nm) for excitation of Fluovolt and yellow (580nm) for Cal630 dye excitation, using a multi-led system (Lumencor SPECTRA X). A dual-wavelenght band-pass filter cube (Semrock) was used to allow fluorescence light from the two dyes to be collected by a single camera (Photometrics Prime sCMOS): in particular, the filter allowed green light (515-545 nm, emission of Fluovolt) and red light (615-655 nm, emission of Cal630) to be collected. In order to separate the two emission wavelengths, we used a Cairn OptoSplit II light splitter that was able to separate the two spectral components of the fluorescence image and focus them simultaneously on the upper and lower half of the camera chip. Molecular Devices MetaMorph software was used to collect and analyse fluorescence images. The camera collected images at an average rate of 90 frames per second. In each studies cell field, a number of single hiPSC-CMs were selected and chosen as regions of interest. The background-corrected average fluorescence values from the pixels in each selected region of interest (myocyte) were recorded at each of the two wavelengths under different stimulation conditions. For the analysis of action potential or calcium transient kinetics during steady-state stimulation, the average of 5-10 subsequent AP or CaT traces was calculated to reduce noise. Pearson's correlation coefficient (r2) was calculated from the linear fitting of values distribution recorded from individual cells.

Perforated patch clamp and calcium transient recording

For cardiomyocytes isolated from patient ventricular tissue were simultaneously measured for membrane potential and calcium transients with perforated patch whole-cell current-clamp Ca^{2}+ sensitive fluorescent dye Fluoforte (Enzo Life Sciences, Farmingdale, NY, USA) respectively, as previously described [193], by measuring fluorescence at 515 ± 10 nm during excitation at 490 ± 8 nm. For hiPSC-CMs, the pipette solution contained (in $\times 10^{-3}$ M) 115 K methanesulfonate, 25 KCl, 10 (4-(2-hydroxyethyl)-1-piperazineethanesulfonic acid) (HEPES), 3 $MgCl_2$, and cells were perfused with Tyrode buffer containing 1.8×10^{-3} M $CaCl_2$. APs were elicited with short depolarizing stimuli (<3 ms) at 1 Hz of stimulation frequency. Action potentials were analysed for MDP (mV), amplitude (mV), and action potential duration (ADP50 and APD90, ms) using the Clampfit 10.7 software (Molecular devices).

Statistics

All data are reported in means ± SEM and were compared using a one-way or two-way analysis of variance (ANOVA) with a Tukey post hoc test with statistical significance set at P<0.05* and P< 0.01** were applied for differences in means between groups/conditions. The interquartile range

test was performed for data distribution and selection. For each analysis, n represented number of cardiomyocytes and N the total number of cell differentiation runs (N) from individual hiPSC passages (p) or individual patients. For this work healthy cell line had N=3-5. The number of individual experiments (individual coverslides) for each assessment was at least 2 from different differentiation runs.

Chapter 5 – Conclusions

This thesis focuses on the preparation and characterization of different microstructured and responsive surfaces. Different approaches to tailor the chemical-physical properties of a substrate are presented towards various application, such as to modulate surface wettability (from superhydrophobic to superhydrophilic) or to allow the maturation of cardiomyocytes with mature biological functions. on hydrogel-based micro-patterned surfaces.
In both cases, photopolymerization of different acrylate based monomers (liquid crystalline elastomers or hydrogel) was employed in combination with soft lithography to shape the material surface with a micro-structured fashion.

In Chapter 2, we focused the attention on self-cleaning applications towards engineering micro-structured surfaces with dynamic properties controlled by light. Several geometries have been tested with two different LC materials, demonstrating how to tune the water contact angle from 80° to 130° only by playing on the material topography, while surface adhesion can be tailored by silanization procedure to achieve water repellent surfaces.
To obtain a dynamic control on the wettability, we hypothesized that a light controlled reshaping of the microstructures could led to variation in the water contact angle. However, our experimental procedure did not allow the achievement of the homogeneous homeotropic LC alignment along the long axis of each microstructures (which is mandatory for big deformation) and the resulting wettability variation resulted poor. New procedures to obtain better LC alignment or the use of more responsive material are under evaluation to enhance the dynamic control on the surfaces.
In Chapter 3, thiol-yne click reaction was explored as a new and non-conventional methodology for the fabrication of LCEs characterized by mixed main-chain/side-chain architecture. This molecular arrangement was demonstrated able to support bigger deformations under thermal stimuli with respect to standard polyacrylate LCEs (previously used also in this thesis). A small library of thiols and alkynes was synthesized and mixed to fabricate polymeric actuator with different actuation under heating. Differential Scanning Calorimetry (DSC) analysis was used to reveal as changing mesogenic cores inside the main-chain is an efficient strategy to modulate the transition temperatures of the final materials (with clearing temperature around 150 °C for core with three aromatic rings and 80 °C for those with two rings).
On the other hand, polymers containing three-aromatic ring cores showed bigger extent in deformation (until 41% of the initial length) with respect to polymer containing two aromatic rings core (16%). Very interestingly, the different temperature range for the thermal contraction of different materials could be exploited to produce actuators composed by parts that respond in a

selective way in different environment (e.g. at the variation in temperature). Insertion of azobenzene dyes also in these polymers and their use to prepare micropatterned substrate are under evaluation in our laboratories.

In Chapter 4, soft-lithography was explored to realize micro-patterned substrates for the maturation and differentiation of specific cellular lines. In particular, we structured poly(ethylene glycol) (PEG) hydrogel into micro-grooves with controlled geometry (1.5 µm height and 0.6 µm width with a distance between a lone pair of lines of 1.4 µm) and we tested their performance as substrate for human induced pluripotent stem cells-derived cardiomyocytes (hiPSC-CMs) culture. This cell line is commonly used for *in vitro* studies to understand the molecular mechanisms of rare genetic diseases leading to different cardiomyopathies, towards new diagnostic and therapeutic approaches. Our materials have been demonstrated able to drive the right maturation, in terms of cellular shape and functionalities, of these cells improving their functionalities with respect to cells cultured on other commercial substrates. Action potential (AP) and calcium transients (CaT) characterizations allowed to demonstrate a cellular like-adult behaviour after 60 days of culture, improving the cellular functional maturation until 90 days. Also the morphology characterization, monitored with the sarcomere length of the cells, confirmed the previous functional characterization. Thanks to an ongoing collaboration, the above described substrates are currently under evaluation for the modelling of the Duchenne dystrophy by group of Dr. Cecilia Ferrantini and Prof. Corrado Poggesi at the Department of experimental and clinical medicine, division of physiology, of the University of Florence .

Appendix

Characterization techniques for Liquid Crystalline Elastomers properties

Polarized Optical Microscopy (POM)

Identification of LC behavior can be obtained by Polarized Optical Microscopy (POM) is a standard tool in the identification of liquid crystal phases and phase transitions. The optical texture which appears by observing an anisotropic material between two polarizers, crossed at 90° to each other, gives information relating to the arrangement of the molecules within the medium. The texture depends on the structural defects of the LC phase and it provides a valuable diagnostic tool for the identification of mesophase type.

When the sample has isotropic properties, the polarized light has its polarization direction either parallel or perpendicular to the director, and it will appear black under crossed polarizers. Since LC are anisotropic, they cause light polarized along the director to propagate at a different velocity than that polarized perpendicular to the director, then the LC might appear bright under crossed polarizers. The polarization of light is rotated by the LC molecules and allows to see optical textures which give information about the arrangement of the molecules within the medium. The textures depend by the structural defects of the LC phase and it provides a valuable diagnostic tool for the identification of mesophase type. In **Figure 77**, different examples of nematic phase images are reported. Typical *Schlieren* texture with two and four brushes defects is characteristic of this mesophase. In **Figure77a**, the POM image of a real mixture (**Mix1** described in Chapter 2 and used in this work for the preparation of micro-pillars for photoresponsive hydrophobic surfaces) shows the characteristic defects. In **Figure77b**, the schematic representation of the molecular order of two and four brushes defects is shown.

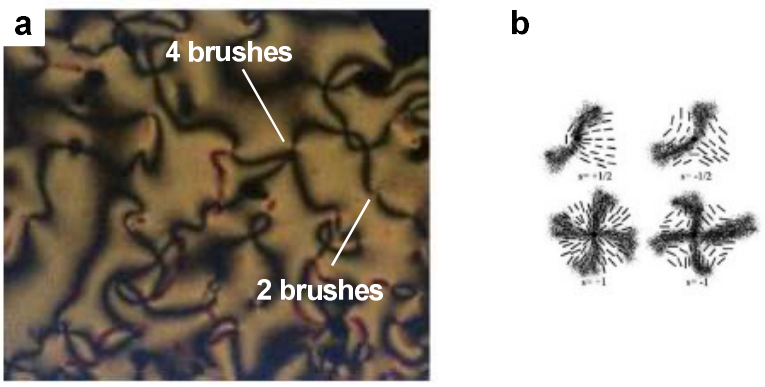

Figure 77 – Two examples of POM fo nematics a) POM picture of a nematic mesophase in which two and four brushes defects are well visible **b)** schematic representation of two and four brushes defects.

Differential Scanning Calorimetry (DSC)

Differential Scanning Calorimetry (DSC) measures the heat capacity of a material as a function of temperature with reference to a standard and it is a helpful technique which complements the optical methods in determining the liquid crystal phase transitions. In the simplest definition, a transition from one phase to another one is the transformation of one thermodynamic system of matter to another.

In **Figure 78** a DSC thermogram of molecule **Alk4**, synthetized during this thesis work, is shown. The DSC trace show both *enantiotropic* and *monotropic* phase transitions. The first one occurs above the melting point, such that the phases involved are thermodynamically stable (**Figure 78**, peak at 111 °C). The second two, occurs below the melting point, where at least one of the phases exists only at temperatures below the melting point and it is revealed by supercooling of the material (**Figure 78**, peak at 88.5 °C). By this graph is not possible identify the type of LC phase, the value of the enthalpy variation gives some information about the degree of the molecular order. Usually, the variation in enthalpy associates to the melting transition from a crystalline solid (**Cr**) to **LC** phase is around from 30 to 50 $kJmol^{-1}$. While, transition phases between different **LC** phases or from **LC** to **I** phases are characterized by a smaller enthalpy variation. For example, the transition phase from **SmA** to **I** involves an enthalpy variation between 4 and 6 $kJmol^{-1}$ and **N** to **I** transition involves just 1-2 $kJmol^{-1}$.

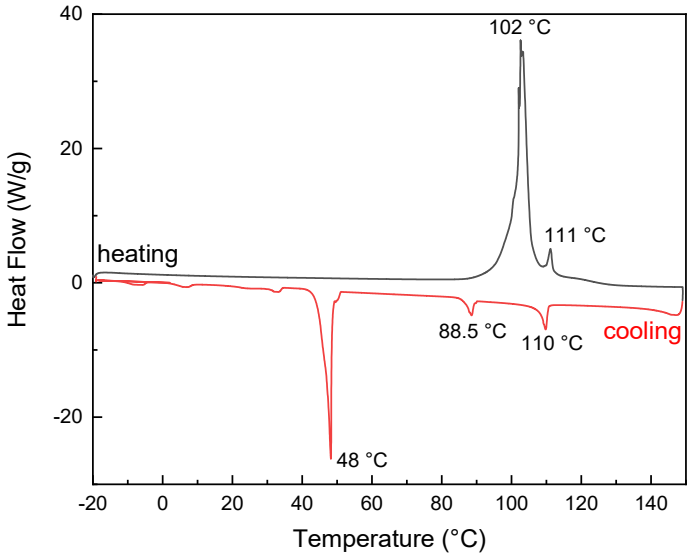

Figure 78 - Schematic of a differential scanning thermogram for a material that exhibits two enantiotropic mesophases and one monotropic mesophase

Dynamic Mechanical Analysis (DMA)

Regarding the mechanical properties of the polymers, Dynamic Mechanical Analysis (DMA), is the common technique used for this purpose. Since polymers respond to the energy of motion in two ways, with an elastic response (for shape recovery) and with a viscous response (for dispersing mechanical energy and preventing breakage), DMA is used for study the viscoelastic properties, of the polymers, under applications of low mechanical force.

Polymer viscoelasticity is dependent on temperature and time; hence these measurements are performed with a controlled heating and cooling to study temperature effects on polymer stiffness and test speed are used for mechanically deforming the polymer and study the time (or frequency) effects on resistance to permanent deformation. DMA utilizes a system of clamps which are based on giving the most suitable type of mechanical motion for the specific study type: tension (stretching), compression (push), flexure (bending) and shear (motion parallel to the sample surface). In standard use the basic operation of the DMA involves the application of a sinusoidally varying stress to a sample and the monitoring of the resulting deformation. In a temperature sweep DMA test, in which the modulus is plotted in function of variation in temperature. A thermoplastic polymer, during the heating, undergo a phase transition and lose its original elasticity, becoming fluid. This behavior is known as glass transition temperature (T_g) and, in DMA, this state is where the viscous response predominates.

The relationship between the strain (sinusoidal curve of the sample) and the stress (sinusoidal curve of the response measured by DMA) is derived and produce three quantifiable properties.

- **E' = Storage Modulus**
- **E'' = Loss Modulus**
- **E''/E' = tan δ**

Storage modulus is relative to the mechanical energy stored by the sample during the loading cycle, ad a consequence, it is related to the stiffness and shape recovery. The loss modulus indicates the polymer ability to disperse the mechanical energy through internal molecular motions. Tan delta peak measures the midpoint between the glassy and rubbery states. In **Figure 79** is reported an example of DMA measurement, in which E', E'' and tan δ are plotted in respect of variation in temperature in the same graph.

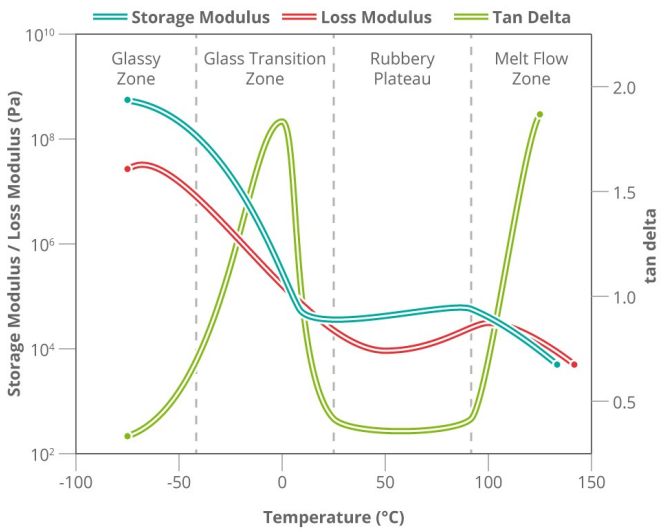

Figure 79 – DMA graphs in which the storage modulus (E'), loss modulus (E'') and tan delta are plotted.

At low temperatures, the sample presents a glassy nature, in which the values of E' and E'' are differentiate of about one order of magnitude. Heating gradually the sample, E' and E'' are matched in the glass transition zone (**Figure 79**, line blue and red), where the tan delta value shows the maximum peak (**Figure 79**, line green). After the T_g transition, a rubbery plateau occurs, indicating that the sample shows softer properties.

References

[1] T. G. Polefka, R. J. Bianchini, and S. Shapiro, “Interaction of mineral salts with the skin: A literature survey,” *International Journal of Cosmetic Science*. 2012.

[2] S. H. Park, S. Lee, D. Moreira, P. R. Bandaru, I. Han, and D. J. Yun, “Bioinspired superhydrophobic surfaces, fabricated through simple and scalable roll-to-roll processing,” *Sci. Rep.*, 2015.

[3] H. Zhou, H. Wang, H. Niu, A. Gestos, X. Wang, and T. Lin, “Fluoroalkyl silane modified silicone rubber/nanoparticle composite: A super durable, robust superhydrophobic fabric coating,” *Adv. Mater.*, 2012.

[4] H. Wang, Y. Xue, J. Ding, L. Feng, X. Wang, and T. Lin, “Durable, self-healing superhydrophobic and superoleophobic surfaces from fluorinated-decyl polyhedral oligomeric silsesquioxane and hydrolyzed fluorinated alkyl silane,” *Angew. Chemie - Int. Ed.*, 2011.

[5] H. H. Ipekci, H. H. Arkaz, M. S. Onses, and M. Hancer, “Superhydrophobic coatings with improved mechanical robustness based on polymer brushes,” *Surf. Coatings Technol.*, 2016.

[6] A. K. Mondal and K. Bansal, “A brief history and future aspects in automatic cleaning systems for solar photovoltaic panels,” *Adv. Robot.*, 2015.

[7] H. Wu *et al.*, “Biomimetic nanofiber patterns with controlled wettability,” *Soft Matter*, 2008.

[8] T. Sun, L. Feng, X. Gao, and L. Jiang, “Bioinspired surfaces with special wettability,” *Accounts of Chemical Research*. 2005.

[9] P. Gould, “Smart, clean surfaces,” *Mater. Today*, 2003.

[10] D. Liu, C. W. M. Bastiaansen, J. M. J. Den Toonder, and D. J. Broer, “Photo-switchable surface topologies in chiral nematic coatings,” *Angew. Chemie - Int. Ed.*, 2012.

[11] V. A. Ganesh, H. K. Raut, A. S. Nair, and S. Ramakrishna, “A review on self-cleaning coatings,” *Journal of Materials Chemistry*. 2011.

[12] J. N. Israelachvili, *Intermolecular and Surface Forces: Third Edition*. 2011.

[13] a W. Adamson and a P. Gast, *Physical Chemistry of Surfaces Sixth Edition*. 1997.

[14] K. Koch, B. Bhushan, and W. Barthlott, “Diversity of structure, morphology and wetting of plant surfaces,” *Soft Matter*, 2008.

[15] K. Koch and W. Barthlott, “Superhydrophobic and superhydrophilic plant surfaces: An inspiration for biomimetic materials,” *Philos. Trans. R. Soc. A Math. Phys. Eng. Sci.*, 2009.

[16] A. Milionis *et al.*, "Spatially controlled surface energy traps on superhydrophobic surfaces," *ACS Appl. Mater. Interfaces*, 2014.

[17] D. Wu *et al.*, "Curvature-driven reversible in situ switching between pinned and roll-down superhydrophobic states for water droplet transportation," *Adv. Mater.*, 2011.

[18] Y. Lai, X. Gao, H. Zhuang, J. Huang, C. Lin, and L. Jiang, "Designing superhydrophobic porous nanostructures with tunable water adhesion," *Adv. Mater.*, 2009.

[19] J. Yong *et al.*, "A simple way to achieve superhydrophobicity, controllable water adhesion, anisotropic sliding, and anisotropic wetting based on femtosecond-laser-induced line-patterned surfaces," *J. Mater. Chem. A*, 2014.

[20] J. Zhang, J. Li, and Y. Han, "Superhydrophobic PTFE surfaces by extension," *Macromol. Rapid Commun.*, 2004.

[21] N. Luo, A. T. Metters, J. B. Hutchison, C. N. Bowman, and K. S. Anseth, "A methacrylated photoiniferter as a chemical basis for microlithography: Micropatterning based on photografting polymerization," *Macromolecules*, 2003.

[22] N. Luo, J. B. Hutchison, K. S. Anseth, and C. N. Bowman, "Surface-initiated photopolymerization of poly(ethylene glycol) methyl ether methacrylate on a diethyldithiocarbamate-mediated polymer substrate," *Macromolecules*, 2002.

[23] H. Ma, R. H. Davis, and C. N. Bowman, "Novel sequential photoinduced living graft polymerization," *Macromolecules*, 2000.

[24] D. Qin, Y. Xia, and G. M. Whitesides, "Soft lithography for micro- and nanoscale patterning," *Nat. Protoc.*, vol. 5, no. 3, pp. 491–502, 2010.

[25] P. Kim, K. W. Kwon, M. C. Park, S. H. Lee, S. M. Kim, and K. Y. Suh, "Soft lithography for microfluidics: A Review," *Biochip Journal*. 2008.

[26] K. Y. Suh, J. Seong, A. Khademhosseini, P. E. Laibinis, and R. Langer, "A simple soft lithographic route to fabrication of poly(ethylene glycol) microstructures for protein and cell patterning," *Biomaterials*, 2004.

[27] W. M. Moreau, *Semiconductor Lithography*. 1988.

[28] P. Rai-Choudhury, *Handbook of Microlithography, Micromachining, and Microfabrication, Volume 2: Micromachining and Microfabrication*. 1997.

[29] D. Qin, Y. Xia, and G. M. Whitesides, "Rapid prototyping of complex structures with feature sizes larger than 20 μm," *Adv. Mater.*, 1996.

[30] Y. Xia *et al.*, "Replica molding using polymeric materials: A practical step toward nanomanufacturing," *Adv. Mater.*, 1997.

[31] C. Eaborn, "Siloxane polymers," *J. Organomet. Chem.*, 1994.

[32] B. D. Gates and G. M. Whitesides, “Replication of Vertical Features Smaller than 2 nm by Soft Lithography,” *J. Am. Chem. Soc.*, 2003.

[33] Y. Xia, E. Kim, X. M. Zhao, J. A. Rogers, M. Prentiss, and G. M. Whitesides, “Complex optical surfaces formed by replica molding against elastomeric masters,” *Science (80-.).*, 1996.

[34] K. Subramani and M. A. Birch, “Micropatterning of Poly (Ethylene Glycol)-Diacrylate (PEG-DA) Hydrogel by Soft-Photolithography for Analysis of Cell-Biomaterial Interactions,” *J. Biomimetics, Biomater. Tissue Eng.*, 2009.

[35] S. Brittain, K. Paul, X. M. Zhao, and G. Whitesides, “Soft lithography and microfabrication,” *Phys. World*, 1998.

[36] Y. Xia and G. M. Whitesides, “Soft lithography,” *Annu. Rev. Mater. Sci.*, vol. 28, no. 1, pp. 153–184, 1998.

[37] G. Oster and N. L. Yang, “Photopolymerization of vinyl monomers,” *Chem. Rev.*, 1968.

[38] O. W. Webster, “Group transfer polymerization: Mechanism and comparison with other methods for controlled polymerization of acrylic monomers,” *Advances in Polymer Science*. 2004.

[39] S. Fiori, A. Mariani, S. Bidali, and G. Malucelli, “Synthesis and characterization of unsaturated polyester resins cured by frontal polymerization,” *E-Polymers*, 2004.

[40] N. V. Gama, A. Ferreira, and A. Barros-Timmons, “Polyurethane foams: Past, present, and future,” *Materials*. 2018.

[41] S. C. Ligon, B. Husár, H. Wutzel, R. Holman, and R. Liska, “Strategies to reduce oxygen inhibition in photoinduced polymerization,” *Chemical Reviews*. 2014.

[42] C. A. Schlecht and J. A. Maurer, “Functionalization of glass substrates: Mechanistic insights into the surface reaction of trialkoxysilanes,” *RSC Adv.*, 2011.

[43] K. Subramani, “Fabrication of hydrogel micropatterns by soft photolithography,” in *Emerging Nanotechnologies for Manufacturing*, 2014.

[44] L. Gao and T. J. McCarthy, “A perfectly hydrophobic surface (θA/θR = 180°/180°),” *J. Am. Chem. Soc.*, 2006.

[45] P. S. Noonan, A. Shavit, B. R. Acharya, and D. K. Schwartz, “Mixed alkylsilane functionalized surfaces for simultaneous wetting and homeotropic anchoring of liquid crystals,” *ACS Appl. Mater. Interfaces*, 2011.

[46] K. Angjelo and S. Elwood, “Piranha Solutions,” *Princeton University*, 2014. .

[47] S. H. Tan, N. T. Nguyen, Y. C. Chua, and T. G. Kang, “Oxygen plasma treatment for reducing hydrophobicity of a sealed polydimethylsiloxane microchannel,” *Biomicrofluidics*, 2010.

[48] B. Arkles, J. R. Steinmetz, J. Zazyczny, and P. Mehta, “Factors contributing to the stability

of alkoxysilanes in aqueous solution," *J. Adhes. Sci. Technol.*, 1992.

[49] S.-C. Jeng and S.-J. Hwang, "Controlling the Alignment of Polyimide for Liquid Crystal Devices," in *High Performance Polymers - Polyimides Based - From Chemistry to Applications*, 2012.

[50] P. Vetter, Y. Ohmura, and T. Uchida, "Study of memory alignment of nematic liquid crystals on polyvinyl alcohol coatings," *Jpn. J. Appl. Phys.*, 1993.

[51] A. Sen, K. A. Kupcho, B. A. Grinwald, H. J. Vantreeck, and B. R. Acharya, "Liquid crystal-based sensors for selective and quantitative detection of nitrogen dioxide," *Sensors Actuators, B Chem.*, 2013.

[52] J.-D. Brassard, D. K. Sarkar, and J. Perron, "Fluorine Based Superhydrophobic Coatings," *Appl. Sci.*, 2012.

[53] M. Li, Q. Dai, W. Huang, and X. Wang, "Pillar versus dimple patterned surfaces for wettability and adhesion with varying scales," *J. R. Soc. Interface*, 2018.

[54] R. Langer and J. P. Vacanti, "- ARTICLES Tissue Engineering," *Science (80-.).*, 1993.

[55] R. Lanza, R. Langer, and J. P. Vacanti, *Principles of Tissue Engineering: Fourth Edition*. 2013.

[56] J. Vacanti, "Tissue engineering and regenerative medicine: from first principles to state of the art," *Journal of Pediatric Surgery*. 2010.

[57] C. Mason and P. Dunnill, "A brief definition of regenerative medicine," *Regenerative Medicine*, 2008.

[58] H. L. Greenwood, H. Thorsteinsdóttir, G. Perry, J. Renihan, P. A. Singer, and A. S. Daar, "Regenerative medicine: New opportunities for developing countries," *Int. J. Biotechnol.*, 2006.

[59] L. G. Griffith and G. Naughton, "Tissue engineering - Current challenges and expanding opportunities," *Science*. 2002.

[60] R. Langer, "Perspectives and challenges in tissue engineering and regenerative medicine," *Advanced Materials*. 2009.

[61] A. Khademhosseini, R. Langer, J. Borenstein, and J. P. Vacanti, "Microscale technologies for tissue engineering and biology," *Proceedings of the National Academy of Sciences of the United States of America*. 2006.

[62] M. McCune, A. Shafiee, G. Forgacs, and I. Kosztin, "Predictive modeling of post bioprinting structure formation," *Soft Matter*, 2014.

[63] C. Norotte, F. S. Marga, L. E. Niklason, and G. Forgacs, "Scaffold-free vascular tissue engineering using bioprinting," *Biomaterials*, 2009.

[64] H. W. Kang, S. J. Lee, I. K. Ko, C. Kengla, J. J. Yoo, and A. Atala, "A 3D bioprinting system to

produce human-scale tissue constructs with structural integrity," *Nat. Biotechnol.*, 2016.

[65] R. Gaebel *et al.*, "Patterning human stem cells and endothelial cells with laser printing for cardiac regeneration," *Biomaterials*, 2011.

[66] E. S. Kim, E. H. Ahn, T. Dvir, and D. H. Kim, "Emerging nanotechnology approaches in tissue engineering and regenerative medicine," *International Journal of Nanomedicine*. 2014.

[67] H. S. Yang *et al.*, "Nanopatterned muscle cell patches for enhanced myogenesis and dystrophin expression in a mouse model of muscular dystrophy," *Biomaterials*, 2014.

[68] B. G. Chung, L. Kang, and A. Khademhosseini, "Micro- and nanoscale technologies for tissue engineering and drug discovery applications," *Expert Opinion on Drug Discovery*. 2007.

[69] D. Carson *et al.*, "Nanotopography-Induced Structural Anisotropy and Sarcomere Development in Human Cardiomyocytes Derived from Induced Pluripotent Stem Cells," *ACS Appl. Mater. Interfaces*, vol. 8, no. 34, pp. 21923–21932, 2016.

[70] D. A. Dunn, A. J. Hodge, and E. A. Lipke, "Biomimetic materials design for cardiac tissue regeneration," *Wiley Interdiscip. Rev. Nanomedicine Nanobiotechnology*, 2014.

[71] D. Zhang, I. Y. Shadrin, J. Lam, H. Q. Xian, H. R. Snodgrass, and N. Bursac, "Tissue-engineered cardiac patch for advanced functional maturation of human ESC-derived cardiomyocytes," *Biomaterials*, 2013.

[72] M. Gherghiceanu *et al.*, "Cardiomyocytes derived from human embryonic and induced pluripotent stem cells: Comparative ultrastructure," *J. Cell. Mol. Med.*, 2011.

[73] S. D. Lundy, W. Z. Zhu, M. Regnier, and M. A. Laflamme, "Structural and functional maturation of cardiomyocytes derived from human pluripotent stem cells," *Stem Cells Dev.*, 2013.

[74] S. D. Bird *et al.*, "The human adult cardiomyocyte phenotype," *Cardiovasc. Res.*, 2003.

[75] S. J. Bryant and K. S. Anseth, "Hydrogel properties influence ECM production by chondrocytes photoencapsulated in poly(ethylene glycol) hydrogels," *J. Biomed. Mater. Res.*, 2002.

[76] L. Smith, S. Cho, and D. E. Discher, "Mechanosensing of matrix by stem cells: From matrix heterogeneity, contractility, and the nucleus in pore-migration to cardiogenesis and muscle stem cells in vivo," *Seminars in Cell and Developmental Biology*. 2017.

[77] O. Wichterle and D. Lím, "Hydrophilic Gels for Biological Use," *Nature*, 1960.

[78] R. M. Nerem and D. Seliktar, "Vascular Tissue Engineering," *Engineering*, vol. 3, pp. 225–243, 2001.

[79] S. Q. Liu, R. Tay, M. Khan, P. L. Rachel Ee, J. L. Hedrick, and Y. Y. Yang, "Synthetic hydrogels for controlled stem cell differentiation," *Soft Matter*. 2009.

[80] J. D. Clapper, J. M. Skeie, R. F. Mullins, and C. A. Guymon, “Development and characterization of photopolymerizable biodegradable materials from PEG-PLA-PEG block macromonomers,” *Polymer (Guildf).*, 2007.

[81] J. Zhu, “Bioactive modification of poly(ethylene glycol) hydrogels for tissue engineering,” *Biomaterials*. 2010.

[82] H. J. Lee, J. S. Lee, T. Chansakul, C. Yu, J. H. Elisseeff, and S. M. Yu, “Collagen mimetic peptide-conjugated photopolymerizable PEG hydrogel,” *Biomaterials*, 2006.

[83] V. A. Liu and S. N. Bhatia, “Three-dimensional photopatterning of hydrogels containing living cells,” *Biomed. Microdevices*, 2002.

[84] M. S. Hahn, L. J. Taite, J. J. Moon, M. C. Rowland, K. A. Ruffino, and J. L. West, “Photolithographic patterning of polyethylene glycol hydrogels,” *Biomaterials*, 2006.

[85] I. Dierking, *Textures of Liquid Crystals*. 2003.

[86] S. Singh, “Phase transitions in liquid crystals,” *Physics Report*. 2000.

[87] C. Ohm, M. Brehmer, and R. Zentel, “Liquid crystalline elastomers as actuators and sensors,” *Advanced Materials*. 2010.

[88] R. Kishi, Y. Suzuki, H. Ichijo, and O. Hirasa, “Electrical deformation of thermotropic liquid-crystalline polymer gels,” *Mol. Cryst. Liq. Cryst. Sci. Technol. Sect. A Mol. Cryst. Liq. Cryst.*, 1997.

[89] H. Finkelmann, W. Gleim, H. J. Kock, and G. Rehage, “Liquid crystalline polymer networks - rubber elastic material with exceptional properties,” *Die Makromol. Chemie*, 1985.

[90] M.-H. Li, P. Keller, B. Li, X. Wang, and M. Brunet, “Light-Driven Side-On Nematic Elastomer Actuators,” *Adv. Mater.*, 2003.

[91] S. Petsch *et al.*, “Smart artificial muscle actuators: Liquid crystal elastomers with integrated temperature feedback,” *Sensors Actuators, A Phys.*, 2015.

[92] R. Zentel, “Liquid Crystalline Elastomers,” *Advanced Materials*. 1989.

[93] P. G. De Gennes, “Possibilites offertes par la reticulation de polymeres en presence d’un cristal liquide,” *Phys. Lett. A*, 1969.

[94] P. G. De Gennes, “No Title,” *Comptes Rendus l’Académie des Sci.*, vol. B, no. 281, p. 101, 1975.

[95] J. Küpfer and H. Finkelmann, “Nematic liquid single crystal elastomers,” *Die Makromol. Chemie, Rapid Commun.*, vol. 12, no. 12, pp. 717–726, 1991.

[96] H. Finkelmann and G. Rehage, “Investigations on liquid crystalline polysiloxanes, 1. Synthesis and characterization of linear polymers,” *Die Makromol. Chemie, Rapid Commun.*, vol. 1, no. 1, pp. 31–34, 1980.

[97] J. Cviklinski, A. R. Tajbakhsh, and E. M. Terentjev, “UV isomerisation in nematic elastomers as a route to photo-mechanical transducer,” *Eur. Phys. J. E*, 2002.

[98] H. Finkelmann, E. Nishikawa, G. G. Pereira, and M. Warner, “A new opto-mechanical effect in solids,” *Phys. Rev. Lett.*, 2001.

[99] B. Donnio, H. Wermter, and H. Finkelmann, “A simple and versatile synthetic route for the preparation of main-chain, liquid-crystalline elastomers,” *Macromolecules*, 2000.

[100] C. E. Carraher Jr., *Seymour/Carraher’s Polymer Chemistry*. 2007.

[101] O. Yaroshchuk and Y. Reznikov, “Photoalignment of liquid crystals: Basics and current trends,” *Journal of Materials Chemistry*. 2012.

[102] H. Zeng, P. Wasylczyk, G. Cerretti, D. Martella, C. Parmeggiani, and D. S. Wiersma, “Alignment engineering in liquid crystalline elastomers: Free-form microstructures with multiple functionalities,” *Appl. Phys. Lett.*, vol. 106, no. 11, 2015.

[103] D. J. Broer, G. P. Crawford, and S. Žumer, *Cross-linked liquid crystalline systems: From rigid polymer networks to elastomers*. 2011.

[104] T. J. White and D. J. Broer, “Programmable and adaptive mechanics with liquid crystal polymer networks and elastomers,” *Nature Materials*. 2015.

[105] A. Buguin, M. H. Li, P. Silberzan, B. Ladoux, and P. Keller, “Micro-actuators: When artificial muscles made of nematic liquid crystal elastomers meet soft lithography,” *J. Am. Chem. Soc.*, vol. 128, no. 4, pp. 1088–1089, 2006.

[106] D. L. Thomsen *et al.*, “Liquid crystal elastomers with mechanical properties of a muscle,” *Macromolecules*, vol. 34, no. 17, pp. 5868–5875, 2001.

[107] T. Ikeda, M. Nakano, Y. Yu, O. Tsutsumi, and A. Kanazawa, “Anisotropic bending and unbending behavior of azobenzene liquid-crystalline gels by light exposure,” *Adv. Mater.*, 2003.

[108] C. L. Van Oosten, C. W. M. Bastiaansen, and D. J. Broer, “Printed artificial cilia from liquid-crystal network actuators modularly driven by light,” *Nat. Mater.*, 2009.

[109] H. Zeng, P. Wasylczyk, C. Parmeggiani, D. Martella, M. Burresi, and D. S. Wiersma, “Light-Fueled Microscopic Walkers,” *Adv. Mater.*, vol. 27, no. 26, pp. 3883–3887, 2015.

[110] D. Martella, S. Nocentini, D. Nuzhdin, C. Parmeggiani, and D. S. Wiersma, “Photonic Microhand with Autonomous Action,” *Adv. Mater.*, vol. 29, no. 42, pp. 1–8, 2017.

[111] S. Nocentini, D. Martella, D. S. Wiersma, and C. Parmeggiani, “Beam steering by liquid crystal elastomer fibres,” *Soft Matter*, vol. 13, no. 45, pp. 8590–8596, 2017.

[112] S. Nocentini, F. Riboli, M. Burresi, D. Martella, C. Parmeggiani, and D. S. Wiersma, “Three-Dimensional Photonic Circuits in Rigid and Soft Polymers Tunable by Light,” *ACS Photonics*,

vol. 5, no. 8, pp. 3222–3230, 2018.

[113] S. Nocentini, D. Martella, C. Parmeggiani, S. Zanotto, and D. S. Wiersma, “Structured Optical Materials Controlled by Light,” *Adv. Opt. Mater.*, vol. 6, no. 15, pp. 1–9, 2018.

[114] C. Ferrantini *et al.*, “Development of Light-Responsive Liquid Crystalline Elastomers to Assist Cardiac Contraction,” *Circ. Res.*, vol. 124, no. 8, pp. e44–e54, 2019.

[115] Y. Hong *et al.*, “Micron-sized main-chain liquid crystalline elastomer actuators with ultralarge amplitude contractions,” *J. Am. Chem. Soc.*, 2009.

[116] H. T. A. Wilderbeek, J. G. P. Goossens, C. W. M. Bastiaansen, and D. J. Broer, “Photoinitiated bulk polymerization of liquid crystalline thiolene monomers,” *Macromolecules*, 2002.

[117] D. Martella, C. Parmeggiani, D. S. Wiersma, M. Piñol, and L. Oriol, “The first thiol-yne click chemistry approach for the preparation of liquid crystalline elastomers,” *J. Mater. Chem. C*, vol. 3, no. 34, pp. 9003–9010, 2015.

[118] B. Reck and H. Ringsdorf, “Combined liquid crystalline polymers: Mesogens in the main chain and as side groups,” *Die Makromol. Chemie, Rapid Commun.*, 1985.

[119] B. Reck and H. Ringsdorf, “Combined liquid-crystalline polymers: Rigid rod and semiflexible main chain polyesters with lateral mesogenic groups,” *Die Makromol. Chemie, Rapid Commun.*, vol. 7, no. 6, pp. 389–396, 1986.

[120] A. Buguin, M. H. Li, P. Silberzan, B. Ladoux, and P. Keller, “Micro-actuators: When artificial muscles made of nematic liquid crystal elastomers meet soft lithography,” *J. Am. Chem. Soc.*, vol. 128, no. 4, pp. 1088–1089, 2006.

[121] H. Zeng *et al.*, “High-resolution 3d direct laser writing for liquid-crystalline elastomer microstructures,” *Adv. Mater.*, vol. 26, no. 15, pp. 2319–2322, 2014.

[122] T. Ikeda, “Photomodulation of liquid crystal orientations for photonic applications,” *Journal of Materials Chemistry*. 2003.

[123] A. Natansohn and P. Rochon, “Photoinduced motions in azo-containing polymers,” *Chem. Rev.*, 2002.

[124] H. Rau, “Azo Compounds,” in *Photochromism: Molecules and Systems*, 2003.

[125] K. Morgenstern, “Isomerization reactions on single adsorbed molecules,” *Accounts of Chemical Research*. 2009.

[126] J. Henzl, M. Mehlhorn, H. Gawronski, K. H. Rieder, and K. Morgenstern, “Reversible cis-trans isomerization of a single azobenzene molecule,” *Angew. Chemie - Int. Ed.*, 2006.

[127] E. Merino and M. Ribagorda, “Control over molecular motion using the cis-trans photoisomerization of the azo group,” *Beilstein Journal of Organic Chemistry*. 2012.

[128] Y. Zhao and T. Ikeda, *Smart Light-Responsive Materials: Azobenzene-Containing Polymers*

and Liquid Crystals. 2008.

[129] P. J. Flory, C. A. J. Hoeve, and A. Ciferri, “Influence of bond angle restrictions on polymer elasticity,” *J. Polym. Sci.*, 1959.

[130] S. Nocentini, D. Martella, C. Parmeggiani, and D. S. Wiersma, “Photoresist design for elastomeric light tunable photonic devices,” *Materials (Basel).*, vol. 9, no. 7, pp. 1–11, 2016.

[131] D. Martella *et al.*, “Light activated non-reciprocal motion in liquid crystalline networks by designed microactuator architecture,” *RSC Adv.*, 2017.

[132] M. G. Debije, “Unravelling the photothermal and photomechanical contributions to actuation of azobenzene-doped liquid crystal polymers in air and water †,” 2019.

[133] D. Martella, S. Nocentini, F. Micheletti, D. S. Wiersma, and C. Parmeggiani, “Polarization-dependent deformation in light responsive polymers doped by dichroic dyes,” *Soft Matter*, 2019.

[134] D. Liu and D. J. Broer, “New insights into photoactivated volume generation boost surface morphing in liquid crystal coatings,” *Nat. Commun.*, vol. 6, pp. 1–7, 2015.

[135] D. G. Legrand and G. L. Gaines, “The molecular weight dependence of polymer surface tension,” *J. Colloid Interface Sci.*, vol. 31, no. 2, pp. 162–167, 1969.

[136] W. R. Ashurst, C. Carraro, and R. Maboudian, “Vapor phase anti-stiction coatings for MEMS,” *IEEE Transactions on Device and Materials Reliability*. 2003.

[137] I. W. Moran, A. L. Briseno, S. Loser, and K. R. Carter, “Device fabrication by easy soft imprint nano-lithography,” *Chem. Mater.*, vol. 20, no. 14, pp. 4595–4601, 2008.

[138] Z. Fan *et al.*, “Three-dimensional nanopillar-array photovoltaics on low-cost and flexible substrates,” *Nat. Mater.*, vol. 8, no. 8, pp. 648–653, 2009.

[139] J. Chen, C. Gu, H. Lin, and S.-C. Chen, “Soft mold-based hot embossing process for precision imprinting of optical components on non-planar surfaces,” *Opt. Express*, vol. 23, no. 16, p. 20977, 2015.

[140] J. Macadangdang *et al.*, “Capillary Force Lithography for Cardiac Tissue Engineering,” no. June, pp. 1–8, 2014.

[141] G. C. Lisensky *et al.*, “Replication and Compression of Surface Structures with Polydimethylsiloxane Elastomer,” *J. Chem. Educ.*, 1999.

[142] H. Yang, G. Ye, X. Wang, and P. Keller, “Micron-sized liquid crystalline elastomer actuators,” *Soft Matter*, 2011.

[143] M. Warner and E. M. Terentjev, *Liquid Crystal Elastomers*. 2003.

[144] P.-G. de Gennes and J. Prost, “The physics of liquid crystals (international series of monographs on physics),” *Oxford Univ. Press. USA*, 1995.

[145] F. Xia and L. Jiang, “Bio-inspired, smart, multiscale interfacial materials,” *Advanced Materials*. 2008.

[146] H. Shahsavan, S. M. Salili, A. Jákli, and B. Zhao, “Smart Muscle-Driven Self-Cleaning of Biomimetic Microstructures from Liquid Crystal Elastomers,” *Adv. Mater.*, vol. 27, no. 43, pp. 6828–6833, 2015.

[147] A. Priimagi *et al.*, “Location of the Azobenzene moieties within the cross-linked liquid-crystalline polymers can dictate the direction of photoinduced bending,” *ACS Macro Lett.*, 2012.

[148] A. Massi and D. Nanni, “Thiol-yne coupling: Revisiting old concepts as a breakthrough for up-to-date applications,” *Organic and Biomolecular Chemistry*. 2012.

[149] L. S. C. Finzi, G. Venturini, “No Title,” *Gazz. Chim. Ital.*, vol. 60, p. 798, 1930.

[150] E. P. Kohler and R. G. Larsen, “The Properties of Unsaturated Sulfur Compounds. III. Alpha Beta Unsaturated Ketosulfones,” *J. Am. Chem. Soc.*, 1936.

[151] B. D. Fairbanks, T. F. Scott, C. J. Kloxin, K. S. Anseth, and C. N. Bowman, “Thiol-yne photopolymerizations: Novel mechanism, kinetics, and step-growth formation of highly cross-linked networks,” *Macromolecules*, 2009.

[152] J. W. Chan, H. Zhou, C. E. Hoyle, and A. B. Lowe, “Photopolymerization of thiol-alkynes: Polysulfide networks,” *Chem. Mater.*, 2009.

[153] J. Escorihuela, A. T. M. Marcelis, and H. Zuilhof, “Metal-Free Click Chemistry Reactions on Surfaces,” *Advanced Materials Interfaces*. 2015.

[154] J. A. Carioscia, H. Lu, J. W. Stanbury, and C. N. Bowman, “Thiol-ene oligomers as dental restorative materials,” *Dent. Mater.*, 2005.

[155] H. Lu, J. A. Carioscia, J. W. Stansbury, and C. N. Bowman, “Investigations of step-growth thiol-ene polymerizations for novel dental restoratives,” *Dent. Mater.*, 2005.

[156] *Radiation Curing in Polymer Science and Technology—Volume II*. 1993.

[157] H. H. Szmant, A. J. Mata, A. J. Namis, and A. M. Panthananickal, “The thiol-olefin co-oxidation (TOCO) Reaction-IV. Temperature effects on product distribution in the toco reaction of indene and aromatic thiols,” *Tetrahedron*, 1976.

[158] G. Odian, *Principles of Polimerization*. 2004.

[159] A. B. Lowe and J. W. Chan, “Thiol-yne Chemistry in Polymer and Materials Science,” in *Functional Polymers by Post-Polymerization Modification: Concepts, Guidelines, and Applications*, 2013.

[160] J. G. Kloosterboer, G. F. C. M. Lijten, and H. M. J. Boots, “Network formation by chain crosslinking photopolymerization and some applications in electronics,” *Makromol.*

Chemie. Macromol. Symp., 1989.

[161] Z. L. Wu *et al.*, "Microstructured nematic liquid crystalline elastomer surfaces with switchable wetting properties," *Adv. Funct. Mater.*, 2013.

[162] M. Lomba *et al.*, "In Situ Photopolymerization of Biomaterials by Thiol-yne Click Chemistry," *Macromol. Biosci.*, 2011.

[163] P. J. Collings and M. Hird, *Introduction to liquid crystals: Chemistry and physics*. 2017.

[164] I. Dierking, "Handbook of liquid crystals," *Liq. Cryst. Today*, 2017.

[165] M. O. Saed, A. H. Torbati, D. P. Nair, and C. M. Yakacki, "Synthesis of programmable main-chain liquid-crystalline elastomers using a two-stage thiol-acrylate reaction," *J. Vis. Exp.*, 2016.

[166] G. R. Mitchell, M. Coulter, F. J. Davis, and W. Guo, "The effect of the spacer length on the nature of coupling in side chain liquid crystals polymers and elastomers," *J. Phys. II*, 1992.

[167] L. T. De Haan, A. P. H. J. Schenning, and D. J. Broer, "Programmed morphing of liquid crystal networks," *Polymer (Guildf).*, 2014.

[168] J. B. Brenneman *et al.*, "Heterocyclic carboxylic acids as activators of soluble guanylate cyclase." pp. 73–76, 2016.

[169] "expt HTag amide formation w HATU (279)__WO2014149164.pdf." .

[170] H. E. Westlake and G. Dougherty, "The Reaction of Benzoyl Chloride with Sodium Thiosulfate," *J. Am. Chem. Soc.*, vol. 67, no. 10, p. 1861, 1945.

[171] V. V. Sureshbabu, T. M. Vishwanatha, and B. Vasantha, "A simple synthesis of N β-Fmoc/Z-amino alkyl thiols and their use in the synthesis of N β-Fmoc/Z-amino alkyl sulfonic acids," *Synlett*, 2010.

[172] J. Hu and M. A. Fox, "A convenient trimethylsilylthioxy-dehalogenation reaction for the preparation of functionalized thiols," *J. Org. Chem.*, 1999.

[173] J. M. MacDougall, X. D. Zhang, W. E. Polgar, T. V. Khroyan, L. Toll, and J. R. Cashman, "Design, chemical synthesis, and biological evaluation of thiosaccharide analogues of morphine- and codeine-6-glucuronide," *J. Med. Chem.*, 2004.

[174] C. C. Han and R. Balakumar, "Mild and efficient methods for the conversion of benzylic bromides to benzylic thiols," *Tetrahedron Lett.*, 2006.

[175] S. K. Pal, V. A. Raghunathan, and S. Kumar, "Phase transitions in novel disulphide-bridged alkoxycyanobiphenyl dimers," *Liq. Cryst.*, 2007.

[176] B. C. Yao, J. Z. Sun, A. J. Qin, and B. Z. Tang, "Thiol-yne click polymerization," *Chinese Science Bulletin*. 2013.

[177] A. Bagheri and J. Jin, "Photopolymerization in 3D Printing," *ACS Appl. Polym. Mater.*, 2019.

[178] M. Kondo, Y. Yu, and T. Ikeda, “How does the initial alignment of mesogens affect the photoinduced bending behavior of liquid-crystalline elastomers?,” *Angew. Chemie - Int. Ed.*, vol. 45, no. 9, pp. 1378–1382, 2006.

[179] A. L. Elias, K. D. Harris, C. W. M. Bastiaansen, D. J. Broer, and M. J. Brett, “Photopatterned liquid crystalline polymers for microactuators,” *J. Mater. Chem.*, 2006.

[180] Y. Jiang, P. Park, S. M. Hong, and K. Ban, “Maturation of cardiomyocytes derived from human pluripotent stem cells: Current strategies and limitations,” *Molecules and Cells*. 2018.

[181] A. Alhadlaq, M. Tang, and J. J. Mao, “Engineered adipose tissue from human mesenchymal stem cells maintains predefined shape and dimension: Implications in soft tissue augmentation and reconstruction,” *Tissue Eng.*, 2005.

[182] M. P. Lutolf and J. A. Hubbell, “Synthetic biomaterials as instructive extracellular microenvironments for morphogenesis in tissue engineering,” *Nature Biotechnology*. 2005.

[183] P. A. Ramires, M. A. Miccoli, E. Panzarini, L. Dini, and C. Protopapa, “In vitro and in vivo biocompatibility evaluation of a polyalkylimide hydrogel for soft tissue augmentation,” *J. Biomed. Mater. Res. - Part B Appl. Biomater.*, 2005.

[184] X. Tong and F. Yang, “Engineering interpenetrating network hydrogels as biomimetic cell niche with independently tunable biochemical and mechanical properties,” *Biomaterials*, 2014.

[185] S. Nemir, H. N. Hayenga, and J. L. West, “PEGDA hydrogels with patterned elasticity: Novel tools for the study of cell response to substrate rigidity,” *Biotechnol. Bioeng.*, 2010.

[186] K. Arcaute, B. Mann, and R. Wicker, “Stereolithography of spatially controlled multi-material bioactive poly(ethylene glycol) scaffolds,” *Acta Biomater.*, 2010.

[187] E. Käpylä, T. Sedlačík, D. B. Aydogan, J. Viitanen, F. Rypáček, and M. Kellomäki, “Direct laser writing of synthetic poly(amino acid) hydrogels and poly(ethylene glycol) diacrylates by two-photon polymerization,” *Mater. Sci. Eng. C*, vol. 43, pp. 280–289, 2014.

[188] J. M. Pioner *et al.*, “Optical Investigation of Action Potential and Calcium Handling Maturation of hiPSC-Cardiomyocytes on Biomimetic Substrates,” *Int. J. Mol. Sci.*, vol. 20, no. 15, p. 3799, 2019.

[189] M. G. Hibberd and B. R. Jewell, “Calcium- and length-dependent force production in rat ventricular muscle,” *J. Physiol.*, 1982.

[190] J. C. Kentish, H. E. D. J. Ter Keurs, L. Ricciardi, J. J. Bucx, and M. I. Noble, “Comparison between the sarcomere length-force relations of intact and skinned trabeculae from rat

right ventricle. Influence of calcium concentrations on these relations," *Circ. Res.*, 1986.

[191] J. P. Konhilas, T. C. Irving, and P. P. De Tombe, "Frank-Starling law of the heart and the cellular mechanisms of length-dependent activation," *Pflugers Archiv European Journal of Physiology*. 2002.

[192] X. Yang, L. Pabon, and C. E. Murry, "Engineering adolescence: Maturation of human pluripotent stem cell-derived cardiomyocytes," *Circulation Research*. 2014.

[193] C. Ferrantini *et al.*, "Late sodium current inhibitors to treat exercise-induced obstruction in hypertrophic cardiomyopathy: an in vitro study in human myocardium," *Br. J. Pharmacol.*, 2018.

[194] R. Coppini *et al.*, "Late sodium current inhibition reverses electromechanical dysfunction in human hypertrophic cardiomyopathy," *Circulation*, 2013.